A Measurement of the c and b Quark Asymmetries in Electron Positron Annihilation

T. J. GREENSHAW

A thesis submitted to the Victoria University of Manchester for the degree of Doctor of Philosophy in the Department of Physics in the Faculty of Science.

October 1985

ABSTRACT

The c and b quark asymmetries were determined from an analysis of electron inclusive multihadronic events recorded with the JADE detector sited on the e^+e^- storage ring PETRA. At a centre of mass energy of $35\,GeV$ the measured values of the asymmetries were $A_c = -0.15 \pm 0.15 \pm 0.03$ and $A_b = -0.24 \pm 0.16 \pm 0.03$ respectively, where the first error is statistical and the second systematic. These results are in good agreement with the Standard Model expectations of $A_c^{\mathrm{SM}} = -0.126$ and $A_b^{\mathrm{SM}} = -0.230$. Combination of the above result for A_b with a previous measurement made by the JADE group enabled a limit to be placed on the $B^0\overline{B^0}$ mixing parameter. At the 90% confidence level, $r < 0.40$.

PREFACE

The author obtained his first degree from Durham University in July 1982 and then transferred to the physics department at the University of Manchester for three years of postgraduate study with the High Energy Physics group. A Diploma for Advanced Studies in Science was awarded in July 1983. This thesis is the result of work carried out since that date at DESY in Hamburg, West Germany.

No portion of the work referred to in this thesis has been submitted in support of an application for another degree or qualification of this or any other institution of learning.

CONTENTS

General Introduction

This thesis describes the measurement of a quantity dependent on the interference effects which occur between the neutral carrier of the weak force and its electromagnetic counterpart, the photon. This quantity, measured for both c and b flavours, is the asymmetry in the production direction of the quarks with respect to the electron direction in electron positron annihilation. Hence the axial coupling of these quarks to the weak neutral force was measured, testing a sector of the Standard Model of elementary particle interactions. Furthermore it is shown that the measurement of the b asymmetry provides a means of studying mixing in the $B^0\overline{B^0}$ system.

The following is divided into two parts. In the first part the Standard Model is introduced. Its predictions concerning the quark production asymmetries and some other results of interest in the context of the measurement made are also given. The construction and operation of the JADE experiment and the standard analysis techniques used are then described. The description of the Standard Model does not follow the historical course of events, but is designed to emphasize the role of the principle of local gauge invariance in the development of the theories involved, this principle being responsible for the Standard Model coupling constant assignments which are measured.

In the second part the problems encountered in measuring the b and c asymmetries and how they were solved are described. The results of the analysis are then presented and discussed.

Part I

THE STANDARD MODEL, QUARK PRODUCTION IN e^+e^- ANNIHILATION AND THE JADE EXPERIMENT

Introduction.

Of the particles seen in physics experiments (Particle Data Group, 1984) only the five leptons, the photon γ and the weak bosons, the W^+, the W^- and the Z^0 are considered to be fundamental. The leptons are the electron e and its neutrino ν_e, the muon μ and its neutrino ν_μ and the tauon τ. The τ is assumed to be accompanied by another neutrino, the ν_τ. The first of each pair has charge -1 in units of the proton charge and the second is neutral. All other particles, collectively called hadrons, are thought to be bound states of another set of fundamental particles which cannot escape outside hadrons, the quarks.[1] The hadrons may be split into two classes, mesons and baryons. Mesons are bound states of a quark and an anti-quark, while baryons are composed of three quarks. There is good experimental evidence for the existence of five types of quarks (Perkins, Close). These are distinguished by the flavours down d, up u, strangeness s, charm c and beauty or bottom b. There is strong indirect evidence for the existence of a sixth quark flavour, top t (Bartel, 1983a) and some indication that it has been produced at the CERN proton anti-proton collider (UA1, 1985). The first, third and fifth of these particles have charge $-1/3$, the second, fourth and sixth charge $+2/3$. The leptons and quarks are all pointlike and have spin $1/2$ in units of $\hbar$. The photon and the weak bosons have spin 1.

The interaction binding the quarks together to form the particles seen in physics experiments, the hadrons, is termed the strong interaction. It is thought to be carried by another type of boson, the gluon. This interaction has the peculiarity that as the interquark separation increases it gets stronger, explaining

[1] It is also possible that bound states of gluons, or a mixture of such bound states with quark bound states, exist as physical particles. The ι may be such a particle (Edwards, 1982).

why the quarks and gluons never exist as free particles.[1] All fundamental particles undergo gravitational interactions, all those that are electrically charged undergo electromagnetic interactions, and all the fundamental fermions undergo weak interactions. The gravitational interaction is negligible at the energies at which particle physics experiments are done and will thus not be further considered. The electromagnetic interaction, coupling to particles through their electric charge, is familiar in its classical manifestation from everyday life. It has infinite range. The weak interaction, responsible for the beta decay of the neutron, is not intrinsically weak but has only very short range.

An essential feature of the currently favoured theories of fundamental particle physics is the idea that the forms of these interactions are dictated by a symmetry principle; local gauge, or phase, invariance. This principle, together with experimental evidence as to the symmetry groups involved, has led to the development of a theory of the strong interactions; Quantum Chromodynamics. The addition of the Higgs mechanism, enabling the introduction of forces whose range is limited by the mass of the particles which transmit them, made possible the development of a theory which simultaneously describes electromagnetic and weak interactions, the Glashow-Salam-Weinberg model. The Higgs mechanism spontaneously breaks, or better hides, the fundamental symmetry of the interactions in this model. Clues to the symmetry remain however, specifically in the relative strengths with which the interactions affect the different particles in the theory and in the existence of a neutral carrier of the weak force. Together Quantum Chromodynamics and the Glashow-Salam-Weinberg model form the Standard Model of fundamental particle interactions.

The notation in the following sections is that which is used in texts such as Aitchison (1982), Aitchison and Hey (1982) and Bjorken and Drell (1964, 1965).

[1] There is one piece of experimental evidence which seems to contradict this (Fairbank, 1981).

Chapter 1

THE STANDARD MODEL

Quantum Field Theory and the Feynman Rules.

The framework within which current theories of the fundamental interactions are described is that of the Lagrangian formulation of relativistic quantum field theory. Systems are described by a Lagrangian L, or it's density L, which depends on the fields of the theory and their gradients. The fields are a means of representing multiple particle states. The equations of motion of the system are obtained from the action principle, namely that $I = \int d^4x\, L$ be stationary under variation of the fields. Correct special relativistic behaviour is ensured if L is a Lorentz invariant function.

Consider the case of a scalar field $\phi(x)$ and let L have the form

$$L = \frac{1}{2}\Big(\partial_\mu\phi(x)\partial^\mu\phi(x) - m^2\phi^2(x)\Big).$$

Applying the action principle gives the Euler-Lagrange equations (Goldstein, p36)

$$\partial_\mu\left(\frac{\partial L}{\partial(\partial_\mu\phi)}\right) - \frac{\partial L}{\partial\phi} = 0$$

which in this case reduce to

$$(\partial_\mu\partial^\mu + m^2)\phi = 0$$

the Klein-Gordon equation , describing the motion of a free scalar field of mass m.

So far the discussion has been classical. Quantization of the system may be performed using the canonical procedure. A momentum π conjugate to the field ϕ is defined by

$$\pi(x) = \frac{\partial L}{\partial(\partial_0\phi(x))}.$$

The fields are then replaced by field operators satisfying the commutation relations

$$[\phi(x), \pi(x')] = i\delta^3(\mathbf{x} - \mathbf{x}')$$

$$[\pi(x), \pi(x')] = 0$$

$$[\phi(x), \phi(x')] = 0.$$

(If the fields in question are fermionic then the commutators in the above expressions must be replaced by anti-commutators.) The Hamiltonian density is defined by

$$H(x) = \pi(x)\partial_0\phi(x) - L(x).$$

That the field operators may be used to represent many particle states may be demonstrated using the following argument. Fourier expanding the field and momentum operators in terms of free particle wave functions gives

$$\phi(x) = \frac{1}{(2\pi)^3}\int \frac{d^3k}{2k_0}\left(a(\mathbf{k})e^{-ik\cdot x} + a^\dagger(\mathbf{k})e^{+ik\cdot x}\right)$$

and

$$\pi(x) = \frac{1}{(2\pi)^3}\int \frac{d^3k}{2k_0}\frac{1}{-ik_0}\left(a(\mathbf{k})e^{-ik\cdot x} - a^\dagger(\mathbf{k})e^{+ik\cdot x}\right)$$

where $k_0 = \sqrt{\mathbf{k}^2 + m^2}$. The operators a and $a^\dagger$, as a result of the commutation relations above, obey

$$[a(\mathbf{k}), a^\dagger(\mathbf{k}')] = 2k_0\delta^3(\mathbf{k} - \mathbf{k}')$$

$$[a(\mathbf{k}), a(\mathbf{k}')] = 0$$

$$[a^\dagger(\mathbf{k}), a^\dagger(\mathbf{k}')] = 0.$$

These are very similar to the commutation relations familiar from the case of the simple harmonic oscillator (Merzbacher, p 356).

$$[a(x), a^\dagger(x')] = \delta(x - x')$$

$$[a(x), a(x')] = 0$$

$$[a^\dagger(x), a^\dagger(x')] = 0$$

The fields are then replaced by field operators satisfying the commutation relations

$$[\phi(x), \pi(x')] = i\delta^3(\mathbf{x} - \mathbf{x}')$$

$$[\pi(x), \pi(x')] = 0$$

$$[\phi(x), \phi(x')] = 0.$$

(If the fields in question are fermionic then the commutators in the above expressions must be replaced by anti-commutators.) The Hamiltonian density is defined by

$$H(x) = \pi(x)\partial_0\phi(x) - L(x).$$

That the field operators may be used to represent many particle states may be demonstrated using the following argument. Fourier expanding the field and momentum operators in terms of free particle wave functions gives

$$\phi(x) = \frac{1}{(2\pi)^3}\int \frac{d^3k}{2k_0}\left(a(\mathbf{k})e^{-ik\cdot x} + a^\dagger(\mathbf{k})e^{+ik\cdot x}\right)$$

and

$$\pi(x) = \frac{1}{(2\pi)^3}\int \frac{d^3k}{2k_0}\,\frac{1}{-ik_0}\left(a(\mathbf{k})e^{-ik\cdot x} - a^\dagger(\mathbf{k})e^{+ik\cdot x}\right)$$

where $k_0 = \sqrt{\mathbf{k}^2 + m^2}$. The operators a and $a^\dagger$, as a result of the commutation relations above, obey

$$[a(\mathbf{k}), a^\dagger(\mathbf{k}')] = 2k_0\delta^3(\mathbf{k} - \mathbf{k}')$$

$$[a(\mathbf{k}), a(\mathbf{k}')] = 0$$

$$[a^\dagger(\mathbf{k}), a^\dagger(\mathbf{k}')] = 0.$$

These are very similar to the commutation relations familiar from the case of the simple harmonic oscillator (Merzbacher, p 356).

$$[a(x), a^\dagger(x')] = \delta(x - x')$$

$$[a(x), a(x')] = 0$$

$$[a^\dagger(x), a^\dagger(x')] = 0$$

in which case, the following relationships between the Hamiltonian H and the annihilation and creation operators a and $a^\dagger$ hold

$$[\mathrm{H}, a] = -\omega a$$

and

$$[\mathrm{H}, a^\dagger] = +\omega a^\dagger.$$

The resulting spectrum is a ladder of states, separated by energy ω. Operating with $a^\dagger$ causes a move one step up the ladder and with a one step down. The ground state is specified by the condition

$$a|0\rangle = 0$$

and has zero point energy $\omega/2$.

Returning to the field theory case, in which

$$\mathrm{H} = \int d^3x\, H$$

the commutation relations analogous to those above are

$$[\mathrm{H}, a(\mathbf{k})] = -k_0 a(\mathbf{k})$$

and

$$[\mathrm{H}, a^\dagger(\mathbf{k})] = +k_0 a^\dagger(\mathbf{k}),$$

there is a ladder of states for each $\mathbf{k}$. The states are separated by an energy of k_0. Thus operating with $a^\dagger$ increases the field energy by k_0 consistent with adding a particle of mass m and momentum $\mathbf{k}$ to it and vice versa for operations with a. This makes the statement that fields may be used to represent many particle states plausible. A more thorough approach shows that the field operator can actually be written in terms of a symmetric (for bosons) or anti-symmetric (for fermions) combination of individual particle wave functions (see, for example, Ziman).

The first of the infinities typical of quantum field theories is encountered here. The ground state of the ϕ field has infinite energy as it is an integral over a contribution of $k_0/2$ for all $\mathbf{k}$. This divergence is easily coped with as only energy differences are measurable and the infinite ground state contribution always subtracts out.

So far the theory that has been considered has been that appropriate to free particles. An interaction term H'_S may be introduced so that $\mathrm{H} = \mathrm{H}_0 + \mathrm{H}'_S$. The time development of the free system, given by the equation of motion

$$\frac{\partial}{\partial t}|\phi(t)\rangle_S = -i\mathrm{H}_0|\phi(t)\rangle_S$$

is

$$|\phi(t)\rangle_S = \sum_n c_n \exp(-iE_n t)|n\rangle$$

where the state has been represented as a sum of the eigenstates $|n\rangle$ satisfying

$$\mathrm{H}_0|n\rangle = E_n|n\rangle.$$

The subscript S denotes that the description is in the Schroedinger picture. The time development of the interacting system is

$$|\phi(t)\rangle_S = \sum_n a_n(t) \exp(-iE_n t)|n\rangle$$

where the effects of the interaction are contained in the time dependent coefficients $a_n(t)$. The phase factors, which are not of interest in describing the interaction, may be removed by using the interaction picture. The state vector in this picture is defined by

$$|\phi(t)\rangle_I = \exp(i\mathrm{H}_0)|\phi(t)\rangle_S$$

and the interaction term in the Hamiltonian becomes

$$\mathrm{H}'_I = \exp(i\mathrm{H}_0)\mathrm{H}'_S \exp(-i\mathrm{H}_0).$$

As may be checked by substitution, the equation of motion is

$$\frac{\partial}{\partial t}|\phi(t)\rangle_I = -i\mathrm{H}'_I|\phi(t)\rangle_I$$

and the remaining time evolution of the state is due only to the interaction. In terms of the eigenstates of the free system

$$|\phi(t)\rangle_I = \sum_n a_n(t)|n\rangle.$$

The interaction picture will be used from now on.

Physics experiments study the transition from a non-interacting particle state at time t_1, long before the interaction of interest takes place, to a non-interacting state long after the interaction has taken place, at time t_2. Define an operator U, which performs this transition, so that

$$|\phi(t)\rangle = U(t,t_1)|\phi(t_1)\rangle.$$

Comparison of this with the equation of motion gives the evolution equation of this operator

$$\frac{\partial}{\partial t}U(t,t_1) = -i\mathrm{H}'U(t,t_1).$$

Integrating this and noting that $U(t_1,t_1) = 1$ (Bjorken and Drell, 1965 p 177) gives

$$U(t_2,t_1) = 1 - i\int_{t_1}^{t_2} \mathrm{H}'U(t,t_1)\,dt.$$

Replacing the U operator under the integral with the expression on the right hand side, and iterating gives an infinite series solution for U

$$U(t_2,t_1) = 1 + (-i)\int_{t_1}^{t_2} dt\,\mathrm{H}'(t) + (-i)^2\int_{t_1}^{t_2} dt\int_{t_1}^{t} dt'\,\mathrm{H}'(t)\mathrm{H}'(t') + \ldots.$$

The n^{th} term in this series is

$$U^{(n)}(t_2,t_1) = (-i)^n\int_{t_1}^{t_2} dt\int_{t_1}^{t} dt'\cdots\int_{t_1}^{t^{(n-2)}} dt^{(n-1)}\,\mathrm{H}'(t)Ha_I(t')\ldots\mathrm{H}'(t^{(n-1)}).$$

Define the scattering operator $S = U(-\infty, +\infty)$, then the n^{th} term in the expansion of S is

$$S^{(n)} = (-i)^n \int_{-\infty}^{\infty} dt_1 \int_{-\infty}^{t_1} dt_2 \cdots \int_{-\infty}^{t_{n-1}} dt_n \, \mathrm{H}'(t_1)\mathrm{H}'(t_2)\ldots\mathrm{H}'(t_n).$$

Demanding that the integrands be time ordered, that is if

$$-\infty < t_1 < t_2 < \cdots < t_n < \infty$$

then the integrand of the n^{th} term is

$$\mathrm{H}'(t_n)\ldots\mathrm{H}'(t_2)\mathrm{H}'(t_1)$$

this becomes (Ziman, p 68)

$$S^{(n)} = \frac{(-i)^n}{n!} \int_{-\infty}^{\infty} dt_1 \int_{-\infty}^{\infty} dt_2 \cdots \int_{-\infty}^{\infty} dt_n \, P\left[\mathrm{H}'(t_1)\mathrm{H}'(t_2)\ldots\mathrm{H}'(t_n)\right]$$

where the P denotes the time ordering process. This may also be written in terms of the interaction Hamiltonian density H'

$$S^{(n)} = \frac{(-i)^n}{n!} \int d^4x_1 \int d^4x_2 \cdots \int d^4x_n \, P\left[H'(x_1)H'(x_2)\ldots H'(x_n)\right].$$

The problem then is to evaluate matrix elements of the form

$$\langle \phi_f | S | \phi_i \rangle$$

where $|\phi_i\rangle$ and $|\phi_f\rangle$ represent the initial and final states respectively.

Consider the previously discussed Lagrangian density, but with an interaction term added, namely

$$L = \frac{1}{2}\partial_\mu\phi\partial^\mu\phi - \frac{1}{2}m^2\phi^2 - \frac{g}{4!}\phi^4.$$

The interaction Hamiltonian is then

$$\begin{aligned} \mathrm{H}' &= \int d^3x H' \\ &= \int d^3x \frac{g}{4!}\phi^4. \end{aligned}$$

The amplitude for scattering from a state $|k_1, k_2\rangle$ into $|k_3, k_4\rangle$ is

$$\langle k_3, k_4|S|k_1, k_2\rangle = \langle 0|a(\mathbf{k}_3)a(\mathbf{k}_4)Sa^\dagger(\mathbf{k}_1)a^\dagger(\mathbf{k}_2)|0\rangle.$$

Considering the case in which $\mathbf{k}_1 \neq \mathbf{k}_3$ and $\mathbf{k}_2 \neq \mathbf{k}_4$ the lowest order term is

$$S_{fi}^{(1)} = \frac{-ig}{4!}\int d^4x \langle 0|a(\mathbf{k}_3)a(\mathbf{k}_4)\phi^4 a^\dagger(\mathbf{k}_1)a^\dagger(\mathbf{k}_2)|0\rangle.$$

Remembering that ϕ may be expanded in terms of the momentum eigenstates and using Wick's theorem (Wick, 1950) enables calculation of this quantity. The only non-zero contributions are of the form

$$\langle 0|\phi(x)a^\dagger(\mathbf{k})|0\rangle = e^{-ik\cdot x}$$

and

$$\langle 0|a(\mathbf{k})\phi(x)|0\rangle = e^{+ik\cdot x}.$$

There are 4! such contributions and together they give

$$\begin{aligned} S_{fi}^{(1)} &= -ig\int d^4x \exp\left[-i(k_1 + k_2 - k_3 - k_4)\cdot x\right] \\ &= -ig(2\pi)^4\delta^4(k_1 + k_2 - k_3 - k_4), \end{aligned}$$

the interaction strength multiplied by a delta function ensuring that energy and momentum are conserved.

This, and indeed all, the terms in the perturbation expansion of the S matrix may be represented using Feynman diagrams. The example above is drawn in figure 1.1. Algebraic factors are associated with elements of these diagrams and, as was first realised by Feynman, these algebraic factors are the same regardless of the context within which the diagram elements occur. For example the vertices in the ϕ^4 theory which has been discussed here always have the factor $-ig$ associated with them. The Feynman diagrams may thus be used to calculate transition amplitudes, without going through the full field theoretic arguments for each different case.

The amplitude for scattering from a state $|k_1, k_2\rangle$ into $|k_3, k_4\rangle$ is

$$\langle k_3, k_4|S|k_1, k_2\rangle = \langle 0|a(\mathbf{k}_3)a(\mathbf{k}_4)Sa^\dagger(\mathbf{k}_1)a^\dagger(\mathbf{k}_2)|0\rangle.$$

Considering the case in which $\mathbf{k}_1 \neq \mathbf{k}_3$ and $\mathbf{k}_2 \neq \mathbf{k}_4$ the lowest order term is

$$S_{fi}^{(1)} = \frac{-ig}{4!}\int d^4x \langle 0|a(\mathbf{k}_3)a(\mathbf{k}_4)\phi^4 a^\dagger(\mathbf{k}_1)a^\dagger(\mathbf{k}_2)|0\rangle.$$

Remembering that ϕ may be expanded in terms of the momentum eigenstates and using Wick's theorem (Wick, 1950) enables calculation of this quantity. The only non-zero contributions are of the form

$$\langle 0|\phi(x)a^\dagger(\mathbf{k})|0\rangle = e^{-ik\cdot x}$$

and

$$\langle 0|a(\mathbf{k})\phi(x)|0\rangle = e^{+ik\cdot x}.$$

There are 4! such contributions and together they give

$$\begin{aligned} S_{fi}^{(1)} &= -ig\int d^4x \exp\left[-i(k_1 + k_2 - k_3 - k_4)\cdot x\right] \\ &= -ig(2\pi)^4\delta^4(k_1 + k_2 - k_3 - k_4), \end{aligned}$$

the interaction strength multiplied by a delta function ensuring that energy and momentum are conserved.

This, and indeed all, the terms in the perturbation expansion of the S matrix may be represented using Feynman diagrams. The example above is drawn in figure 1.1. Algebraic factors are associated with elements of these diagrams and, as was first realised by Feynman, these algebraic factors are the same regardless of the context within which the diagram elements occur. For example the vertices in the ϕ^4 theory which has been discussed here always have the factor $-ig$ associated with them. The Feynman diagrams may thus be used to calculate transition amplitudes, without going through the full field theoretic arguments for each different case.

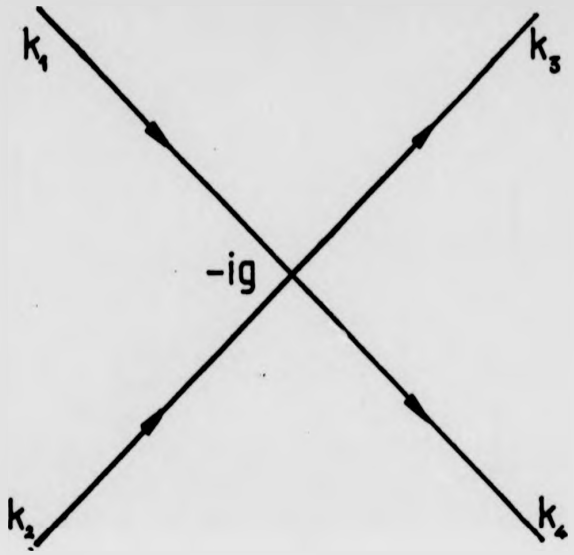

Figure 1.1. Lowest order ϕ^4 field theory scattering diagram.

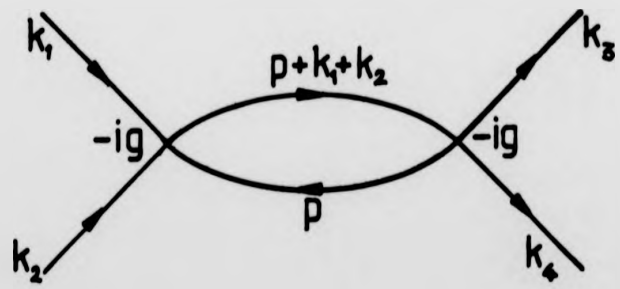

Figure 1.2. Next to lowest order ϕ^4 field theory scattering diagram.

Consider now the next term in the scattering process under study

$$S_{fi}^{(2)} = \frac{1}{2}\left(\frac{-ig}{4!}\right)^2 \iint d^4x d^4y \, \langle 0|a(\mathbf{k}_3)a(\mathbf{k}_4)P|\phi^4(x)\phi^4(y)]a^\dagger(\mathbf{k}_1)a^\dagger(\mathbf{k}_2)|0\rangle.$$

In addition to terms of the type previously discussed this contains a term of the form

$$\langle 0|P|\phi(x)\phi(y)]|0\rangle.$$

Now

$$\langle 0|\phi(x)\phi(y)|0\rangle = \int \frac{d^3k}{(2\pi^3)} \frac{1}{2k_0} \exp\left[-ik\cdot(x-y)\right].$$

The quantity required is similar to the above, but for the time ordering of the product. This may be written

$$P\left[\phi(x)\phi(y)\right] = \theta(x_0 - y_0)\phi(x)\phi(y) + \theta(y_0 - x_0)\phi(y)\phi(x)$$

where the θ function

$$\theta(t) = 1 \text{ for } t > 0$$

$$= 0 \text{ for } t < 0$$

ensures that only the correctly time ordered products are non-zero. This function may be represented by

$$\theta(t) = \frac{i}{2\pi}\int_{-\infty}^{\infty} \frac{d\omega}{\omega + i\epsilon} e^{-i\omega t}$$

which must be evaluated in the complex plane using the residue theorem (see, for example, Kreyzsig). Combining these results

$$\langle 0|P\left[\phi(x)\phi(y)\right]|0\rangle = \int \frac{d^4k}{(2\pi)^4} \frac{\exp\left[-ik\cdot(x-y)\right]}{(k^2 - m^2) + i\epsilon}$$

which may be recognised as the formula for a Feynman propagator. The Feynman diagram for this process is shown in figure 1.2. The amplitude is

$$S_{fi}^{(2)} = \frac{1}{2}(-ig)^2\delta^4(k_1 + k_2 - k_3 - k_4)\int \frac{d^4p}{(2\pi)^4} \frac{i}{p^2 - m^2} \frac{i}{(p + k_1 + k_2)^2 - m^2}$$

where p is the momentum running round the loop in the diagram. Again overall energy-momentum conservation is ensured by the delta function and a factor $-ig$

appears for each vertex. The new feature here is the integral over the loop momentum p. This integral is divergent and represents the second and more serious type of infinity encountered in field theories, not being simply additive as the previous example was. Moreover it is clear that in this theory the problem is worse for higher order terms in the perturbative expansion of the S matrix, as more and more loops appear.

The general treatment of such infinities is a complex subject and will not be tackled here. Suffice it to say that for a certain class of theories, which are known as renormalizable theories, all infinities can be absorbed in a finite number of redefinitions of some of the parameters of the theory, such as masses and charges or coupling constants. Physically this is justifiable, as the so-called 'bare' masses and charges which appear in the Lagrangian are never observable, always being subject to (infinite) corrections due to vacuum polarization effects. Renormalizable theories may be written in terms of the experimentally measured masses and charges. That this may be consistently done to all orders in the perturbative expansion may be proved diagrammatically, a demonstration of the power of the Feynman graphical approach (Ziman, p 186). Until non-perturbative solutions to quantum field theories are found only renormalizable theories are of interest in physics (Weinberg, 1980). An illustration of how renormalization may be carried out is given in the section on Quantum Electrodynamics.

A first indication of the importance of the gauge principle, which is discussed in what follows, is that the property of gauge invariance seems to be crucial in proving that a theory is renormalizable. Conversely, if a theory is constructed with the specific aim of making it renormalizable, it turns out to be a gauge theory (Llewellyn-Smith, 1974). Perhaps an even more important feature of the gauge principle is its power to determine the dynamics of a theory, once the symmetries involved are specified.

The Gauge Principle and Quantum Electrodynamics.

Consider the Lagrangian describing the motion of a free Dirac field ψ of mass m,

$$L_0 = \bar{\psi}(i\gamma^\mu \partial_\mu - m)\psi$$

where the γ^μ are the Dirac matrices, described in Aitchison and Hey. This is invariant under the global phase, or gauge, transformation

$$\psi(x) \rightarrow \psi'(x) = \exp\left[-i\theta\right]\psi(x).$$

The gauge transformation is termed global as the phase change introduced is independent of the space-time coordinates. Such an invariance implies the existence of a conserved current (Noether's theorem) which in this case is

$$j^\mu = \bar{\psi}\gamma^\mu\psi.$$

Writing $\theta = q\chi$ this is seen to be the electromagnetic current for a fermion of charge q

$$j^\mu = q\bar{\psi}\gamma^\mu\psi.$$

Consider, following the suggestion of Yang and Mills (1954), demanding that the Lagrangian be invariant under the local form of the above transformation. That is, let χ be a function of the space-time coordinates x. The local gauge transformation is then

$$\psi(x) \rightarrow \psi'(x) = \exp\left[-iq\chi(x)\right]\psi(x).$$

Some full Lagrangian L_1 must be found so that the variation under the above local transformation δL_1 is zero. Now

$$\begin{aligned}\delta L_0 &= \bar{\psi}'(i\gamma^\mu\partial_\mu - m)\psi' - \bar{\psi}(i\gamma^\mu\partial_\mu - m)\psi \\ &= q\bar{\psi}\gamma^\mu\psi\partial_\mu\chi(x)\end{aligned}$$

so L_1 must contain a term whose change under the local transformation exactly cancels that above. Such a term is $-q\bar{\psi}\gamma^\mu\psi A_\mu$ provided that, as the ψ field undergoes the transformation above, A_μ undergoes the transformation

$$A_\mu(x) \rightarrow A'_\mu(x) = A_\mu(x) + \partial_\mu\chi(x).$$

The Lagrangian then becomes

$$L_1 = \bar{\psi}(i\gamma^\mu\partial_\mu - m)\psi - q\bar{\psi}\gamma^\mu\psi A_\mu.$$

Imposing invariance under the local gauge transformation has forced the introduction of a new vector field A_μ which undergoes interactions with the matter field ψ. The Lagrangian above is exactly that obtained when the 'minimum prescription' for introduction of electromagnetic interactions is used (see, for example, Aitchison and Hey). Thus application of the local gauge principle has generated a theory of electromagnetically interacting Dirac particles from the free theory.

The Lagrangian above is not yet the complete Lagrangian of Quantum Electrodynamics, or QED, as the term describing the behaviour of the A_μ fields is missing, the Yang-Mills term. This is the term which gives rise to the Maxwell equations and it may be introduced in a locally gauge invariant manner using the tensor

$$F^{\mu\nu} = \partial^\mu A^\nu - \partial^\nu A^\mu$$

as under the transformation for the A^μ fields

$$\begin{aligned}\delta F^{\mu\nu} &= \left\{\partial^\mu\left(A^\nu + \partial^\nu\chi(x)\right) - \partial^\nu\left(A^\mu + \partial^\mu\chi(x)\right)\right\} - \left\{\partial^\mu A^\nu - \partial^\nu A^\mu\right\} \\ &= 0.\end{aligned}$$

The addition of a term

$$L_{EM} = -\frac{1}{4}F_{\mu\nu}F^{\mu\nu}$$

so that the full Lagrangian becomes

$$L = \bar{\psi}(i\gamma^\mu\partial_\mu - m)\psi - q\bar{\psi}\gamma^\mu\psi A_\mu - \frac{1}{4}F_{\mu\nu}F^{\mu\nu}$$

ensures that, if the Euler-Lagrange equations are applied to the full Lagrangian, the result

$$\partial_\nu \partial^\nu A^\mu - \partial^\mu (\partial_\nu A_\nu) = j^\mu$$

has the correct Maxwell form. The Maxwell equations in terms of the electric and magnetic fields may be obtained from the above as is shown in, for example, Weinberg (1972).

The crucial stage above, demanding invariance of the Lagrangian under local gauge transformations, is equivalent in this and all cases to replacing the derivatives ∂^μ in the free Lagrangian by their covariant counterparts, D^μ (Aitchison, p36). In the above example

$$D^\mu = \partial^\mu + iqA^\mu.$$

The symmetry to which this simple one-dimensional phase invariance is related is that of the Abelian group U(1).

The QED tree level diagrams, that is those not containing loops, and the algebraic factors with which they are associated are given in Aitchison and Hey.

Renormalization and the Running Coupling Constant.

Consider the process $e^-\mu^- \rightarrow e^-\mu^-$, the lowest order Feynman diagram and a vacuum polarization correction for which are illustrated in figures 1.3 and 1.4 respectively. The amplitudes for these two graphs are the same, but for a modification to the propagator in the second due to an integral over the loop momentum. This tends logarithmically to infinity as the upper limit of the integral goes to infinity (cf. the ϕ^4 theory considered in the first section of this chapter). As the divergence is associated with high energy behaviour it is termed an ultraviolet divergence. Some way of removing this infinity must be found before the theory can be of any use. If an upper bound to the integral, Λ, is introduced then it can

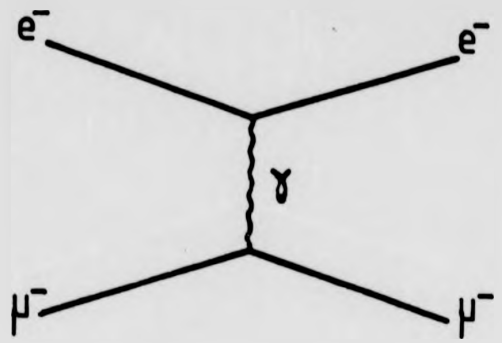

Figure 1.3. Lowest order electron muon scattering diagram.

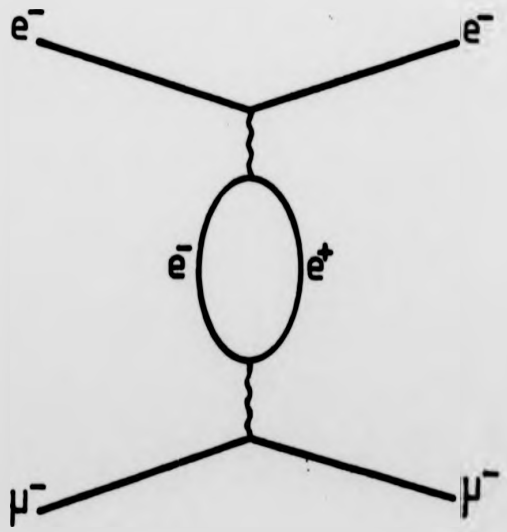

Figure 1.4. Vacuum polarization correction to electron muon scattering.

be shown (Bjorken and Drell, 1964) that the amplitude resulting from the sum of the two graphs in terms of $\alpha B^{(1)}$, the amplitude due to the first graph alone, is

$$\alpha B^{(2)} = \alpha\left[1 - \frac{\alpha}{3\pi}\ln\left(\frac{\Lambda^2}{m^2}\right) - \frac{\alpha}{15\pi}\frac{q^2}{m^2} + O(\alpha^2)\right]B^{(1)}$$

where $\alpha = e^2/(4\pi)$ is the electromagnetic coupling constant, m the mass of the electron and q the momentum transfer. The effect of the vacuum polarization diagram may thus be considered to be, in part, an infinite modification to the coupling constant. Ignoring terms of order α^2 and higher

$$\alpha \to \alpha' = \alpha\left[1 - \frac{\alpha}{3\pi}\ln\left(\frac{\Lambda^2}{m^2}\right)\right].$$

To get sensible predictions out of this theory the relationship between the α which appears in the Lagrangian, and in the formula for the amplitude above, and the measured coupling constant α_m must be found. A measurement of the coupling constant determines

$$\alpha_m = \alpha\left[1 + \sum_{n=1}^{\infty}\alpha^n C_n(\Lambda^2)\right]$$

where C_n is the correction at order α^n of the above form. The bare α may be obtained by inverting this formula. For the example above, working to order $n = 1$, this gives

$$\alpha = \alpha_m\left[1 + \frac{\alpha_m}{3\pi}\ln\left(\frac{\Lambda^2}{m^2}\right)\right].$$

Writing the amplitude in terms of α_m the finite result

$$A = \alpha_m\left[1 + \frac{\alpha_m}{15\pi}\frac{q^2}{m^2} + O(\alpha_m^2)\right]B^{(1)}$$

is obtained. As the expression for α contains an infinite term, the attempt to find the value of the bare α must be abandoned, alternatively stated, the theory cannot predict the value of α_m. At least however, by inserting the measured value of the coupling constant, calculations which give finite results may be performed. Agreement between theory and experiment is in fact extraordinarily good for processes which may be considered purely electrodynamically, see Van Dyck (1976 and 1977).

The above is an example of the process known as renormalization and can in QED be performed systematically order by order to remove all the infinities which occur (Schwinger, 1958).

In addition to the above some q^2 dependence may be included in the definition of the coupling constant. As the amplitudes for the diagrams in figures 1.3 and 1.4 are the same but for the modification to the propagator, using a running coupling constant

$$\alpha'_R(q^2) = \alpha_m(\mu^2)\left[1 - \frac{\alpha_m(\mu^2)}{15\pi}\frac{q^2}{m^2} + O(\alpha_m^2(\mu^2))\right]$$

where μ is some reference momentum transfer, would include the effects of the vacuum polarization graph in the lowest order calculation. For $q^2 >> m^2$ this becomes approximately (Bjorken and Drell, 1964)

$$\alpha''_R(Q^2) = \alpha\left[1 + \frac{\alpha}{3\pi}\ln\left(\frac{Q^2}{m^2}\right)\right]$$

where the subscript m has been dropped, the use of the renormalized coupling constant being implicit, and the positive quantity $Q^2 = -q^2$ is introduced for convenience. Similar expressions may be calculated for higher orders and the most significant parts, the leading log terms, combined to give

$$\alpha_R(Q^2) = \frac{\alpha}{1 - \frac{\alpha}{3\pi}\ln\left(\frac{Q^2}{m^2}\right)}.$$

The effective coupling strength is seen to increase for large Q^2, that is small distances. This effect is small in QED and the use of the running coupling constant does not significantly improve results, however in Quantum Chromodynamics, or QCD, it becomes important.

Another type of infinity arises in attempting to calculate the diagram shown in figure 1.5. This time the divergence occurs as the emission angle or momentum of the bremsstrahlung photon becomes very small, this is thus termed an infra-red divergence. The problem is not as fundamental as that above as this infinity

The above is an example of the process known as renormalization and can in QED be performed systematically order by order to remove all the infinities which occur (Schwinger, 1958).

In addition to the above some q^2 dependence may be included in the definition of the coupling constant. As the amplitudes for the diagrams in figures 1.3 and 1.4 are the same but for the modification to the propagator, using a running coupling constant

$$\alpha'_R(q^2) = \alpha_m(\mu^2)\left[1 - \frac{\alpha_m(\mu^2)}{15\pi}\frac{q^2}{m^2} + O(\alpha_m^2(\mu^2))\right]$$

where μ is some reference momentum transfer, would include the effects of the vacuum polarization graph in the lowest order calculation. For $q^2 >> m^2$ this becomes approximately (Bjorken and Drell, 1964)

$$\alpha''_R(Q^2) = \alpha\left[1 + \frac{\alpha}{3\pi}\ln\left(\frac{Q^2}{m^2}\right)\right]$$

where the subscript m has been dropped, the use of the renormalized coupling constant being implicit, and the positive quantity $Q^2 = -q^2$ is introduced for convenience. Similar expressions may be calculated for higher orders and the most significant parts, the leading log terms, combined to give

$$\alpha_R(Q^2) = \frac{\alpha}{1 - \frac{\alpha}{3\pi}\ln\left(\frac{Q^2}{m^2}\right)}.$$

The effective coupling strength is seen to increase for large Q^2, that is small distances. This effect is small in QED and the use of the running coupling constant does not significantly improve results, however in Quantum Chromodynamics, or QCD, it becomes important.

Another type of infinity arises in attempting to calculate the diagram shown in figure 1.5. This time the divergence occurs as the emission angle or momentum of the bremsstrahlung photon becomes very small, this is thus termed an infrared divergence. The problem is not as fundamental as that above as this infinity

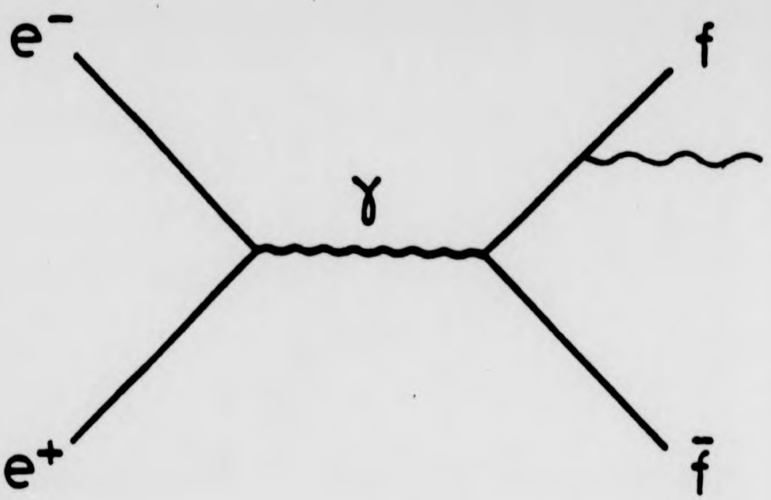

Figure 1.5. Photon radiation from a final state fermion.

cancels with others that appear when all the terms to this order are calculated. In calculating the above diagram alone a cut-off may be introduced to get rid of the infinite part. This is justifiable as the divergence is associated with just the parts of the process that are not measurable. It is impossible to distinguish between an electron and an electron that is accompanied by a photon of momentum less than that experimentally resolvable.

Historically QED was not developed using the gauge principle as described here, rather gauge invariance was noticed to be a feature of the theory (Fock, 1927). Two theories constructed using the gauge principle are briefly described in the following. In these theories the symmetries involved are those of higher dimensional non-Abelian groups, and in such cases the gauge principle turns out to be even more powerful in constraining the form of the theories. For further discussion of the group theoretic terms used see Gibson and Pollard (1976).

Generalization of the Covariant Derivative and QCD.

Consider a Lagrangian L formulated to describe the behaviour of a free field ϕ. If L is invariant when ϕ is globally transformed according to an n-dimensional representation of the group G, that is under

$$\phi(x) \rightarrow \phi'(x) = \exp\left[-ig\theta_a t^a\right]\phi(x)$$

then the covariant derivative is defined to be

$$D^\mu = \partial^\mu + igt^a W^{a\mu}(x).$$

(Sub or superscripts $a, b, \ldots$ are used to indicate group indices and summation is implied over repeated indices, whether they are 'up' or 'down' having no significance.) The t^a are $n \times n$ matrices obeying the algebra

$$[t^a, t^b] = if_{abc}t^c$$

where the f_{abc} are the structure constants of G. The W are the gauge fields, equivalent to the electromagnetic potential in QED, and transform according to

$$W_\mu(x) \rightarrow W'_\mu(x) = -i\exp\left[-ig\theta(x)\cdot t\right]\partial_\mu \exp\left[+ig\theta(x)\cdot t\right] + \exp\left[-ig\theta(x)\cdot t\right]W_\mu(x)\exp\left[+ig\theta(x)\cdot t\right]$$

the dot product being over the group indices $1 \ldots n$. Generalising the field tensor to

$$F^{a\mu\nu} = \partial^\mu W^{a\nu} - \partial^\nu W^{a\mu} - g f_{abc} W^{b\mu} W^{c\nu},$$

the Yang-Mills term in the Lagrangian has the form

$$L_{YM} = -\frac{1}{4} F^a_{\mu\nu} F^{a\mu\nu}.$$

Consider the use of these expressions in generating a theory of the strong interactions, QCD.

There are experimental reasons for believing that quarks have associated with them a degree of freedom called colour. For example this solves the problem of the apparent violation of the Pauli exclusion principle in baryons containing three quarks of the same type; the quarks may have different colour quantum numbers. The number of colours may be deduced from the ratio of the quark to the lowest order QED muon production cross-section in e^+e^- annihilation

$$R = \frac{\sigma(e^+e^- \rightarrow q\bar{q})}{\sigma_0(e^+e^- \rightarrow \mu^+\mu^-)}.$$

Experimentally this is found to be approximately three times the number of quark flavours that are produced, suggesting that there are three colours. The same result can be deduced from a study of the π^0 lifetime. QED calculations of the expected rate of the decay $\pi^0 \rightarrow \gamma\gamma$ assuming the π^0 to be composed of mixtures of charged quarks and anti-quarks give a lifetime that is approximately three squared times too large, unless the three colours are included. For further discussion of this and other pointers to an SU(3) colour symmetry, see Gell-Mann (1960) and Close (1979).

Adding the colour degrees of freedom a quark field may be written as

$$\psi_i = \begin{pmatrix} q_i^R \\ q_i^B \\ q_i^G \end{pmatrix}$$

where i runs over the flavours $d, u, s, c, b \ldots$ and R, B and G stand for the three colours. The free field Lagrangian

$$L = \sum_{i=d,u,s\ldots} \bar{\psi}_i (i\gamma^\mu \partial_\mu - m_i)\psi_i$$

then displays invariance under arbitrary variations of 'colour phase'

$$\psi_i \rightarrow \psi_i' = \exp\left[-ig_S \theta^a \frac{\lambda^a}{2}\right].$$

As there are three colours, not just one phase as in QED, the 'colour phase' changing quantity is not just a simple number. In fact the $\lambda^a/2$ are matrices which represent the symmetry of the above transformation: SU(3). There are eight matrices in all as the group SU(3) has eight generators, that is in order to be able to make arbitrary rotations in an SU(3) space, eight operators are necessary. In the case above these matrices must have dimension 3×3, as the quark fields are three dimensional. Formally the matrices satisfy the algebra

$$\left[\frac{\lambda^a}{2}, \frac{\lambda^b}{2}\right] = i f_{abc} \frac{\lambda^c}{2},$$

f_{abc} being the structure constants of SU(3). The θ, one for each of the generators, are parameters allowing the transformation to be made arbitrary. One possible representation of the λ matrices may be found in Gibson and Pollard.

Using the given prescription, the covariant derivative is

$$D^\mu = \partial^\mu + ig_S \frac{\lambda^a}{2} A^{a\mu}$$

where the gauge fields describe, in this case, gluons. Inserting the covariant derivative in the free field Lagrangian produces a new Lagrangian, containing interaction

terms. This is invariant under the local version of the SU(3) 'colour phase' transformation, in which $\theta \rightarrow \theta(x)$, provided the gluon fields transform according to the general prescription given for gauge fields. Adding the Yang-Mills term the Lagrangian is

$$L = \sum_i \overline{\psi}_i (i\gamma^\mu \partial_\mu - m_i - g_S \frac{\lambda^a}{2} \gamma^\mu A^a_\mu)\psi_i - \frac{1}{4} F^a_{\mu\nu} F^{\mu\nu}_a .$$

The $F^a_{\mu\nu}$ are defined by

$$F^a_{\mu\nu} = \partial_\mu A^a_\nu - \partial_\nu A^a_\mu - g_S f_{abc} A^b_\mu A^c_\nu .$$

The first two terms are of the same form as those responsible for the Maxwell equations in QED, the last describes interactions among the gluons themselves. This new feature arises as in QCD the gauge fields, the gluons, are found to carry colour charge, while the gauge fields of QED, the photons, are neutral.

The quantity g_S is the strong interaction gauge coupling constant. To ensure local gauge invariance, it must have the same value for all flavours and also in the Yang-Mills sector. This illustrates the fact that for non-Abelian symmetries the principle of local gauge invariance is more powerful than in the case of Abelian symmetries. In QED, an example of the latter, there is no a priori reason why different matter fields should not couple to the gauge field with different strengths, nor any reason why those strengths should be quantized in units of the electronic charge.

The Lagrangian above is not the complete Lagrangian of QCD. A term of the form

$$\theta \epsilon^{\mu\nu\rho\sigma} F^a_{\mu\nu} F^a_{\rho\sigma}$$

may be added without destroying the local gauge invariance (Llewellyn-Smith, 1982). θ is an arbitrary parameter that must be determined by experiment. Also when the complex problem of quantizing the vector gauge fields is tackled (see,

for example, Aitchison) it is found that gauge fixing, or ghost, terms have to be added to the Lagrangian. The above form is however adequate for all QCD tree level Feynman graphs. These are listed in Aitchison and Hey. Further discussion of QCD may be found in Pennington (1983).

Confinement and Asymptotic Freedom.

Renormalization may be carried out in QCD in a manner similar to that illustrated for QED, though it is not the most economical method (t'Hooft, 1971a). The leading log expression for the running coupling constant in QCD is

$$\alpha_S(Q^2) = \frac{\alpha_S(\mu^2)}{1 + \frac{\alpha_S(\mu^2)}{12\pi}(33 - 2f)\ln\left(\frac{Q^2}{\mu^2}\right)}$$

where f is the number of quark flavours. Introducing

$$\ln(\Lambda^2) = \ln(\mu^2) - \frac{12\pi}{(33 - 2f)\alpha_S(\mu^2)}$$

this may be written

$$\alpha_S(Q^2) = \frac{12\pi}{(33 - 2f)\ln\left(\frac{Q^2}{\Lambda^2}\right)}$$

with Λ of the order of $300MeV$ (Hill, 1985).

It can be seen that, for $f \leq 16$, $\alpha_S(Q^2)$ tends to zero as Q^2 tends to infinity. This is the phenomenon of asymptotic freedom and implies that, to high energy probes, quarks will appear to be free inside protons, explaining the success of the quark-parton model (Close, 1979). Also, for large Q^2, perturbation theory is valid and quantites such as the cross-section for quark anti-quark gluon production in e^+e^- annihilation may be calculated.

For small Q^2, $\alpha_S(Q^2)$ becomes large and the perturbative expansion is no longer valid. Attempts are being made to solve the theory in this region using discrete approximations to the fields involved (Kogut, 1983). It is hoped the increase of the coupling strength at low momentum transfers indicates that QCD

explains confinement, namely the fact that no free colour charges are seen. This certainly seems to represent the experimental situation, only one experiment having reported evidence for free quarks (Fairbank, 1981) despite extensive searches (see, for example, Bartel, 1980).

In order to relate calculations in perturbative QCD involving quarks and gluons to the experimentally observed particles, models of the confinement process have been developed. In e^+e^- annihilation these are concerned with how a jet of particles is produced from the initial quarks and gluons and the process is termed hadronization, or fragmentation. The hadronization model used in the following is that developed by the Lund group and will be described in the section on the Monte-Carlo. It is based on a solvable model which exhibits confinement, the Schwinger model (Schwinger, 1962). This is QED in one space and one time dimension. In this theory if a positive and negative particle are moved away from one another then, as in one spatial dimension the electronic field strength is independent of the separation between the particles, eventually the field energy is enough to polarize the vacuum, generating two dipoles and confining the charge.

The Glashow-Salam-Weinberg Model.

In developing a theory of electroweak interactions the problem of finding the symmetries involved is complicated by the fact that the particles that belong together in multiplets do not have the same masses. Clues to the symmetry must be sought in the relationships between the coupling strengths of the interactions to the different particles. The symmetries used in the currently accepted picture, the Glashow-Salam-Weinberg or GSW model, were first recognised by Glashow (1961).

Glashow saw that two symmetries are involved. The first is the $SU(2)_L$ symmetry observed in weak interactions, which is seen in that the couplings of the weak interaction to many different particles have the same strength and may be

mathematically expressed by the statement that (charged) weak interactions are invariant under global transformations of the form

$$\psi_L \rightarrow \psi'_L = \exp\left[-ig\theta \cdot \frac{\tau}{2}\right]\psi_L$$

where

$$\psi_L = \begin{pmatrix} \nu_e \\ e \end{pmatrix}_L, \begin{pmatrix} \nu_\mu \\ \mu \end{pmatrix}_L, \begin{pmatrix} \nu_\tau \\ \tau \end{pmatrix}_L$$
$$= \begin{pmatrix} u \\ d' \end{pmatrix}_L, \begin{pmatrix} c \\ s' \end{pmatrix}_L, \begin{pmatrix} t \\ b' \end{pmatrix}_L.$$

The subscript L denotes that only the left handed, or negative, chiral, or helicity, states are involved. This observation is the result of much experimental effort, as is described by Perkins (1982).

As the ψ_L are doublets the representation of $SU(2)_L$ involved is two dimensional, a suitable choice for the τ are therefore the Pauli matrices, which satisfy the required $SU(2)_L$ algebra

$$\left[\frac{\tau^a}{2}, \frac{\tau^b}{2}\right] = if_{abc}\frac{\tau^c}{2}.$$

One representation of these matrices is given in Gibson and Pollard. The second symmetry involved is the U(1) symmetry of the electromagnetic interactions. Invariance is observed under global transformations of the form

$$\psi \rightarrow \psi' = \exp\left[-ig'\theta\right]\psi.$$

Invariance of the Lagrangian under the local version of this second transformation may be demanded in order to generate QED as has already been shown. A similar procedure may be followed using the $SU(2)_L$ transformation in an attempt to generate a theory of the weak interactions. If this is done then three gauge fields will be introduced as there are three generators of the group $SU(2)_L$. Two of these fields will be electrically charged and one will be neutral. All of them will only couple to left-handed states, that is to particles whose spin and momentum

directions are anti-parallel, as only these particles can be placed in $SU(2)_L$ doublets. This does not correctly represent nature, it is known that the neutral weak interaction also couples to right-handed states (Perkins, 1982).

Glashow's proposal provides a way out of this dilemma. A theory with the gauge group $SU(2)_L \times U(1)$ must be generated by simultaneously demanding invariance of the Lagrangian under both the $SU(2)_L$ and the U(1) local gauge transformations. In this case the $SU(2)_L$ and U(1) sectors of the theory are connected. The $SU(2)_L$ symmetry is named weak isospin in analogy with the approximate SU(2) isospin symmetry evident in the hadron spectrum. The quantum numbers are conventionally labelled t and t_3 for the total weak isospin and its third component respectively. The U(1) symmetry is called weak hypercharge, again in analogy with the hadronic case, and its quantum numbers are labelled y. The relationship between t_3, y and the electronic charge q of a particle is

$$q = t_3 + \frac{y}{2}.$$

The correct form for the neutral weak interactions then arises through mixing of the weak isospin and weak hypercharge sectors. The required local gauge invariance is obtained by using a covariant derivative of the form

$$D^\mu = \partial^\mu + igT^{(t)} \cdot W^\mu + i\frac{g'}{2} y B^\mu.$$

The weak isospin and weak hypercharge assignments are:-

Particles	t	t_3	y	q
ν_e, ν_μ, ν_τ	+1/2	+1/2	−1	0
e_L, μ_L, τ_L	+1/2	−1/2	−1	−1
e_R, μ_R, τ_R	0	0	−2	−1
u_L, c_L, t_L	+1/2	+1/2	+1/3	+2/3
d'_L, s'_L, b'_L	+1/2	−1/2	+1/3	−1/3
u_R, c_R, t_R	0	0	+4/3	+2/3
d'_R, s'_R, b'_R	0	0	−2/3	−1/3

Substituting

$$T^{(0)} = 0$$

$$T^{(1/2)} = \frac{\tau}{2}$$

in the above expression for the covariant derivative gives

$$D^{\mu} = \partial^{\mu} + ig\frac{\tau}{2} \cdot W^{\mu} - i\frac{g'}{2} B^{\mu}$$

for left handed leptons and

$$D^{\mu} = \partial^{\mu} - ig' B^{\mu}$$

for right handed leptons. As required, the charged weak gauge bosons can only couple to left-handed helicity states, while mixing the B field with the neutral part of the weak gauge field W_3 allows neutral weak current interactions to occur in both sectors.

In addition to the problem of introducing the correct mixing between B and W_3, the weak gauge bosons must be given masses in order to explain the short range of weak interactions. These goals may be accomplished, as suggested by Weinberg (1967) and Salam (1968), without destroying the local gauge invariance crucial to the renormalizability of the theory, by using the Higgs mechanism.

An isospinor with $(t, t_3) = (1/2, \pm 1/2)$ and $y = 1$ composed of four scalar fields is introduced

$$\phi = \frac{1}{\sqrt{2}} \begin{pmatrix} \phi_1 + i\phi_2 \\ \phi_3 + i\phi_4 \end{pmatrix}$$

which may also generally be written

$$\phi = \exp\left[i\theta(x) \cdot \frac{\tau}{2}\right] \begin{pmatrix} 0 \\ \rho(x) \end{pmatrix}.$$

The behaviour of this field is described by the Lagrangian

$$L_H = (\partial_{\mu}\phi)^{\dagger}(\partial^{\mu}\phi) + \frac{1}{2}\mu^2\phi^{\dagger}\phi - \frac{1}{2}\lambda^2(\phi^{\dagger}\phi)^2.$$

The reasoning which led to the introduction of this system, with the behaviour described in the above Lagrangian, is discussed in both Aitchison and Aitchison and Hey.

The peculiarity of the above which makes it possible to introduce the necessary particle masses is that it has a non-zero vacuum expectation value. This may be written

$$\langle 0|\phi(x)|0\rangle = \begin{pmatrix} 0 \\ \frac{1}{\sqrt{2}}(f+\sigma(x)) \end{pmatrix}$$

where the freedom to choose the gauge has been exploited in order to make the form particularly simple. It should be noted that the above holds strictly only classically, it is assumed that the result carries over to the quantum case (but see the discussion in Guralnik). Replacing the ordinary derivative in L_H by its covariant form gives a Lagrangian L'_H in which there are terms describing interactions between the scalar field ϕ and the W and B fields. If the ϕ field is set to its vacuum expectation value this becomes

$$\begin{aligned} L'_H =& \frac{1}{2}\partial_\mu\sigma\partial^\mu\sigma - \frac{1}{2}\mu^2\sigma^2 \\ &+ \frac{1}{8}f^2g^2(W^1_\mu W^{1\mu} + W^2_\mu W^{2\mu}) \\ &+ \frac{1}{8}f^2(gW^3_\mu - g'B^\mu)(gW^{3\mu} - g'B^\mu) + \ldots . \end{aligned}$$

This contains terms describing, on the first line, a scalar field σ of mass μ (the Higgs boson) and on the second line, the charged parts of the W field, which have acquired a mass of

$$M_W = \frac{1}{2}fg.$$

The third line shows that the neutral component of the W field and the B field are mixed. Introducing the linear combinations

$$Z_\mu = \cos\theta_W W^3_\mu - \sin\theta_W B_\mu$$

and

$$A_\mu = \sin\theta_W W^3_\mu + \cos\theta_W B_\mu$$

where

$$\tan\theta_W = \frac{g'}{g}$$

reveals the mass eigenstates, with

$$M_Z = \frac{1}{2} f \sqrt{g^2 + g'^2}$$
$$= \frac{M_W}{\cos\theta_W}$$

and

$$M_A = 0.$$

These are, respectively, the neutral weak boson and photon fields. Writing the covariant derivative in terms of these fields

$$D_\mu = \partial_\mu + ig\sin\theta_W \left(t_3^{(t)} + \frac{y}{2}\right) A_\mu + i\frac{g}{\cos\theta_W}\left[\cos^2\theta_W t_3^{(t)} - \frac{y}{2}\sin^2\theta_W\right] Z_\mu + \ldots$$

enables the quantity $g\sin\theta_W$ to be identified with the charge e (compare the above with the QED covariant derivative) and the couplings of the left and right components of the various fields to the Z^0 to be picked out.

It is also necessary to give masses to the fermions of the theory. This may be done without spoiling the local gauge invariance by the addition of a term of the form

$$-\frac{\sqrt{2}m_f}{8}\left(\bar{\psi}_R(f)\phi^\dagger\psi_L(f) + \bar{\psi}_L(f)\phi\psi_R(f)\right)$$

for each fermion f. Inserting the vacuum expectation value for ϕ this becomes

$$-m_f(\bar{\psi}_R(f)\psi_L(f) + \bar{\psi}_L(f)\psi_R(f)) + \cdots = -m_f\bar{\psi}\psi + \ldots$$

the required mass term (plus a term describing interactions between the fermion and the Higgs boson σ in which the coupling strength is proportional to the fermion mass).

The $t_3 = -1/2$ components of the left-handed quark spinors have been consistently written with a prime. This is because the eigenstates of the electroweak

interactions are not the same as those of the strong interaction. Conventionally the phases are so chosen that the $q = 2/3$ components are the same as the strong eigenstates and mixing then occurs between the $q = -1/3$ components. This mixing may be expressed by

$$\begin{pmatrix} d' \\ s' \\ b' \end{pmatrix} = \mathbf{V} \begin{pmatrix} d \\ s \\ b \end{pmatrix}$$

where the matrix

$$\mathbf{V} = \begin{pmatrix} V_{ud} & V_{us} & V_{ub} \\ V_{cd} & V_{cs} & V_{cb} \\ V_{td} & V_{ts} & V_{tb} \end{pmatrix}$$

must be unitary. This constrains the values of the matrix elements in such a way that they may be parameterized using three angles θ_1, θ_2 and θ_3 and a phase δ (Kobayashi and Maskawa, 1973). Writing $s_1 = \sin\theta_1, c_1 = \cos\theta_1$ etc. the matrix is then

$$\mathbf{V} = \begin{pmatrix} c_1 & -s_1c_3 & -s_1s_3 \\ s_1c_2 & c_1c_2c_3 - s_2s_3e^{i\delta} & c_1c_2s_3 + s_2c_3e^{i\delta} \\ s_1s_2 & c_1s_2c_3 + c_2s_3e^{i\delta} & c_1s_2s_3 - c_2c_3e^{i\delta} \end{pmatrix}.$$

Adding the Yang-Mills term to the elements discussed in the above gives the classical field Lagrangian of the GSW model. Again this is not the complete Lagrangian, as when the fields are quantized gauge fixing terms must be added to it.

The renormalizability of this theory was proved by t'Hooft (1971b). Feynman rules for all the tree level graphs are listed in Aitchison and Hey.

Significant support was lent to the GSW model by the discovery of the W and Z bosons (Arnison 1983, Banner 1983, Bagnaia 1983). The masses quoted for these bosons are currently[1] (UA1, UA2, 1985)

$$M_W = 81.5 \pm 1.4\, GeV/c^2$$

$$M_Z = 92.6 \pm 1.7\, GeV/c^2$$

[1]The results of the UA1 and UA2 groups are combined, statistical and systematic errors being added in quadrature.

which give

$$\sin^2 \theta_W = 0.225 \pm 0.014$$

in excellent agreement with results from neutrino scattering measurements, from which (CHARM, 1985)

$$\sin^2 \theta_W = 0.215 \pm 0.10 .$$

Chapter 2

Electron Positron Annihilation

Introduction.

When an electron and a positron collide at high energy several interactions may occur. The lowest order QED Feynman diagrams for which, in decreasing order of likelihood of the process in question, are illustrated in figures 2.1, 2.2 and 2.3. The reaction 2.1, an example of a two-photon interaction, is of interest here only in that it is a background to the processes studied. For more information concerning such reactions, particularly those in which the final state is multihadronic, see Cartwright (1983).

The graphs 2.2 and 2.3 in the case that the final state fermions are an electron and a positron are the lowest order diagrams describing Bhabha scattering, $e^+e^- \rightarrow e^+e^-$, which is used by the JADE experiment to monitor the luminosity. This will be discussed further in the following chapter.

Quark Production and the c and b Asymmetries.

The interaction of interest here is that represented by the graphs 2.3 and 2.4, when the final state fermions are $c\bar{c}$ or $b\bar{b}$. The differential cross-section for the annihilation of high energy unpolarised electrons and positrons into these final states, calculated from the Feynman diagrams shown, is

$$\frac{d\sigma_f}{d\Omega} = \frac{\alpha^2}{4s}\left[C_1(1+\cos^2\theta) + C_2\cos\theta\right]$$

where initial and final state particle masses have been ignored. In the above $\alpha = e^2/(4\pi)$ is the electromagnetic coupling constant, s is the square of the sum of the electron and positron energies, that is the centre of mass energy squared and θ is the angle between the outgoing fermion's direction and the direction of the incoming electron, as illustrated in figure 2.5.

The coefficients C_1 and C_2 are given by

$$C_1 = q_f^2 - 2q_f v_e v_f \mathrm{Re}(\chi) + (v_e^2 + a_e^2)(v_f^2 + a_f^2)|\chi|^2$$

and

$$C_2 = -4q_f a_e a_f \mathrm{Re}(\chi) + 8v_e v_f a_e a_f |\chi|^2$$

where q_f is the electric charge of the fermion and a_e and a_f are the axial couplings of the Z^0 to the electron and fermion respectively, v_e and v_f being their vector counterparts. These couplings, in terms of which the differential cross-section is more conveniently expressed than the left and right handed couplings g_L and g_R previously used, may be obtained from

$$a = 2(g_R - g_L)$$

$$v = 2(g_R + g_L).$$

Reading the g_L and g_R from the neutral part of the weak covariant derivative given in chapter one it can be seen that $a = 1$ for the $t_3 = 1/2$ components of the weak isospinors and $a = -1$ for the $t_3 = -1/2$ components. The vector coupling constants are then given by

$$v_f = a_f - 4q_f \sin^2\theta_W.$$

The axial and vector couplings are:-

Particle f	q_f	a_f	v_f	v_f $(\sin^2\theta_W = 0.225)$
ν_e, ν_μ, ν_τ	0	+1	+1	+1.000
e, μ, τ	−1	−1	$-1 + 4\sin^2\theta_W$	−0.100
d, s, b	−1/3	−1	$-1 + \frac{4}{3}\sin^2\theta_W$	−0.700
u, c, t	+2/3	+1	$+1 - \frac{8}{3}\sin^2\theta_W$	+0.400

χ may be defined as

$$\chi = \frac{1}{16\sin^2\theta_W \cos^2\theta_W}\left(\frac{s}{s - M_Z^2 + iM_Z\Gamma_Z}\right).$$

Another parameterization is also commonly used (see, for example, Wetzel 1983). These two parameterizations give the same results when fully calculated to all orders, and are identical at the tree level, but the manner in which the corrections due to higher order diagrams are applied is not the same and care must be taken in comparing results using the different schemes (Cashmore, 1985). That above will be used throughout this thesis. In this case the relationship

$$\sin^2\theta_W = 1 - \frac{M_W^2}{M_Z^2}$$

holds to all orders.

The terms in the differential cross-section proportional to χ^2 are those which arise from the weak diagram 2.4, those proportional to χ are due to the interference between the weak diagram and the electromagnetic diagram 2.3 and the remaining term is due to the lowest order QED diagram.

Integrating the differential cross-section gives the total cross-section

$$\sigma_f = \frac{4\pi\alpha^2}{3s} C_1.$$

The term linear in $\cos\theta$ in the differential cross-section gives rise to an asymmetry in the number of fermions produced in the forward direction, with $\cos\theta > 0$, compared to the number produced in the backward direction, with $\cos\theta < 0$. Denoting these numbers N_F^f and N_B^f respectively, this may be expressed by

$$A_f = \frac{N_F^f - N_B^f}{N_F^f + N_B^f}$$

or

$$A_f = \frac{\int_0^1 \frac{d\sigma_f}{dx}\, dx - \int_{-1}^0 \frac{d\sigma_f}{dx}\, dx}{\sigma_f}$$

where $x = \cos\theta$. Performing the integrations gives

$$A_f = \frac{3}{8}\frac{C_2}{C_1}.$$

At PETRA energies these expressions may be considerably simplified. Firstly note that the measured width of the Z^0 (UA1, UA2, 1985), $\Gamma_Z \approx 3 GeV/c^2$, is much smaller than its mass, therefore to a good approximation

$$\chi = \frac{1}{16 \sin^2\theta_W \cos^2\theta_W} \left(\frac{s}{s - M_Z^2}\right).$$

Secondly, as $s << M_Z^2$, $|\chi|$ is small. Thirdly the measured value of $\sin^2\theta_W$ is close to $1/4$ and thus the vector coupling of the electron to the Z^0, $v_e = 1 - 4\sin^2\theta_W$ is small. Therefore, to an accuracy of better than one per cent for c quarks and five per cent for b quarks

$$\frac{d\sigma_f}{d\Omega} = \frac{\alpha^2}{4s}\left[q_f^2(1 + \cos^2\theta) - 4 q_f a_e a_f \chi \cos\theta\right]$$

$$\sigma_f = \frac{4\pi\alpha^2}{3s} q_f^2$$

and

$$A_f = -\frac{3}{2}\frac{a_e a_f}{q_f} \frac{1}{16 \sin^2\theta_W \cos^2\theta_W} \frac{s}{s - M_Z^2}.$$

For the c and b quarks the asymmetries calculated from the approximation above, at $35 GeV$ and using the values of the various parameters that have been given, are

$$A_c = -0.134$$

and

$$A_b = -0.269.$$

For comparison the results without approximation are

$$A_c = -0.133$$

and

$$A_b = -0.256.$$

The error introduced by using the approximation is in both cases smaller than that arising due to the errors with which the parameters $\sin\theta_W$ and M_Z have been measured. These give rise to an errors of ± 0.010 for A_c and ± 0.020 for A_b.

From the total cross-section above the ratio of flavours produced in electron positron annihilations can be seen to be at lowest order simply the ratio of the quark charges squared, only quarks with mass less than the beam energy being produced. At $35\,GeV$ the relative numbers of d, u, s, c and b are

$$N_d : N_u : N_s : N_c : N_b = 1 : 4 : 1 : 4 : 1 .$$

The ratio

$$R = \frac{\sigma(e^+e^- \rightarrow q\bar{q})}{\sigma_0(e^+e^- \rightarrow \mu^+\mu^-)}$$

may also be calculated and is, again to lowest order

$$R_0 = 3\sum_f q_f^2$$

where the sum runs over the quark flavours that may be produced at the energy in question. The factor three in this expression arises due to the three colour degrees of freedom of the quarks, as was mentioned in the first chapter. R, measured by several groups over a large energy range, is plotted in figure 2.6. The formula above does not give a particularly good fit to the data. A QCD correction to the lowest order expression is found to be significant and the above must be modified so that

$$R = R_0\left(1 + \frac{\alpha_S}{\pi}\right)$$

where the quark masses have been ignored. A good fit to the data is now obtained with $\alpha_S \approx 0.2$ at $35\,GeV$.

Corrections to the asymmetry arising from higher order electroweak diagrams, QCD and the quark masses must be considered to see if they have a significant effect on the result above. Electroweak corrections have been calculated by, among others, Brown et al. and Böhm and Hollik. Various of the diagrams shown in Cashmore (1985) were evaluated for the case that the final state fermions are muons,

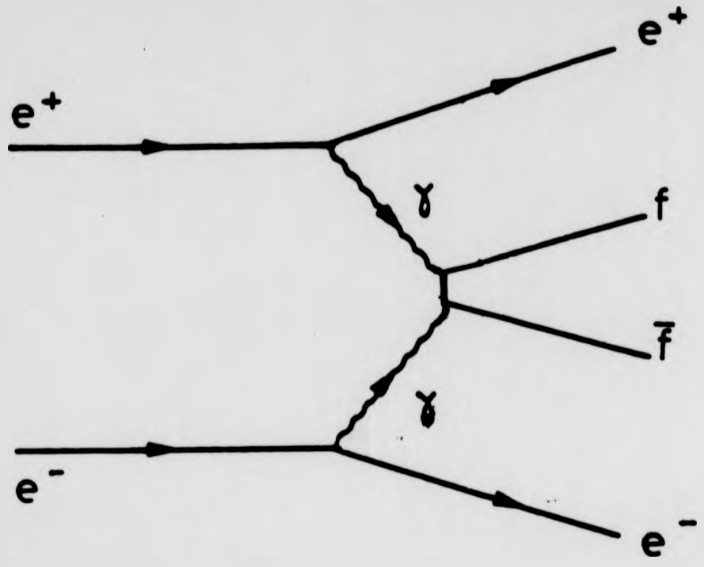

Figure 2.1. A two photon process.

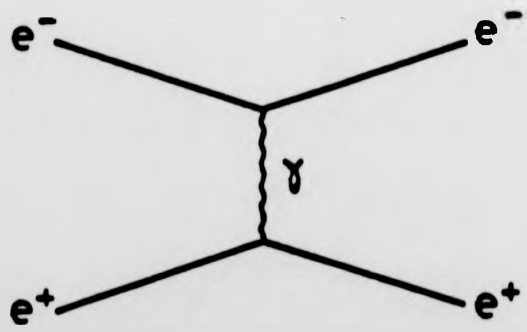

Figure 2.2. The lowest order QED electron-positron scattering diagram.

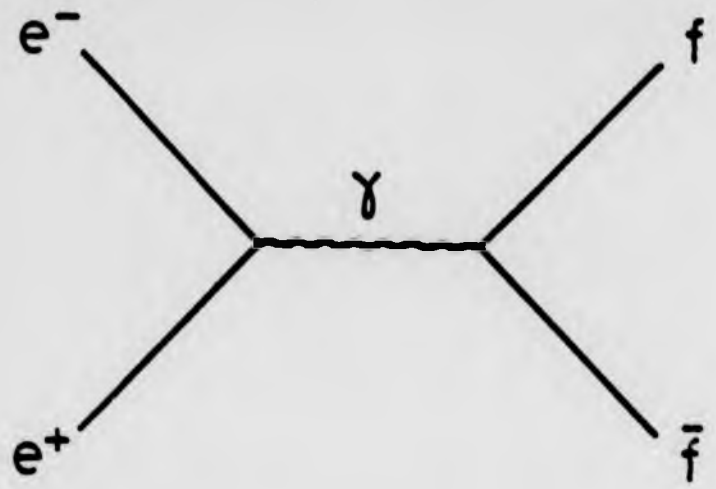

Figure 2.3. Lowest order QED electron-positron annihilation diagram.

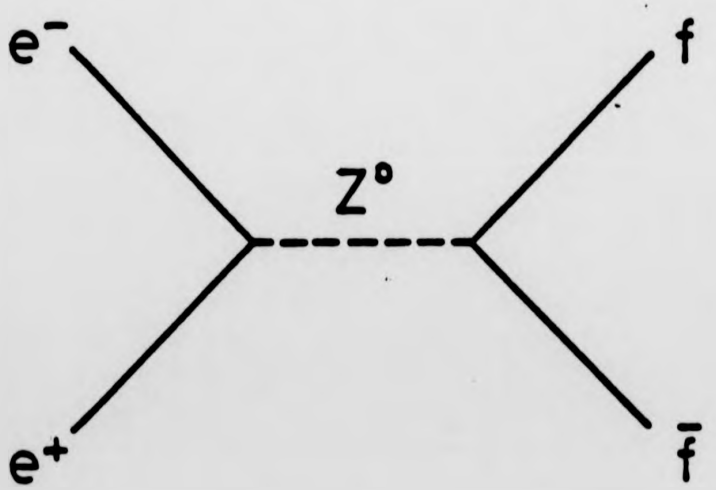

Figure 2.4. Lowest order Z^0 contribution to electron-positron annihilation.

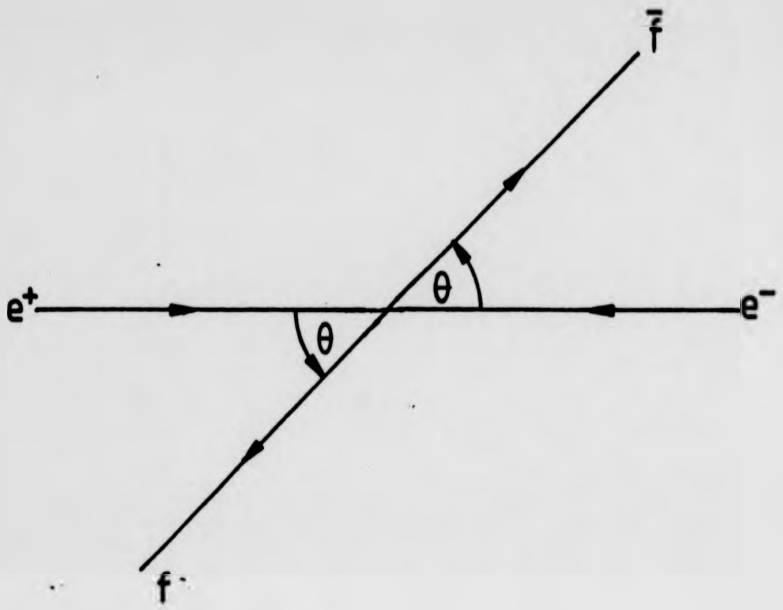

Figure 2.5. Definition of θ.

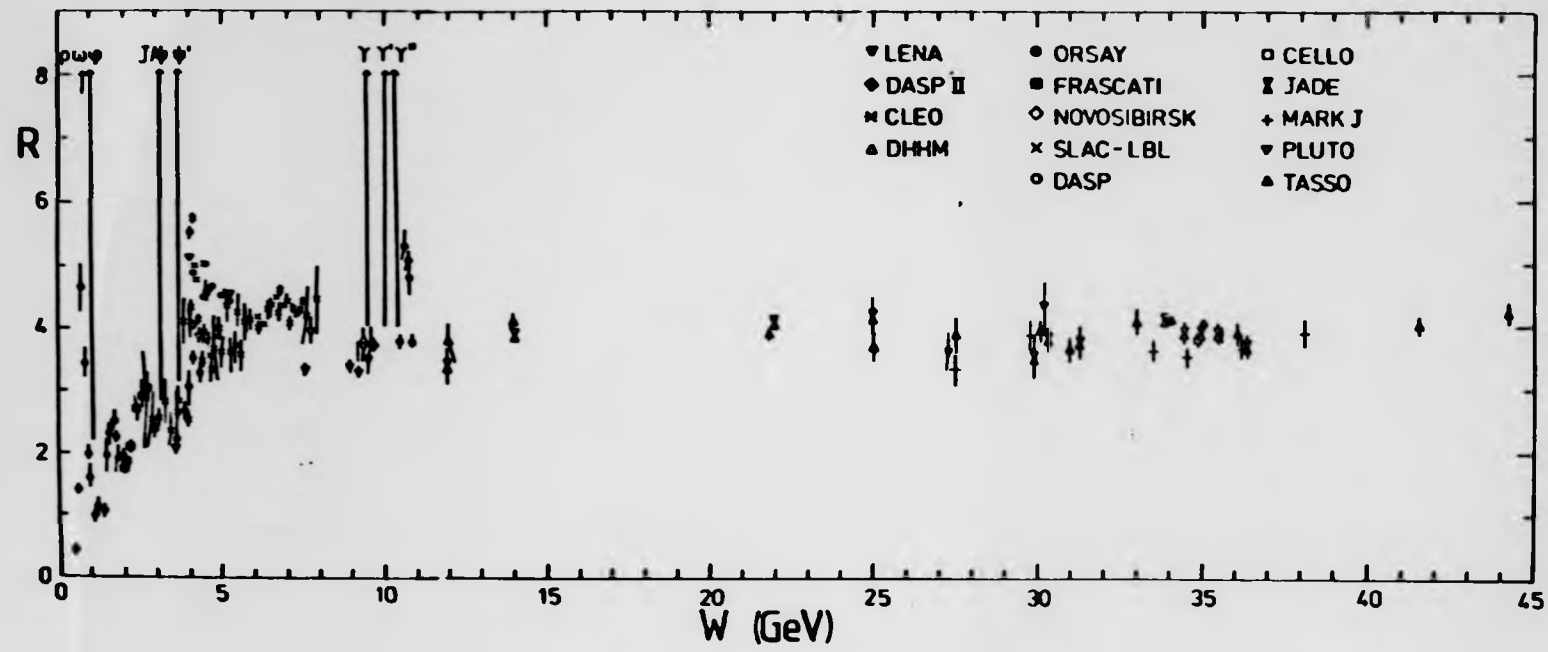

Figure 2.6. The ratio of the quark production cross section to the lowest order muon production cross section as a function of centre of mass energy.

consistent results being obtained. Taking the figures from the last reference, at a centre of mass energy of $35\,GeV$ and with other conditions also similar to those relevant to the measurement made here, the corrected asymmetry was found to be

$$A'_\mu = A_\mu + 0.017.$$

The correction consists of a component $+0.023$ from the higher order QED diagrams, and a component -0.006 from the weak and electroweak diagrams. The latter is dominated by the Z^0 self energy and is thus about the same for quarks. The QED correction is however smaller for quarks due to their smaller electric charge and greater mass. The net effect is that higher order electroweak effects approximately cancel in the c and b quark asymmetries.

Corrections due to including the phase-space factors for the fermion masses give

$$A_f(m_f) = \frac{2v}{3 - v^2} A_f(0)$$

where

$$v = \sqrt{1 - \frac{4m_f^2}{s}},$$

m_f being the fermion mass. Using $m_c = 1.35\,GeV/c^2$ and $m_b = 5.3\,GeV/c^2$ (Fritzsch, 1985) this results in a decrease of the asymmetries at $35\,GeV$ so that

$$A''_c = 0.994 A_c$$

$$A''_b = 0.911 A_b.$$

The effects on the asymmetry of the QCD processes illustrated in figure 2.7 have been calculated by Jersak (1981). At $\sqrt{s} = 35\,GeV$, making the approximations used previously, it is possible to parameterize the correction using

$$A'''_f = \left(\frac{\pi + \alpha_S r_f(\mu)}{\pi + \alpha_S t_f(\mu)} \right) A_f$$

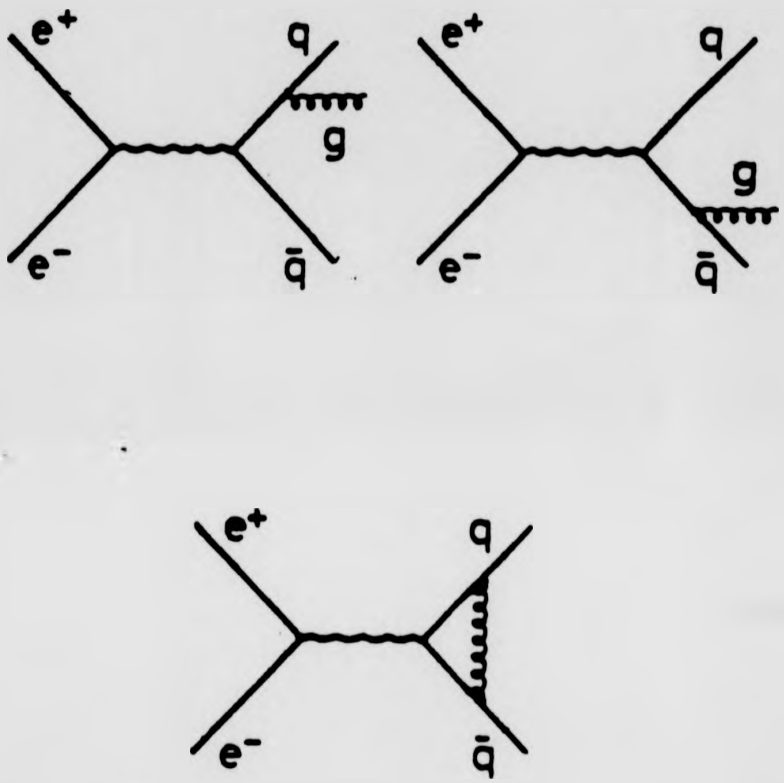

Figure 2.7. The QCD diagrams calculated in order to obtain the corrections to the quark asymmetries.

where $\mu = 2m_f/\sqrt{s}$ and at $35\,GeV$, using the quark masses above

$$r_c(\mu) = 0.2$$

$$t_c(\mu) = 1.0$$

$$r_b(\mu) = 1.15$$

$$t_b(\mu) = 1.3\,.$$

Using $\alpha_S = 0.16$

$$A_c''' = 0.96 A_c$$

$$A_b''' = 0.99 A_b.$$

Combining all these effects, the corrections amount to

$$A_c^{(1)} = k_c A_c$$

$$A_b^{(1)} = k_b A_b$$

where $k_c = 0.95$ and $k_b = 0.90$. The corrected values of the c and b asymmetries at $35\,GeV$ are

$$A_c^{(1)} = -0.126$$

and

$$A_b^{(1)} = -0.230$$

where the figures from the full asymmetry calculation have been used.

Having measured the asymmetries it can be seen that the quantites $a_e a_f/q_f$ may be determined. Assuming the quark charges to be $2/3$ and $-1/3$ as expected and supported by, for example, the previously discussed measurements of R, and using the result from $\nu_e e$ scattering $a_e = -1.02 \pm 0.12$ (Kim, 1981) enables determination of the a_f. (The result for a_e requires the use of information from $e^+e^- \rightarrow \mu^+\mu^-$ to resolve ambiguities as to which of a_e and v_e is dominant and the sign of a_e.)

Jets and Fragmentation.

The quarks produced according to the differential cross-section above are not seen as free particles. By some as yet not calculable process, hopefully eventually describable using non-perturbative QCD, they hadronize or fragment to produce a cone or jet of hadrons. Figure 2.8 shows an event in which this has occurred, the jets are clearly visible. Occasionally hard gluon radiation occurs and the gluon also hadronizes producing a jet, such an event is shown in figure 2.9.

A model that plausibly describes the hadronization process, based as previously stated on the Schwinger model, has been developed at the Lund university. The basic idea of this model is that the colour field between the separating quark and anti-quark may be represented by a massless relativistic string of constant energy per unit length. As the q and $\bar{q}$ move apart the energy of the string increases until it breaks, some of its energy being used to create a quark anti-quark pair $q'\bar{q}'$ at the freshly broken ends of the string. The polarity of the colour field is such that the q and $\bar{q}'$ are now connected by a colour string, as are the $\bar{q}$ and the q'. Further breaks may occur until the energy of the system is exhausted, resulting in the production of several colour singlet quark anti-quark pairs, or mesons. Baryons are produced when the string breaks with the production of a diquark anti-diquark pair. The ratio of baryon to meson production has been measured to be about 0.07 to one (Abrams, 1980). At the break the quark anti-quark, or diquark anti-diquark, are given equal but opposite momenta transverse to the string. The transverse momentum, p_T, distribution and the probability of producing the different flavours at the breaks being given by

$$p(m_T, p_T) = \frac{\pi}{\kappa^2} \exp\left(-\frac{\pi m_T^2}{\kappa}\right)$$

where m_T, the transverse mass, is defined by

$$m_T = \sqrt{m_q^2 + p_T^2}$$

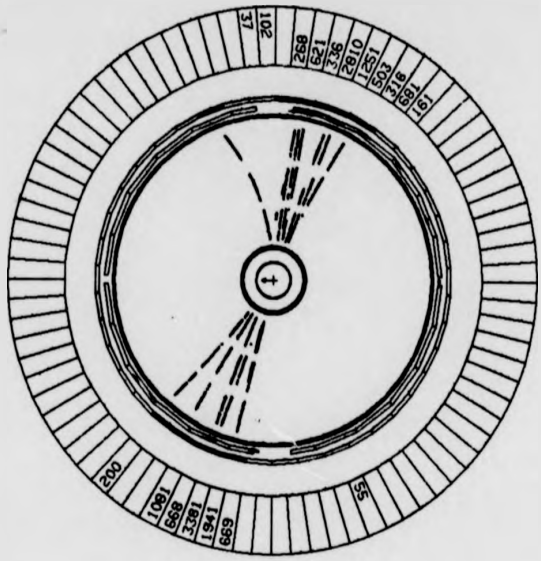

Figure 2.8. A two jet event.

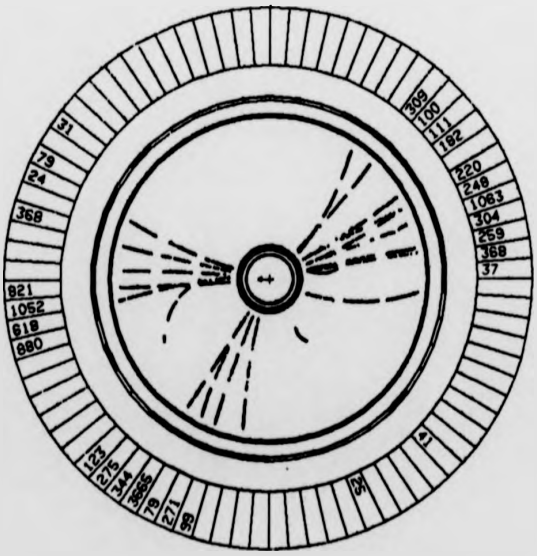

Figure 2.9. A three jet event.

and κ is the energy per unit length of the string. The quark masses, m_q, are chosen so that the ratio of production of flavours in the fragmentation is

$$N_d : N_u : N_s : N_c : N_b = 1.0 : 1.0 : 0.3 : 10^{-11} : 0.0$$

This gives good agreement with data (Bartel, 1983b).

Gluon production is represented by a kink in the string, which stretches from quark to gluon to anti-quark. On either side of the gluon a quark anti-quark pair form, resulting in two strings, one connected to the initial quark and one to the initial anti-quark, and a meson. The two strings then fragment in their centre of mass frames and finally all resulting particles are boosted back into the laboratory frame, which gives rise to three jet events if the gluon was sufficiently energetic.

The manner in which the longitudinal momentum, p_L, and energy, E, are shared among particles in a jet is desribed by the fragmentation function. This is written in terms of

$$z = \frac{(E + p_L)_{\text{hadron}}}{(E + p_L)_{\text{quark}}}$$

The symmetric Lund fragmentation function has the form

$$f(z)dz = N\frac{(1-z)^a}{z}\exp\left[-\frac{bm_T^2}{z}\right]dz$$

where N is a normalization constant and a and b are parameters determined by a fit to data. The probability that a meson, formed when a break in the string leaves an anti-quark attached to a quark q, has a fraction of the quark q's energy and longitudinal momentum in the range z to $z + dz$ is then $f(z)dz$. The remaining energy and longitudinal momentum are carried by the rest of the fragmenting system.

Kinematical arguments have been used to suggest that, for the heavy c and b quarks, a more suitable form for the fragmentation function is (Peterson, 1982)

$$f(z)dz = \frac{N_q}{z\left(1 - \frac{1}{z} - \frac{\epsilon_q}{1-z}\right)^2}dz$$

where the N_q are normalization factors and the parameters ϵ_q are expected to be given approximately by the mass of the light quark created as the string breaks divided by the mass of the heavy quark all squared.

Heavy Quark Decays.

In c and b events the hadrons containing the heavy quarks, generally D and B mesons respectively, decay weakly with lifetimes[1] (Schubert, 1984 and Bjorken, 1985)

$$\tau(D^{\pm}) = (8.3 \pm 1.0) \times 10^{-13}\, secs$$

$$\tau(D^{0}) = (3.60 \pm 0.35) \times 10^{-13}\, secs$$

$$\tau(B) = (12.6 \pm 1.9) \times 10^{-13}\, secs.$$

Note that $\tau(B)$ is actually the lifetime of the mix of mesons and baryons containing b quarks produced in electron-positron annihilations as it has not as yet proved possible to separate the contributions from these various particles. The mechanism whereby these decays occur is in general complicated due to non-perturbative QCD effects. The spectator diagram, illustrated in figure 2.10, is expected to be the dominant process. That it is not the only diagram of importance may be deduced from the difference between the D^0 and the $D^{\pm}$ lifetimes. If the identity of the light quark were of no consequence, as suggested by the spectator model, these would be the same.

The decays of particular interest in the following are the semi-leptonic ones $D \rightarrow l\nu_l X$ and $B \rightarrow l\nu_l X$. They occur primarily via the spectator diagram, the virtual W producing a lepton neutrino pair. The measured branching ratios for these decays are (Schubert, 1984 and Baines, 1985)

$$BR(D \rightarrow l\nu_l X) = (8.4 \pm 0.6)\%$$

$$BR(B \rightarrow l\nu_l X) = (11.7 \pm 0.5)\%.$$

[1]The measured B lifetime shows an alarming dependence on the accuracy of the device used to measure it, being smaller the more accurate the detector, see figure 3 Bjorken, 1985.

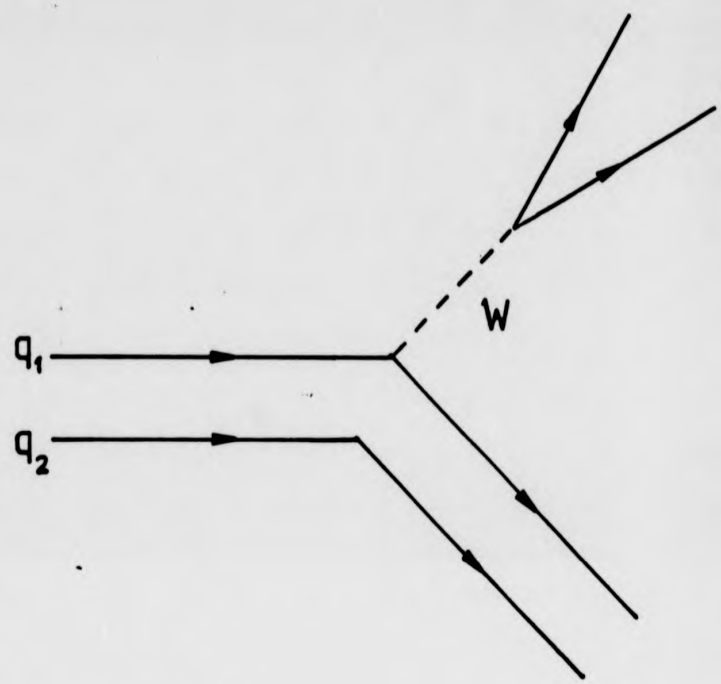

Figure 2.10. The spectator diagram.

The multiplicity of semi-leptonic B decays is found to be smaller than that of B decays in which no lepton is produced, as in the former a significant amount of the energy released in the decay is invested in a colourless pair of particles and thus is no longer available to the fragmentation process which is responsible for the production of many of the particles in the latter decay. Measurements give average charged multiplicities of (Schubert, 1984)

$$\overline{N}_{ch}(B \to Y) = 6.3 \pm 0.3$$

$$\overline{N}_{ch}(B \to l\nu_l X) = 4.1 \pm 0.4 .$$

A similar effect probably occurs in D decays, but it has not been studied. The average charged multiplicity in D decays is (Lüth, 1979)

$$\overline{N}_{ch}(D \to Y) = 2.5 \pm 0.1 .$$

The last point that must be made here is that, in the decays of B mesons, the b quark decay $b \to cW$ is much preferred over $b \to uW$. The ratio

$$r = \frac{BR(b \to uW)}{BR(b \to cW)}$$

has been measured by CLEO to be less than 5% at the 90% confidence level (Atarelli, 1982).

Chapter 3

The Accelerator and the Detector

PETRA.

Since its first operation in July 1978 to the present day, PETRA (an acronym for Positron Elektron Tandem Ring Anlage) has been the world's highest energy electron positron storage ring. As shown in figure 3.1 PETRA consists of eight straight sections of lead-shielded water-cooled vacuum pipe, four long and four short, connected by circular arcs in which in normal operation two bunches of electrons and two of positrons circulate in opposite directions. These bunches are steered round the arcs by dipole magnets, while alternate horizontally and vertically focussing quadrupole magnets prevent lateral bunch dispersal. Corrections for the incorrect focussing by the quadrupoles of slightly off-momentum particles are applied using sextupole magnets spaced regularly round the ring. Longitudinal bunch dispersal is prevented by the influences of synchrotron radiation loss and the acceleration system. The latter, composed of radio-frequency cavities, is housed on the long straight sections. The dimensions of PETRA are shown in figure 3.1. An introduction to the physics of accelerators may be found in Blewett (1977).

The injection schemes for PETRA are as follows. Electrons from an electron gun are accelerated in LINAC I to $40\,MeV$ and passed to the synchrotron (see figure 3.1) where they are accelerated to about $7\,GeV$. These may then be injected into PETRA. Positrons, produced by electron collisions with a metal target, are accelerated to $400\,MeV$ in LINAC II and then stored in the positron intensity accumulator until a sufficient number have been collected. These are then passed to the synchrotron and accelerated to about $7\,GeV$ after which they are injected into PETRA. The electron and positron beams are then simultaneously accelerated to the required energy. While this is taking place electrostatic sep-

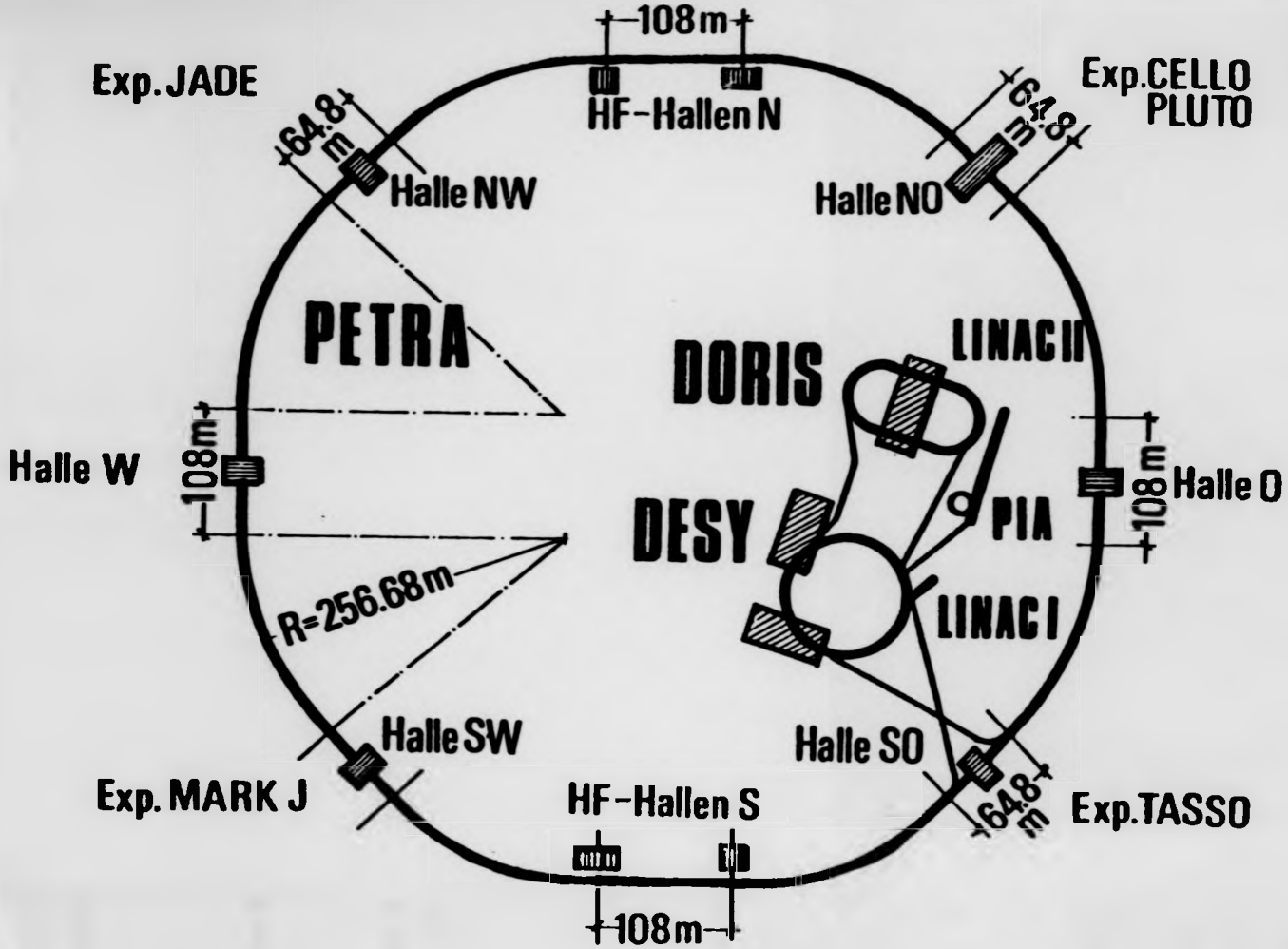

Figure 3.1. PETRA and the DESY accelerator complex.

arators at the experimental areas, where the bunches cross, are used to prevent the electron and positron beams from colliding. When collision energy has been reached these separators are switched off and the electron and positron bunches then pass through each other at the interaction regions. There are four of these, each equipped with a detector designed to study various aspects of the electron positron interactions which occur within them. The filling process takes typically twenty to thirty minutes.

The rate of interactions r for a process with cross-section σ is given by

$$r = \mathcal{L}\sigma$$

where $\mathcal{L}$ is the luminosity, the number of interactions per unit time per unit cross-section. At PETRA this is typically $4 \times 10^{30}\, cm^{-2}s^{-1}$. The rate at which multi-hadronic events occur is thus one or two per hour. The integrated luminosity

$$L = \int \mathcal{L}\, dt$$

determines the total number of events that are observed through

$$N = L\sigma.$$

The luminosity is monitored by observing the process of Bhabha scattering as this is theoretically well understood, experimentally easily recognised and has a relatively high rate at least at small polar angles.

The 24,000 multi-hadronic events used in this study were obtained in about one year of running time from an integrated luminosity of about $70\, pb^{-1}$.

JADE.

The JADE detector (JADE stood originally for a collaboration of JApanisch, Deutsch and Englisch institutes, nowadays the A stands for an Amerikanisch institute) is situated on the north-west straight section of the PETRA ring. The

detector, illustrated in figure 3.2, was designed to measure the momentum and energy loss per unit length of charged particles, the energy of photons and electrons and to identify penetrating particles, muons, over as large a solid angle as possible. It was hoped that the detector would thus be useable for a wide range of investigations.

At the time the data used in this analysis were collected, in the years 1980,1981 and 1982, the detector consisted of the following components:

(a) the beampipe counters;

(b) the central drift chamber, or Jet chamber;

(c) the time of flight, or TOF counters;

(d) the electromagnetic calorimeter;

(e) the muon system.

Components (a),(b) and (c) were surrounded by an aluminium solenoid which carried, during running, a current of about 7500 A producing a magnetic field, parallel to the beampipe, of 0.487 T. This field was measured and found to be constant to within better than 1% over the volume inside the inner detector. Measuring the curvature of the trajectory followed by a charged particle in this magnetic field enabled determination of its momentum. Outside the coil the magnetic field was contained in an iron return yoke. Stray fields, which might have affected the performance of photomultipliers for example, were kept at the level of $10^{-4}\,T$ or lower.

The remaining detector components were:

(f) the forward muon counters;

(g) the tagging counters.

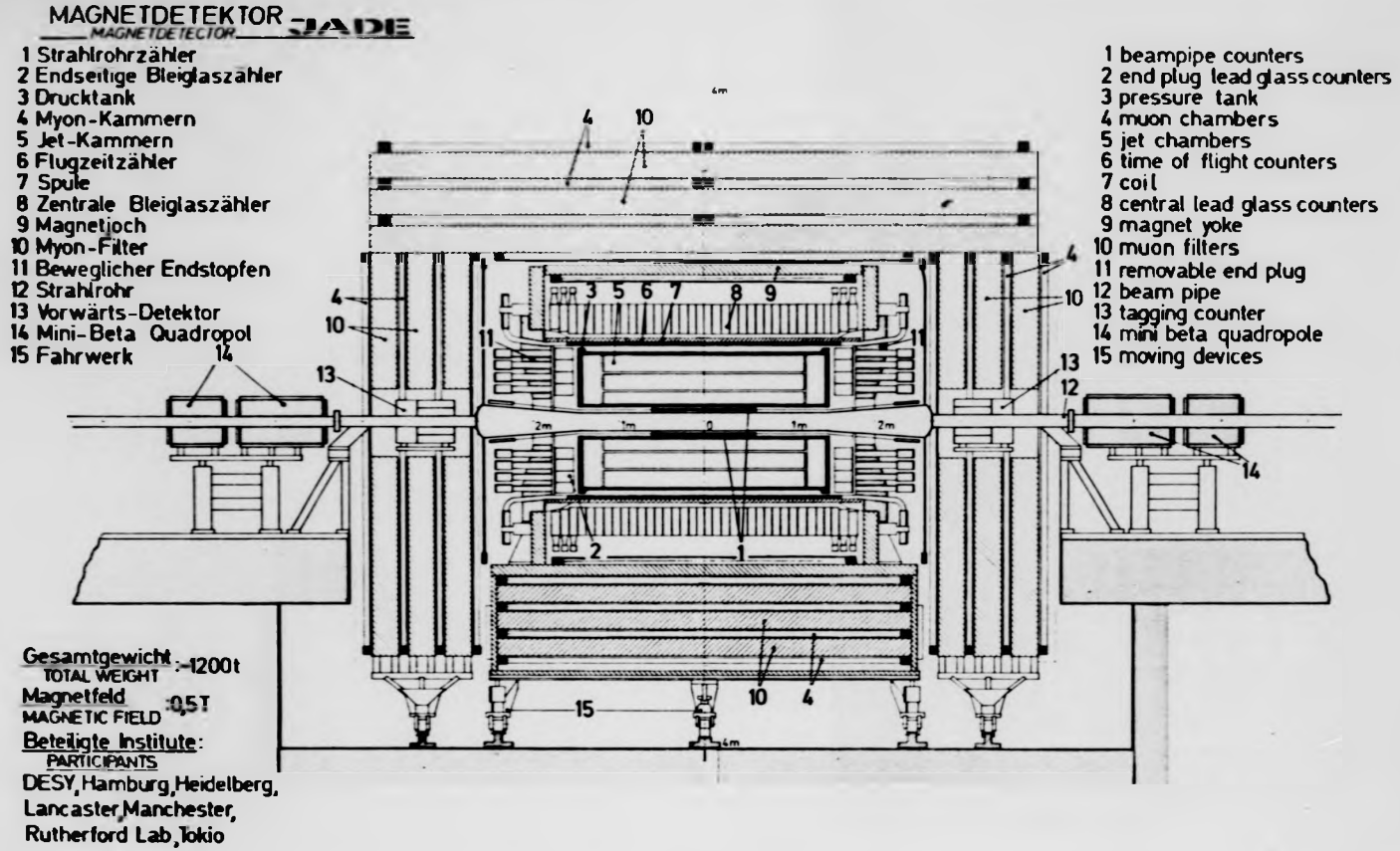

Figure 3.2. The JADE detector.

These components will now be described in more detail, the emphasis being on those which are of particular interest in the following analysis.

Henceforth a coordinate system will be used with origin at the interaction point within the JADE detector, z axis in the direction of the positron beam, y axis vertical and x axis pointing towards the centre of the PETRA ring. In addition, as illustrated in figure 3.3, the coordinates θ, the angle with respect to the z axis and ϕ, the angle in the $x\,y$ plane with respect to the x axis will be used.

The Beampipe Counters.

The beampipe was surrounded by an array of 24 scintillation counters of length $1.3\,m$. Each of these was read out at both ends through a light-guide and photomultiplier. These counters were used primarily to provide an indication of the beam conditions, thus enabling a decision to be made as to whether or not it was safe to switch on the more fragile detector components.

The Jet Chamber.

Physical principles.

A charged particle passing through a gas loses energy to it through electromagnetic interactions, exciting and ionizing the atoms and molecules of the gas. The particle leaves behind it a trail of ionized atoms and the electrons which have been removed from those atoms. The energy lost by the particle per unit of flight path, dE/dx, and hence the linear density of the ionization trail are dependent on the gas pressure, its composition, the particle's charge and its speed (Allison and Cobb, 1980). The dependence on the particles speed, which is one of the properties used to identify particles in the following, is illustrated in figure 3.4. For particles with a speed $\beta > 0.3$, in units of the speed of light, dE/dx decreases with increasing speed, proportional to β^{-2}. A minimum is reached at about $\beta = 0.97$ and thereafter dE/dx increases logarithmically with increasing $\gamma^2 = (1 - \beta^2)^{-1}$,

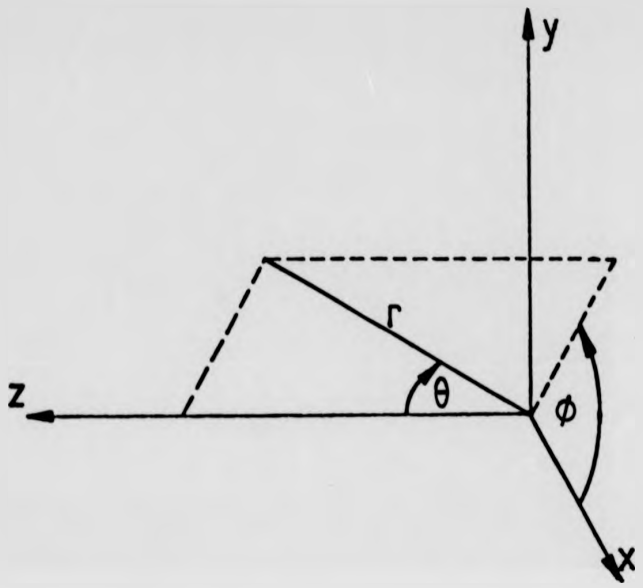

Figure 3.3. The JADE coordinate system.

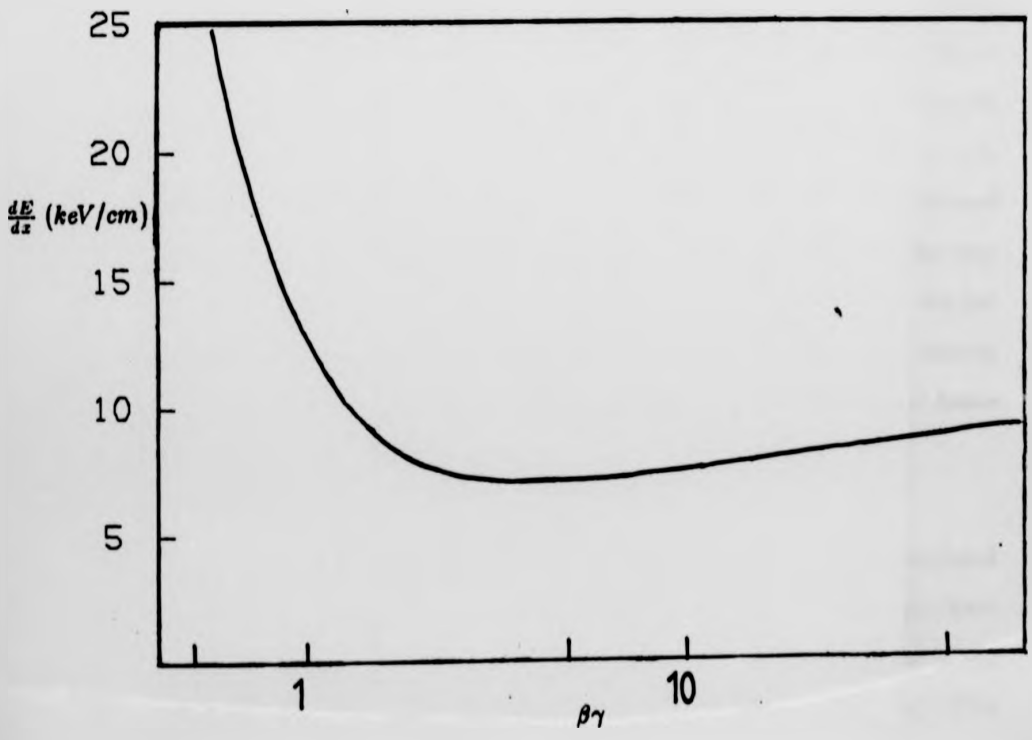

Figure 3.4. dE/dx as a function of $\beta\gamma$.

until it plateaus at a dE/dx of about $10.0\,keV/cm$.

In a proportional drift chamber, such as the Jet chamber, the ion-electron pairs produced by the passage of a fast particle are caused to drift by the application of an electric field across the gas. The velocity at which the electrons drift is typically $5\,cm/\mu sec$ along the field lines towards the anode while the ions move about a thousand times more slowly towards the cathode. The field is shaped so that it is roughly uniform apart from a region near the anode, within which it is much stronger. The electrons thus drift towards the anode with almost constant speed until they enter the region of high electric field strength. Here between inter-atomic collisions they may acquire enough energy to ionize the atoms with which they collide and thus a large number of electrons and ions are produced near the anode. If the field strength is correctly chosen, by using an anode wire of correct dimensions and applying the correct potentials, the number of electrons and ions produced near the anode is proportional to the number produced by the initial fast particle, hence the name proportional chamber. The charge cloud induces an electrical pulse on the anode, starting as the electrons reach the anode and tailing off as the positive ions drift away from it. This pulse travels to both ends of the anode wire. Measurement of the time after passage of the charged particle at which the pulse is generated, together with knowledge of the electron drift speed in the gas, enables determination of where along the drift path the fast particle passed the anode wire. Measurement of the charge of the pulse enables determination of the amount of ionization caused by the fast particle and hence its dE/dx.

A coordinate for the distance along the anode at which the pulse was generated may be found by comparing the arrival times of the pulses, or by comparing their charges, at either end of the wire. These latter are inversely proportional to the impedance between the point at which the pulse was induced and ground. This

until it plateaus at a dE/dx of about $10.0\,keV/cm$.

In a proportional drift chamber, such as the Jet chamber, the ion-electron pairs produced by the passage of a fast particle are caused to drift by the application of an electric field across the gas. The velocity at which the electrons drift is typically $5\,cm/\mu sec$ along the field lines towards the anode while the ions move about a thousand times more slowly towards the cathode. The field is shaped so that it is roughly uniform apart from a region near the anode, within which it is much stronger. The electrons thus drift towards the anode with almost constant speed until they enter the region of high electric field strength. Here between inter-atomic collisions they may acquire enough energy to ionize the atoms with which they collide and thus a large number of electrons and ions are produced near the anode. If the field strength is correctly chosen, by using an anode wire of correct dimensions and applying the correct potentials, the number of electrons and ions produced near the anode is proportional to the number produced by the initial fast particle, hence the name proportional chamber. The charge cloud induces an electrical pulse on the anode, starting as the electrons reach the anode and tailing off as the positive ions drift away from it. This pulse travels to both ends of the anode wire. Measurement of the time after passage of the charged particle at which the pulse is generated, together with knowledge of the electron drift speed in the gas, enables determination of where along the drift path the fast particle passed the anode wire. Measurement of the charge of the pulse enables determination of the amount of ionization caused by the fast particle and hence its dE/dx.

A coordinate for the distance along the anode at which the pulse was generated may be found by comparing the arrival times of the pulses, or by comparing their charges, at either end of the wire. These latter are inversely proportional to the impedance between the point at which the pulse was induced and ground. This

impedance consists of a component due to the wire length along which the pulse has travelled and a component due to the electronics used to measure the pulse charge. If the impedances of the electronics at each end of the wire are known or are the same as the same readout system is used at both ends of the wire, then the position along the wire at which the pulse was induced may be found. This method, known as charge division, was used in the Jet chamber. More detail concerning the theory, construction and operation of proportional chambers may be found in Sauli.

Construction and operation.

The chamber was built of three concentric rings of cells, each cell being a proportional drift chamber. The inner two rings contained 24 cells and the outer 48. The entire chamber was surrounded by an aluminium pressure vessel which enabled the gas filling, a mixture of argon, methane and isobutane, to be kept at a pressure of 4 atmospheres. This improved both the accuracy with which space points could be measured and the dE/dx resolution over that obtainable with a similar style of chamber at atmospheric pressure.

Each cell contained cathodes on the inner faces of its walls and 16 anode wires running axially along its length. A sector of the chamber, containing two first ring cells, two second ring cells and four outer ring cells, is shown in figure 3.5. The anode wires, of $20\mu m$ gold plated tungsten, were separated by further wires to enable fine control of the electric field in the critical multiplication region. Each of the anodes was read out at both ends through a pre-amplifier and an analogue to digital converter, capable of recording the arrival time and pulse height of up to eight pulses.

As the Jet chamber was operated in a magnetic field the electron drift direction was not that of the electric field lines, but at an angle to them. This angle, the Lorentz angle, was almost constant along the entire electron drift path, as the

impedance consists of a component due to the wire length along which the pulse has travelled and a component due to the electronics used to measure the pulse charge. If the impedances of the electronics at each end of the wire are known or are the same as the same readout system is used at both ends of the wire, then the position along the wire at which the pulse was induced may be found. This method, known as charge division, was used in the Jet chamber. More detail concerning the theory, construction and operation of proportional chambers may be found in Sauli.

Construction and operation.

The chamber was built of three concentric rings of cells, each cell being a proportional drift chamber. The inner two rings contained 24 cells and the outer 48. The entire chamber was surrounded by an aluminium pressure vessel which enabled the gas filling, a mixture of argon, methane and isobutane, to be kept at a pressure of 4 atmospheres. This improved both the accuracy with which space points could be measured and the dE/dx resolution over that obtainable with a similar style of chamber at atmospheric pressure.

Each cell contained cathodes on the inner faces of its walls and 16 anode wires running axially along its length. A sector of the chamber, containing two first ring cells, two second ring cells and four outer ring cells, is shown in figure 3.5. The anode wires, of $20\mu m$ gold plated tungsten, were separated by further wires to enable fine control of the electric field in the critical multiplication region. Each of the anodes was read out at both ends through a pre-amplifier and an analogue to digital converter, capable of recording the arrival time and pulse height of up to eight pulses.

As the Jet chamber was operated in a magnetic field the electron drift direction was not that of the electric field lines, but at an angle to them. This angle, the Lorentz angle, was almost constant along the entire electron drift path, as the

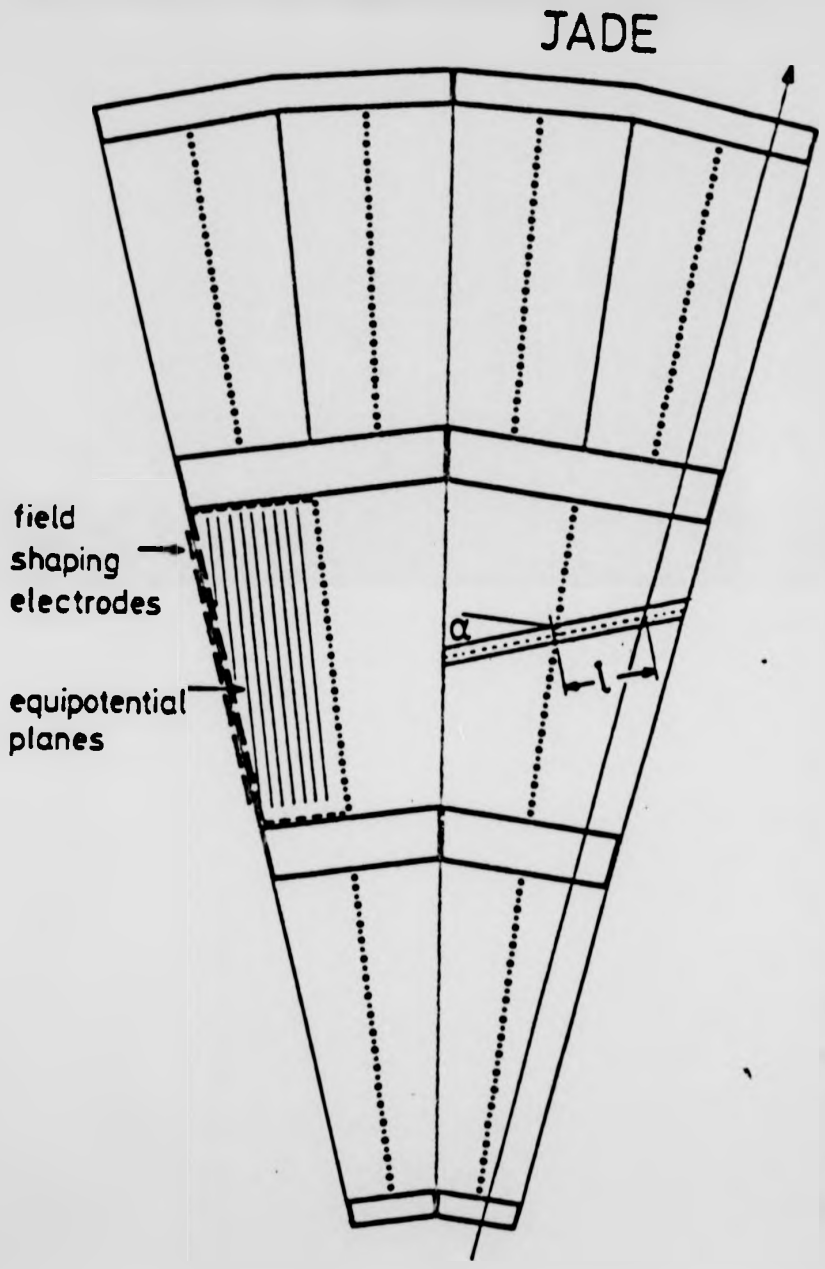

Figure 3.5. A sector of the Jet chamber, α is the Lorentz angle and l the drift length.

electron drift speed was practically constant, and was measured to be 18°30′ for the normal operational magnetic field of 0.487 T.

The measurements of the electronic drift time and the charge division for each of the 16 wires in a cell enabled determination of the track followed by a charged particle in passing through the chamber, up to deciding whether it had passed 'left' or 'right' of a plane of sense wires. To resolve this ambiguity the sense wires were displaced alternately 150 μm left and right of the central plane of the cell. Due to the electrostatic forces on the wires this displacement increased to a mean of 200μm when the high voltage was switched on. The effect of this asymmetry was that the fit quality obtained when a smooth trajectory was fitted through the hits due to a track was better for the correct left-right assignment than for the 'mirror' hits. For tracks which passed through all three rings of the Jet chamber a further means of resolving the left-right ambiguity was available. The juxtaposition of the cells in the third ring with those in the first two was such that only one choice of trajectory allowed a smooth curve to be fitted along the hits assigned to a track, the mirror tracks being discontinuous at the boundary between the second and third rings.

Due to the axial magnetic field the trajectories of charged particles in the Jet chamber were approximately helical, although deviations from helicity arose due to energy lost in traversing the gas and multiple Coulomb scattering in the gas or cell walls. The particle momentum transverse to the beam direction p_{xy} (in GeV/c) was calculated from the radius of curvature ρ (in m) of a helix fitted to the space points assigned to a track using

$$p_{xy} = 0.3qB\rho$$

where B was the magnetic field strength (in T), c the speed of light and q the particle's charge (in units of e), assumed to be ± 1, the sign being determined from

the direction of the track curvature. The magnitude of the total momentum was then calculated from

$$p = \frac{p_{xy}}{\sin\theta},$$

θ being the angle of the track direction with respect to the beam, or z axis.

For each sense wire a measurement of the ionization caused by a particle passing through its sensitive volume was obtained by combining the pulse charge measurements made at each end of the wire. To find the linear density of the ionization trail this figure was corrected for the length of the particle track in the anode's sensitive volume. This included a 10% correction due to the effect of the left-right sense wire staggering which slightly altered the shape of the electric field and hence the catchment volume left and right of the sense wire plane. Corrections were also made to the pulse height measurements from wires at the cell edges as for one side of the sense wire planes the catchment volume was reduced due to the Lorentz angle at which the electrons drift.

A study of the pulse charge results corrected for the above effects revealed a negative correlation between drift distance and pulse charge, probably due to the presence of a small amount of oxygen, which absorbs drifting electrons, in the Jet chamber gas (JADE 1979 and 1984a). Electronic cross-talk at a level of about 6% was observed between adjacent sense wires and also tracks passing very close to an anode were seen to give a spuriously large pulse. Corrections were applied for all these effects to obtain a figure for dE/dx for the track for each anode that it passed.

The individual dE/dx measurements along a given track were seen to approximately follow the expected Landau distribution, that is a Poisson distribution with a long positive tail. The tail holds little information as to the particle identity and makes the distribution awkward to work with. The following procedure was thus

adopted to produce a measure of the dE/dx for a track. The highest fifth of the dE/dx measurements were discarded and the remaining measurements, which were found to be approximately normally distributed, were used to calculate the mean dE/dx for the track and its standard error.

Some parameters and dimensions of the Jet chamber are given in table 3.1, more information concerning the construction and operation of the chamber is given in Heintze (1982).

The Time Of Flight Counters.

The Time Of Flight, or TOF, counters immediately surrounded the Jet chamber pressure vessel. They consisted of 42 plastic scintillation counters which were read out at both ends, using photomultipliers. They were used in the trigger, for low energy particle identification and for rejection of out of time tracks due to cosmic ray or other sources.

The Electromagnetic Calorimeter.

Physical Principles.

A second means by which charged particles lose energy in traversing matter is the emission of bremsstrahlung radiation in the Coulomb fields of the nuclei (figure 3.6). This emission is, classically speaking, the result of the acceleration of the charge in the electric field of the nucleus. Only for light particles, that is electrons and positrons, traversing sufficiently dense materials does bremsstrahlung radiation compose a significant proportion of the energy lost.

A closely related effect occurs when a photon interacts in a nuclear field to produce an electron positron pair (figure 3.7).

The combination of the processes of bremsstrahlung and pair production leads to the development of electromagnetic cascades, or showers, when high energy elec-

Table 3.1, Jet Chamber Parameters.

Length	$2.4\,m$
Inner radius	$0.2\,m$
Outer radius	$0.8\,m$
Maximum drift distance	$0.075\,m$
Drift field	$94\,kV/m$
Gas mixture, Ar:CH_4:(iso)C_4H_{10}	0.887:0.085:0.028
Gas pressure	$4\,atm$
Drift measurement resolution	$160\,\mu m$
Longitudinal measurement resolution	$16\,mm$
Double track resolution	$7\,mm$
Resolution of p_{xy} measurement	$\frac{\Delta p_{xy}}{p_{xy}} = 0.014 p_{xy}$ (p_{xy} in GeV/c)
Inner detector material for normally incident particles	$0.037\,r.l.$
Acceptance, max. no. of hits	$\lvert\cos\theta\rvert < 0.83$
Acceptance, more than 8 hits	$\lvert\cos\theta\rvert < 0.97$
dE/dx resolution, >36 hits, $\lvert\cos\theta\rvert < 0.75$	
(a) Bhabha tracks	0.065
(b) Pion tracks in multihadronic events with momenta in range $0.45 < p_\pi < 0.6\,GeV/c$	0.080

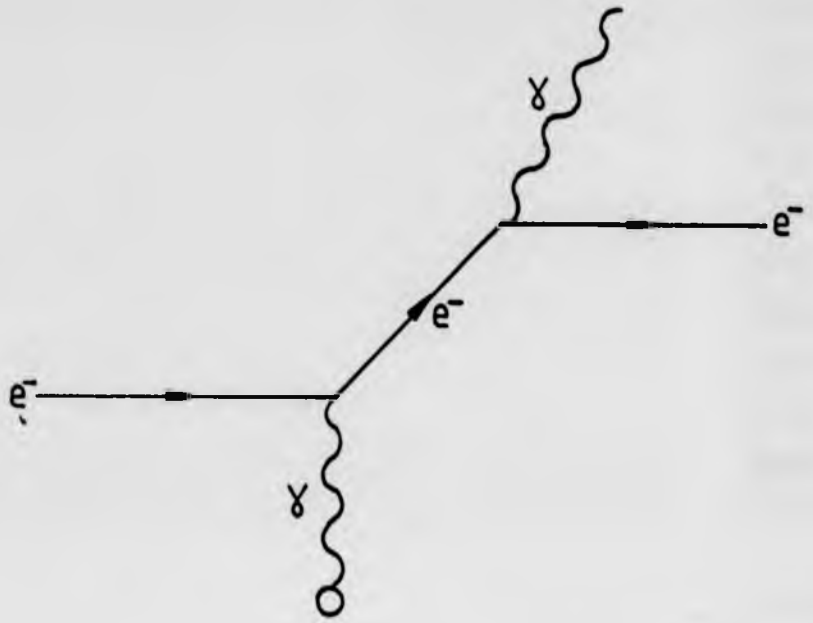

Figure 3.6. Bremsstrahlung emission of a photon in the electromagnetic field of a nucleus.

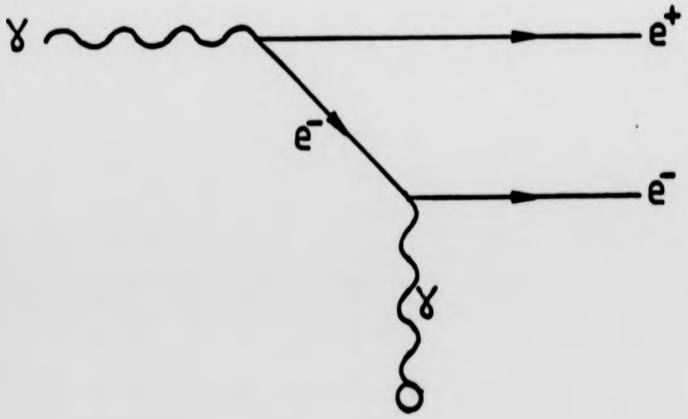

Figure 3.7. Pair production in the electromagnetic field of a nucleus.

trons, positrons or photons enter a dense material. For a high energy electron this occurs as follows. The electron emits a bremsstrahlung photon and this photon then pair produces. The electrons and positron emit further bremsstrahlung photons which also pair produce and so on until the energy of the resulting photons is below the threshold for pair production, that is less than twice the electron mass, or the loss of energy of the positrons and electrons through the processes of ionization and excitation becomes dominant over the energy loss through bremsstrahlung radiation. Showers are produced in a similar manner by high energy positrons and photons. For the latter the first step is pair production, not bremsstrahlung. This process lends itself to Monte-Carlo simulation and may be accurately modelled (Ford, 1978).

The electrons and positrons in electromagnetic cascades travel with a speed greater than that of light in the dense material in which they are produced and thus emit Čerenkov radiation. They also cause excitation and ionization of the atoms of the material and as these atoms relax photons are emitted. Both these processes result in a detectable light output, the quantity of light being proportional to the incident electron, positron or photon energy. For the material from which the JADE electromagnetic calorimeter was constructed the former of these mechanisms for light production is the most important.

Construction and Operation.

The electromagnetic calorimeter was built in three parts: a barrel section outside the magnet coil and inside the iron return yoke; and two end cap sections. Schott SF5 lead-glass was used throughout, a glass in which approximately 55% of the silicon dioxide has been replaced by lead oxide, thus increasing its density without spoiling its transparency.

The barrel was constructed of 30 rings of 84 lead-glass blocks, each block tapering from $8.5 \times 10.2\,cm^2$ at its inner surface to $10.2 \times 10.2\,cm^2$ at its outer

surface, over a length of 30 cm. This length represents 12 radiation lengths. The blocks were optically isolated from one another and each was read out through a 6 cm light guide using a photomultiplier.

The endcaps were each built of 96 blocks of lead-glass. The blocks were $14 \times 14 \times 22.3\,cm^3$ in dimension, that is about 9.3 radiation lengths long, and were read out in the same manner as the barrel blocks although the light guides had to pass through the iron return yoke and were thus 51 cm long.

Prior to installation all the blocks and their photomultipliers were calibrated using a positron test beam. In addition an optical fibre was connected to each photomultiplier enabling them to be illuminated with light from a xenon flash tube. Hence calibration of any drift in photomultiplier gain was possible. Dimensions and parameters of the electromagnetic calorimeter are listed in table 3.2.

The Muon System.

This section of the detector was designed to enable identification of muons. These pass through the electromagnetic calorimeter without losing a lot of energy as they are too massive to emit much bremsstrahlung radiation, but then so are pions, kaons and protons. These latter however all undergo hadronic interactions with the nuclei in material while muons do not as they contain no colour charged components. Thus muons tend to penetrate further in matter.

To exploit this fact the muon system was built of a series of blocks of absorber inter-leaved with planar proportional drift chambers. These enabled the penetration of particles through the absorber to be observed and tracks which were particularly likely to be muons to be picked out. For more detail concerning the construction of this section of the detector see Allison (1985a).

Table 3.2, Electromagnetic Calorimeter Parameters.

Barrel acceptance	$\lvert\cos\theta\rvert < 0.82$
Highest quality shower measurement	$\lvert\cos\theta\rvert < 0.75$
Barrel energy resolution	$E < 6\,GeV$, $\frac{\Delta E}{E} = \frac{0.06}{\sqrt{E}}$
	$E > 6\,GeV$, $\frac{\Delta E}{E} = 0.038$
	(E in GeV)
Barrel angular resolution	$\Delta\theta \approx 0.6°$, $\Delta\phi \approx 0.7°$
End cap acceptance	$0.89 < \lvert\cos\theta\rvert < 0.97$
End cap energy resolution	$\frac{\Delta E}{E} = 0.1$
	(E in GeV)
End cap angular resolution	$\Delta\theta \approx 0.7°$, $\Delta\phi \approx 1.1°$

The Forward Muon Counters.

These were 4 arrays of 20 large scintillation counters placed outside the ends of the iron return yoke on either side of the beampipe and used to aid triggering on muon pair events in which the polar angle at which the muons were produced was small.

The Tagging System.

These detectors, which have undergone several design changes and which have been placed in two positions along the beampipe, were used to detect small angle Bhabha events in order to monitor the luminosity and also for two photon physics.

Chapter 4

Data Taking, Analysis, Multihadronic Event Selection and the JADE Monte-Carlo

Running the JADE Detector.

The control, monitoring and readout of the JADE detector during data taking were performed automatically by the JADE Data Acquisition System, JDAS. This was composed of a trigger unit and a computer system with its attendant software.

Typically, after completion of a PETRA filling and acceleration of the electron and positron beams to the required energy, provided the beampipe counters indicated that the beam conditions were suitably stable, the high voltage supplies of the electromagnetic calorimeter and the Jet chamber were switched on. These could not be left on during filling as the occasional losses of large numbers of particles which occur during this process could then have damaged them. A data taking run was then started and control of the experiment passed to JDAS. During the run JDAS continually monitored various critical power supplies and produced and checked histograms related to the performance of the various detector components. Its most important function however was to select potentially interesting events, to collate through a CAMAC system all the information recorded by the detector concerning those events, to perform various quick tests to check if the events deserved further study and if so to transfer the data to a storage medium.

Selection of a small group of events for full readout and storage was necessary as the great majority of signals which occur in the detector are not due to electron positron annihilations, but result from background sources such as cosmic rays, electron or positron interactions with residual beam gas atoms or with the beampipe, synchrotron radiation or just electronic noise. Readout of the complete detector takes about $30\,msec$, during which time the detector is insensitive

to further events. Beam crossings, and potentially electron positron annihilation events, occur every $3.8\,\mu sec$. Thus simply storing all signals recorded by the detector, even if coincidence with a beam crossing was required, would mean the loss of a large proportion of the events of interest and would require the use of an enormous amount of storage space.

The first stage in the event selection process was performed by the trigger, which was designed to use the information from the various detector components as it became available to decide whether to read the event out or not. If yes then JDAS collected and stored all the event data, otherwise all the detector components were placed in a state of readiness for the next beam crossing and potential annihilation event.

The Trigger.

The trigger process was started by the arrival of an electronic pulse from PETRA control, if this was followed by a signal from a capacitive pick-up at $z = -6.67\,m$, indicating the passage of a positron bunch, then a logical flag $T0$ was set. This indicated that the trigger system had started a cycle and further $T0$'s were not accepted until the cycle was completed. Timing signals were also issued to the electronic readout sytems of the various detector elements.

After the bunch crossing, signals started to arrive from the detector, firstly from the photo-tubes of the scintillators and the lead-glass system. The first trigger decision, $T1$, was then made. Three responses were possible, if the information was such that the event was definitely worthy of further study then an 'accept' was issued, if the event was definitely of no interest then a 'reject' was issued and if further information was required to enable the decision to be made a 'postpone' was issued. A reject resulted in the immediate issue of a reset to all the detector components, completing a trigger cycle and preparing the detector for the next beam crossing. An accept was followed by full readout of the detector. The

conditions leading to the decisions accept, postpone and reject are given in table 4.1. The $T1$ decision was reached approximately $0.7\,\mu sec$ after $T0$.

The next batch of information to become available to the trigger was that from the Jet chamber and was used to make the $T2$ decision. A hard-wired logic unit was used to check if the pattern of wires registering a hit could correspond to a track or tracks. Again an accept, a reject or a postpone was issued depending on the results of this check, see table 4.1 for the required conditions. The $T2$ decision was reached after about $2\,\mu sec$. A reject at either the $T2$ or the $T1$ level enabled resetting of the detector in time for the next beam crossing.

If a $T2$ postpone was issued then the final trigger step, $T3$, was considered. Information from the muon system was used to decide if the event contained penetrating particles, if so it was accepted if not rejected. Due to the long maximum electron drift time in the muon chambers, this information was not available until $4.5\,\mu sec$ after $T0$, thus waiting for $T3$ entailed the loss of at least one beam crossing. $T3$ was originally designed as a means of triggering on muon pair events, but the necessity of waiting so long for the information to arrive made it desirable to find some other way of triggering on such events. In 1982 this was accomplished by modifying the $T2$ trigger to accept muon pair events. The $T3$ level of the trigger process was then only needed to search for indications of penetrating tracks after a postpone at $T1$ due to signals from opposite forward muon counters.

Readout and Online Event Selection.

The individual JADE detector elements were interfaced to the JADE online computer, a NORD 10S/NORD 50 dual processor, through a multi-branch CAMAC system. If an event was accepted by the trigger unit then all the event data were transferred via the CAMAC system into a section of the memory of the NORD 10S. If the event was triggered at the $T2$ level, that is on the evidence that it contained tracks, the data were simultaneously transferred to a Plessey

Table 4.1, Trigger Conditions.

(a) T1.

Condition:-	Response:-
Total lead glass energy $> 4\,GeV$.	Accept event.
Signals in both tagging counters.	Accept event.
A signal in one tagging counter and at least $2\,GeV$ in the leadglass.	Accept event.
At least one TOF counter signal and two $> 1\,GeV$ lead glass clusters.	Postpone 1.
A signal from one tagging counter.	Postpone 2.
Signals from two approx. opposite TOF counters and hits in not more than 4 TOF counters.	Postpone 3.
Signals from opposite forward muon counters.	Postpone 4.

(b) T2.

Following:-	Accept event if:-
Postpone 1.	One or more inner detector tracks.
Postpone 2.	One or more inner detector tracks.
Postpone 3.	At least two tracks with $p_{xy} > 0.5\,GeV/c$.

(c) T3.

Following:-	Accept event if:-
Postpone 4.	At least one potential muon track.

MIPROC 16 microprocessor, which performed a more sophisticated track search than that used in the trigger, making use of the drift time information. As soon as the data transfer was completed, the CAMAC system was cleared and a reset issued, the detector was then ready to accept the next event.

If the MIPROC found no evidence of tracks in events triggered at the $T2$ level these were now rejected and purged from the NORD 10S memory. Otherwise the data were moved to a second section of memory, or buffer, in which they were accessible to the NORD 50. The NORD 50 performed some analysis of those events; histograms of various quantities important to the running of the detector were filled, these were checked for evidence that the detector was malfunctioning, a fast pattern recognition procedure was used to study tracks in the Jet chamber data and the events were categorized.

The results of the fast pattern recognition were used to calculate the position of the event z-vertex. If the quality of the vertex found was good, and outside the limits possible for a genuine annihilation event ($|z| < 30\,cm$ was required) then the event was not passed on for storage.

The categorization algorithms were capable of recognising event classes such as muon pair events, Bhabha events, multihadronic events, cosmic ray events and beam gas events. If the event was unambiguously found to belong to one of the latter two background types, then it was rejected, unless it was one of the 5% of 'rejected' events selected for storage to enable later checking of the classification algorithms. Rejection of events at this stage saved a considerable amount of space on storage media and also a lot of valuable off-line computing time. Another advantage was that the online system was able to produce 'instant' results for various quantities of interest, such as the luminosity and the ratio of the multihadronic to muon pair cross-sections R.

MIPROC 16 microprocessor, which performed a more sophisticated track search than that used in the trigger, making use of the drift time information. As soon as the data transfer was completed, the CAMAC system was cleared and a reset issued, the detector was then ready to accept the next event.

If the MIPROC found no evidence of tracks in events triggered at the $T2$ level these were now rejected and purged from the NORD 10S memory. Otherwise the data were moved to a second section of memory, or buffer, in which they were accessible to the NORD 50. The NORD 50 performed some analysis of those events; histograms of various quantities important to the running of the detector were filled, these were checked for evidence that the detector was malfunctioning, a fast pattern recognition procedure was used to study tracks in the Jet chamber data and the events were categorized.

The results of the fast pattern recognition were used to calculate the position of the event z-vertex. If the quality of the vertex found was good, and outside the limits possible for a genuine annihilation event ($|z| < 30\,cm$ was required) then the event was not passed on for storage.

The categorization algorithms were capable of recognising event classes such as muon pair events, Bhabha events, multihadronic events, cosmic ray events and beam gas events. If the event was unambiguously found to belong to one of the latter two background types, then it was rejected, unless it was one of the 5% of 'rejected' events selected for storage to enable later checking of the classification algorithms. Rejection of events at this stage saved a considerable amount of space on storage media and also a lot of valuable off-line computing time. Another advantage was that the online system was able to produce 'instant' results for various quantities of interest, such as the luminosity and the ratio of the multihadronic to muon pair cross-sections R.

Further detail concerning the online analysis may be found in Mills (1985).

Events which survived all the selection processes, or had been chosen for off-line test of those processes, were then copied into a further buffer from which they could be graphically displayed, allowing the operators of the experiment to make a visual check of the detector performance. The same graphics display could be used to view the histograms collected by the NORD 50.

From this last buffer the data were copied either via a link to disc in the DESY computer centre and from there to magnetic tape, or, if the link was malfunctioning, directly to tape in the JADE control room.

JDAS is described in more detail in Cords (1985).

The data format used was the BOS system (Blobel, 1979) in which data are stored in large arrays or banks. These may be easily created, extended and deleted, thus making the system suitable for the storage of raw data and later adding the information obtained by processing that data as is convenient in high energy physics.

Data Analysis.

Despite the best efforts of the trigger and event filtering processes that were performed online, most of the events recorded by JADE in the period 1979 to 1982 were from various background sources. As full analysis of all these events would have required prohibitive amounts of computer time, further simple tests were made to eliminate some of the more obvious background events. These are listed in table 4.2.

For the approximately 13% of events that remained after these cuts a full analysis was performed. This included a detailed search for tracks in the Jet chamber. These were fitted to a parabola in xy space and a straight line in rz.

Table 4.2, Preliminary Event Selection.

Events were rejected if either of the following conditions was satisfied:-

(a) Total lead glass energy $< 7\,GeV$ with $< 3.5\,GeV$ in the barrel, no tag signal or Jet chamber hits.

(b) Total lead glass energy $> 6\,GeV$, 95% of which was in one endcap.

A fast search for inner detector tracks was performed for the events which survived these cuts and those in which no event vertex was found or in which the vertex was more than $35\,cm$ from the origin in z were rejected. The remaining events were accepted if they satisfied any of the following conditions:-

(a) There were signals from one or both of the tagging counters and the event contained at least one track of momentum $> 0.2\,GeV/c$ with 20 or more hits in the xy plane and originating from within $30\,cm$ of the origin in z.

(b) There was no signal from the tagging system and the event contained at least one track with momentum $> 0.6\,GeV/c$, 12 hits in the rz plane and origin within a cylinder along the beam axis, centred on the interaction point, with radius $6\,cm$ and length $60\,cm$.

(c) There was no signal from the tagging system and no track with 12 or more hits in the rz plane, but at least one track with 20 or more hits in the xy plane.

Clusters of neighbouring lead-glass blocks in which energy had been deposited were also searched for, and the position at which a single particle must have entered the electromagnetic calorimeter to form that pattern of energy deposition was calculated. The particle tracks in the Jet chamber in the locality of the shower were extrapolated to check if the particle concerned could have given rise to the shower. If no tracks fitted this hypothesis the shower was assumed to be due to a photon. The cluster energy was calculated and corrected for the angle of incidence of the track which caused its formation, assuming this to have come from the origin if it was a photon. Clusters in which energy may have leaked into an insensitive region of the calorimeter were marked as having an unreliable energy.

Finally the Jet chamber tracks were extrapolated through the lead-glass system, magnet yoke and muon filter, allowance being made for the effects of multiple coulomb scattering. The muon chambers were then searched for hits in a region compatible with their resolution and the effects of multiple scattering of the track, to study the penetration distance of the track through the hadron absorber. Penetrating tracks were flagged as muon candidates. More details concerning this last step are given in Allison (1985b).

At this stage of the analysis Monte-Carlo simulations, to be described in the last section of this chapter, suggested that about 55% of the events were the result of electron-positron annihilations.

Multihadronic Event Selection.

As a first step in finding multihadronic events, multi-particle events of all types were selected by requiring:

(a) at least 4 charged tracks in each event;

(b) a lead-glass energy of $E_{\text{barrel}} > 3\,GeV$ or $E_{\text{endcaps}} > 0.4\,GeV$;

Clusters of neighbouring lead-glass blocks in which energy had been deposited were also searched for, and the position at which a single particle must have entered the electromagnetic calorimeter to form that pattern of energy deposition was calculated. The particle tracks in the Jet chamber in the locality of the shower were extrapolated to check if the particle concerned could have given rise to the shower. If no tracks fitted this hypothesis the shower was assumed to be due to a photon. The cluster energy was calculated and corrected for the angle of incidence of the track which caused its formation, assuming this to have come from the origin if it was a photon. Clusters in which energy may have leaked into an insensitive region of the calorimeter were marked as having an unreliable energy.

Finally the Jet chamber tracks were extrapolated through the lead-glass system, magnet yoke and muon filter, allowance being made for the effects of multiple coulomb scattering. The muon chambers were then searched for hits in a region compatible with their resolution and the effects of multiple scattering of the track, to study the penetration distance of the track through the hadron absorber. Penetrating tracks were flagged as muon candidates. More details concerning this last step are given in Allison (1985b).

At this stage of the analysis Monte-Carlo simulations, to be described in the last section of this chapter, suggested that about 55% of the events were the result of electron-positron annihilations.

Multihadronic Event Selection.

As a first step in finding multihadronic events, multi-particle events of all types were selected by requiring:

(a) at least 4 charged tracks in each event;

(b) a lead-glass energy of $E_{\text{barrel}} > 3\,GeV$ or $E_{\text{endcaps}} > 0.4\,GeV$;

(c) one track or more with at least 20 recorded hits and origin such that $|z| < 40\,cm$;

(d) at least 2 tracks with more than 24 hits and with origin such that the distance to the interaction point in the xy plane, $|r_{\min}| < 3\,cm$.

Bhabha events in which some background source, typically beampipe interactions, had contributed a few extra tracks were then removed by requiring that, for the events with only two tracks with more than 24 hits, the angle between the plane defined by one of the tracks and the beam axis and that defined by the other track and the beam axis, be at least 10°. Some τ pair events were removed by eliminating events with a three tracks opposite to one track topology.

Only about 0.5% of the events survived all these cuts, but the loss of multihadronic events was negligible. Of the events selected approximately 50% were multihadronic, the rest being primarily two photon and beam gas events, though some τ pair contamination remained.

The events selected as above were then re-analysed. The tracks were refitted to helices and also to parabolae constraining the tracks to the event vertex. The energy loss per unit length of charged tracks was calculated. A search was performed for vertices in the Jet chamber, arising from particles that decayed in flight or converting photons. Other quantities useful in physics analyses were also calculated, for example sphericity, the idea being that computer time could be saved by calculating such results once and having them available with the event data. For further information on this standard analysis package see JADE (1984b).

The last stage in the multihadronic event selection was to remove the beam gas and two photon events by requiring that

$$E_{\rm vis} > E_{\rm beam}$$

and

$$p_{\mathrm{bal}} < 0.4$$

where

$$E_{\mathrm{vis}} = \sum_{i=1}^{N_c} p_i + \sum_{j=1}^{N_n} E_j$$

and

$$p_{\mathrm{bal}} = \frac{\sum_{i=1}^{N_c} p_i \cos\theta_i + \sum_{j=1}^{N_n} E_j \cos\theta_j}{E_{\mathrm{vis}}}$$

p_i being the absolute momentum of the i^{th} observed charged particle, θ_i its polar angle and N_c the total number of charged particles observed. E_j, θ_j and N_n are the corresponding figures for neutral clusters.

As the centre of mass of both two photon events and beam gas events was generally not stationary in the laboratory reference frame, and in both event classes energy was generally lost down the beam pipe, these cuts removed such events. Multihadronic events were only lost if a lot of energy had escaped down the beampipe due to bremsstrahlung emission of a high energy photon from the initial electron or positron, an unlikely occurrence. All the events which survived thus far were scanned, enabling removal, primarily, of some of the remaining τ pairs.

After the complete selection procedure outlined above Monte-Carlo simulation indicated that 96% of the events were multihadronic. The remaining background was composed primarily of τ pair events ($2.4 \pm 1.5\%$) and two photon events ($1.2 \pm 0.7\%$).

The JADE Monte-Carlo.

In order to determine the properties of e^+e^- annihilation events it is necessary to find out what influence the measurement process, that is the detector and the accompanying analysis procedures, has on the quantities of interest; namely the

types, energies, momenta and number of particles produced. This is achieved by using a computer model to simulate the interactions thought to occur in electron positron annihilation and also the detection process. The latter is well understood and can thus be accurately modelled. Comparing the results of the simulation of an interaction and the detection process with those obtained from the real data then enables the underlying physics to be studied and the simulation of the interactions involved to be refined. The simulation techniques use (pseudo) random number generators to model the probabalistic nature of the interactions and the detection processes which occur in quantum physics. These are known as Monte-Carlo techniques, and the suite of programs written to perform the modelling have acquired the name the 'JADE Monte-Carlo'. The JADE Monte-Carlo has undergone five years of continuous development and the simulation of the detector is now sophisticated and in general accurate, as may be determined by comparison of Monte-Carlo and real data concerning processes in which the underlying physics is well understood. For example Bhabha scattering provides a source of electrons whose energy distribution is well known. The energy deposited by these electrons in the lead-glass system may thus be compared with the expectations of the Monte-Carlo.

The Monte-Carlo has a further purpose. If a procedure is required for identifying a particular type of particle or event, this may be developed and its effectiveness determined by studying the particular properties of that type of particle or event as simulated by the Monte-Carlo. Identification of such particles or events in the real data enables testing of new areas of physics.

The JADE Monte-Carlo may be considered as consisting of three stages. In the first the initial configuration of particles in an electron positron annihilation event is simulated. In the second these particles are tracked through the detector, simulating particle decays and interactions with the detector including production

of signals in the detector components, but assuming perfect resolution and detection efficiency. In the last stage the effects of the real resolutions and efficiencies of the detector components are added. Further discussion will be limited to the modelling of multihadronic events.

The first stage of the Monte-Carlo for multihadronic event simulation was performed using a program based on the Lund model, version 5.2. The program simulates electron positron annihilation to hadrons including initial state radiation effects to order α^3, and perturbative QCD effects to order α_S^2, using $\alpha_S = 0.16$ at $35\,GeV$. Threshold effects due to the quark masses are simulated. A significant result of this is that the probability of production of b quarks decreases from the 9.1% expected from the ratio of the quark charges squared, to 8.2%.

As has been stated in chapter one the hadronization process, whereby the produced quarks anti-quarks and gluons convert to the hadrons that are seen, cannot be calculated from QCD. There are several alternative means of simulating hadronization, but that of the Lund group gives particularly good agreement with data (Bartel, 1983d). The ideas upon which this model is based were discussed in the chapter on electron positron annihilation. The Lund symmetric fragmentation function was used to produce the longitudinal momentum distribution for d, u and s quarks, with $a = 1.0$ and $b = 0.6$ (Bethke, 1984) and that of Peterson with $\epsilon_c = 0.05$ and $\epsilon_b = 0.018$ for the c and b quarks respectively, these latter being the values measured by the DELCO group (Atwood, 1983).

The decays of short-lived particles, D and B mesons for example, were also simulated at this stage and the products added to the set of initial particles.

The second stage of the Monte-Carlo consisted of simulating the passage of each of the initial particles through the JADE detector, referred to as 'tracking'. The effects of multiple Coulomb scattering and energy loss due to passage through

the material of the detector, photon conversions and particle decays were all taken into account. Decays were simulated according to the results tabulated by the Particle Data Group (1984), the decay products also being tracked through the detector.

As the particles were followed through the Jet chamber, the signals caused in the detector, excluding dE/dx information, were simulated, perfect efficiency and resolution being assumed. For particles which reached the lead glass electromagnetic shower development and the resulting signals were simulated, accurately for electrons and photons and somewhat less accurately for other particles to save computer time. Particles which passed through the electromagnetic calorimeter were tracked through the muon system.

In the third stage of the Monte-Carlo, the effects of the central drift chamber drift chamber resolution and efficiency were simulated as were the effects of the trigger. The Monte-Carlo data were then analysed in exactly the same manner as the real data.

The history of all the particles was recorded; their parents, genuine momentum and energy and how, if at all, they decayed.

That the Monte-Carlo accurately simulates the real data may be checked by comparing the distributions of various quantities in both data sets. As an example the Monte-Carlo and real data spectra of the momentum transverse to the event axis in multihadronic events, for tracks with momenta greater than $1\,GeV/c$, are shown in figure 4.1.

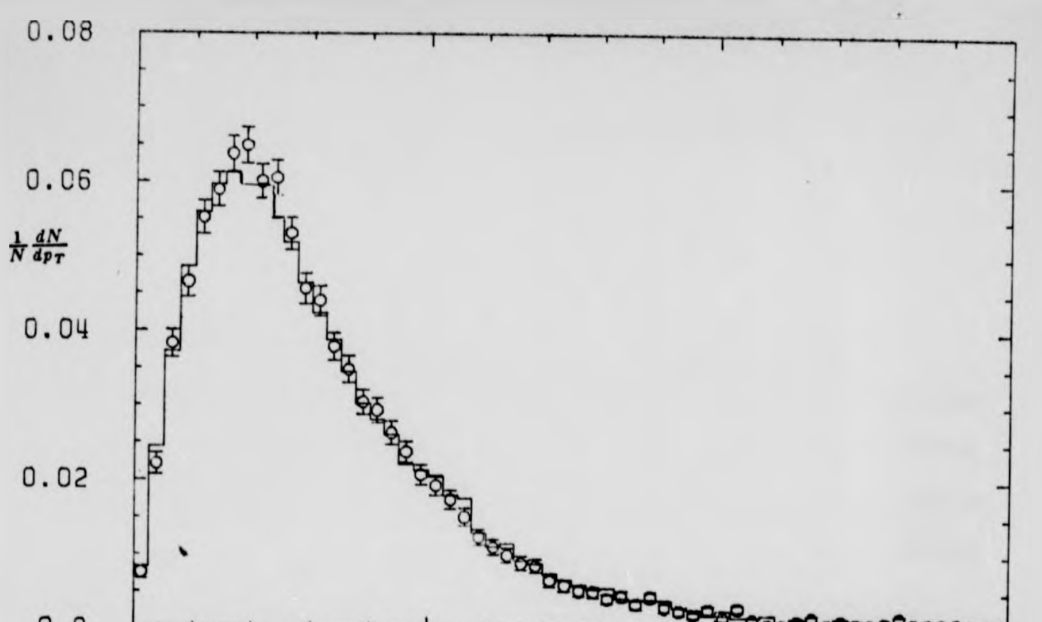

Figure 4.1. Monte-Carlo (solid line) and real data (circles) p_T spectra for all charged tracks with momenta greater than $1 GeV/c$.

Part II

Measurement of the c and b Quark Asymmetries

Introduction.

The measurement of the c and b quark asymmetries necessitates the separation of c and b quark events from the mix of events produced in electron positron annihilation, the determination of the quark directions in those events and an analysis of the distribution of the directions to determine the size of any asymmetry present.

One means of identifying heavy quarks, on a statistical basis, is to study kinematic quantities dependent on their mass. The energy released in their weak decay leading to properties which distinguish them from light quark events.

The quark, as opposed to the antiquark, direction may be identified as follows. Consider the events schematically represented in figures 5.1 and 5.2. These contain a prompt lepton, that is a lepton which results from the weak decay of a heavy quark. As the heavy c and b quarks are almost never produced in the fragmentation process this must be one of the initially produced quarks. Such multihadronic events, containing one or more leptons, are termed inclusive lepton events. The sign of the lepton's charge is the same as that of the quark from the decay of which it results. The charge of the lepton thus indicates, or tags, the quark charge. Therefore, for jets containing prompt leptons, it may be determined whether the jet had as parent the quark or anti-quark; provided the event flavour is known. (The complications arising in the case that a b quark decays via the cascade $b \rightarrow c \rightarrow l$ are discussed in what follows.)

The outline of a scheme whereby the c and b asymmetries can be measured using inclusive lepton c and b events is now apparent. For each event the quark

Part II

Measurement of the c and b Quark Asymmetries

Introduction.

The measurement of the c and b quark asymmetries necessitates the separation of c and b quark events from the mix of events produced in electron positron annihilation, the determination of the quark directions in those events and an analysis of the distribution of the directions to determine the size of any asymmetry present.

One means of identifying heavy quarks, on a statistical basis, is to study kinematic quantities dependent on their mass. The energy released in their weak decay leading to properties which distinguish them from light quark events.

The quark, as opposed to the antiquark, direction may be identified as follows. Consider the events schematically represented in figures 5.1 and 5.2. These contain a prompt lepton, that is a lepton which results from the weak decay of a heavy quark. As the heavy c and b quarks are almost never produced in the fragmentation process this must be one of the initially produced quarks. Such multihadronic events, containing one or more leptons, are termed inclusive lepton events. The sign of the lepton's charge is the same as that of the quark from the decay of which it results. The charge of the lepton thus indicates, or tags, the quark charge. Therefore, for jets containing prompt leptons, it may be determined whether the jet had as parent the quark or anti-quark; provided the event flavour is known. (The complications arising in the case that a b quark decays via the cascade $b \rightarrow c \rightarrow l$ are discussed in what follows.)

The outline of a scheme whereby the c and b asymmetries can be measured using inclusive lepton c and b events is now apparent. For each event the quark

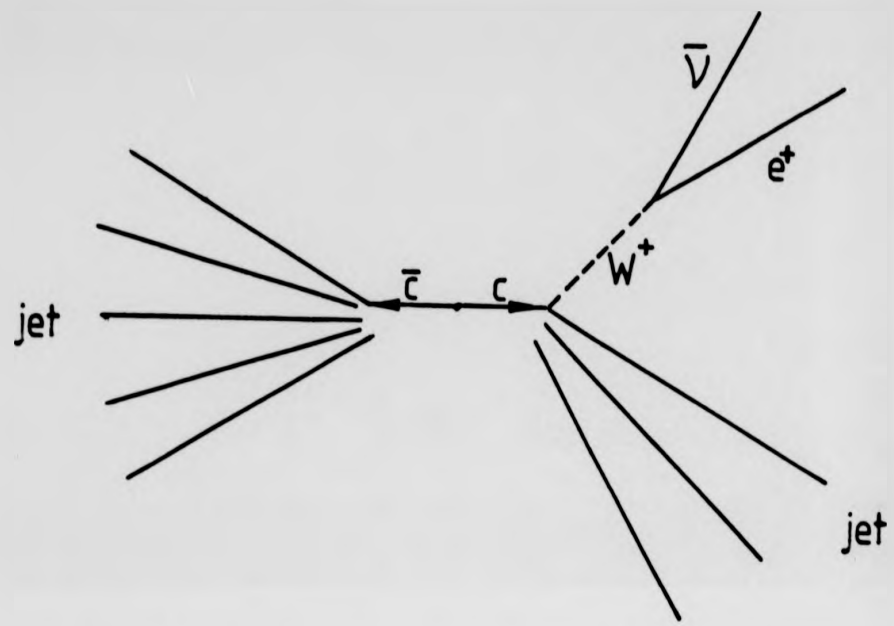

Figure 5.1. A schematic picture of an electron inclusive $c\bar{c}$ event.

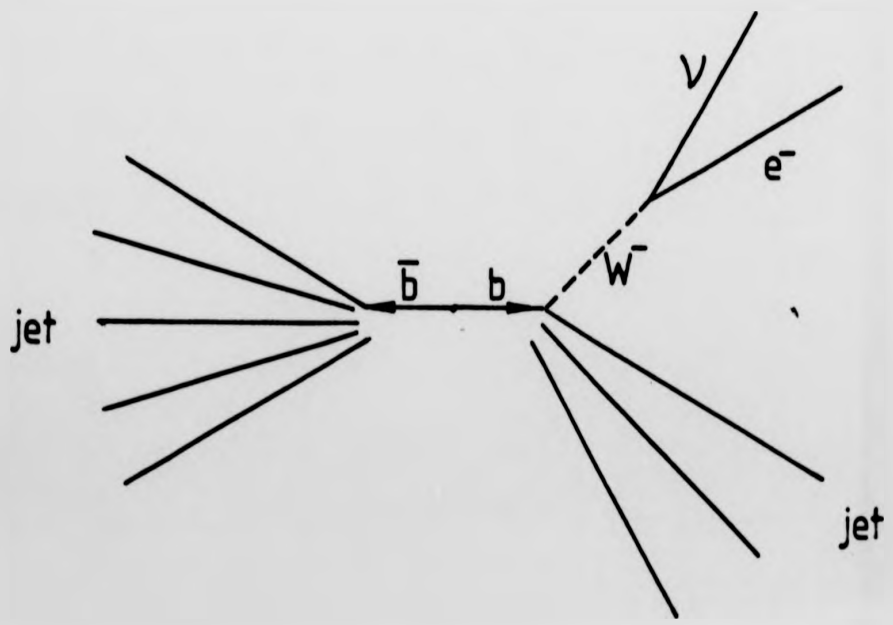

Figure 5.2. A schematic picture of an electron inclusive $b\bar{b}$ event.

anti-quark production axis is found by determining the event axis. This direction is given a sense according to the sign of the prompt lepton and the direction of the jet in which it appears. Hence a series of measurements of the angle θ between the outgoing quark's direction and that of the initial state electron are made. From the distribution of these angles the required asymmetries are determined.

This scheme has been used with great success to measure the b asymmetry from a sample of inclusive muon events (Bartel, 1984a). In this study similar techniques were used to measure the c and b asymmetries using a sample of inclusive electron events. In what follows the identification of electrons in multihadronic events, the separation of c and b quark flavours and the analysis of the quark direction distribution made to determine the asymmetries are described in detail.

Chapter 5

ELECTRON SELECTION

The basic idea behind the selection techniques discussed in this chapter is to obtain for each charged track, from the quantities measured by the JADE detector, a figure representing the probability that the track was that of an electron. Discussion is restricted to tracks having a momentum greater than $1\,GeV/c$. This cut significantly increases the ratio of prompt to non-prompt electrons without causing the loss of many of the former as these tend to have high momenta and also makes the efficiency of the selection technique to be presented roughly independent of the track momentum. This considerably simplifies some features of the following analysis.

There are four ways in which the JADE detector can be used to identify charged particles. These are:

(a) the time taken to travel between the interaction point and the TOF counters;

(b) the penetration through the hadron filter;

(c) the energy loss per unit path length in the Jet chamber gas;

(d) and the energy deposited in the electromagnetic calorimeter.

All these techniques must be used in conjunction with a measurement of the particle's momentum. For the purpose of identifying electrons from heavy quark decays, due to their high momenta, only techniques (c) and (d) are useful.

Method (a), time of flight, relies on determining the particles speed, v, which when compared with its momentum p enables calculation of its rest mass m_0 through the relation

$$m_0 = \frac{p}{\gamma\beta}$$

where $\beta = v/c$ and $\gamma = 1/\sqrt{1-\beta^2}$. As the speed of a particle asymptotically approaches that of light with increasing momentum, separation of electrons and pions can only be achieved at momenta less than about $350\,MeV$. At higher momenta the differences in flight time between the interaction region and the TOF counters are smaller than may be resolved by the TOF system, which has a time resolution of about half a nanosecond.

Information from the muon system, method (b), is useful here only in that it enables vetoing of penetrating tracks, which are extremely unlikely to be electrons.

The electron identification process is thus based on the remaining two techniques.

Electron Selection using dE/dx.

As previously described the JADE inner detector provides a simultaneous measurement of a charged particles momentum and the energy it loses per unit length in traversing the inner detector gas dE/dx, or $\mathcal{E}$. The relationship between particle velocity and $\mathcal{E}$, described in the section on the detector, leads to the set of curves illustrated in figure 5.3 for $\mathcal{E}$ against momentum p for the particle types which occur most frequently in multihadronic events. These are, in order of increasing mass, electrons e, muons μ, pions π, kaons K and protons p. The curve for muons is not separately illustrated; as muons have approximately the same mass as pions it lies very close to the pion curve and $\mathcal{E}$ cannot be used to separate muons from pions with the JADE detector, the $\mathcal{E}$ resolution not being good enough. In the following the pion and muon tracks are considered together and 'pions' means 'pions and muons' unless explicitly otherwise stated.

As the angle between the particle and wire directions gets smaller, the quality of the $\mathcal{E}$ measurement decreases. Thus in the following analysis only tracks with $|\cos\theta| < 0.8$ are considered.

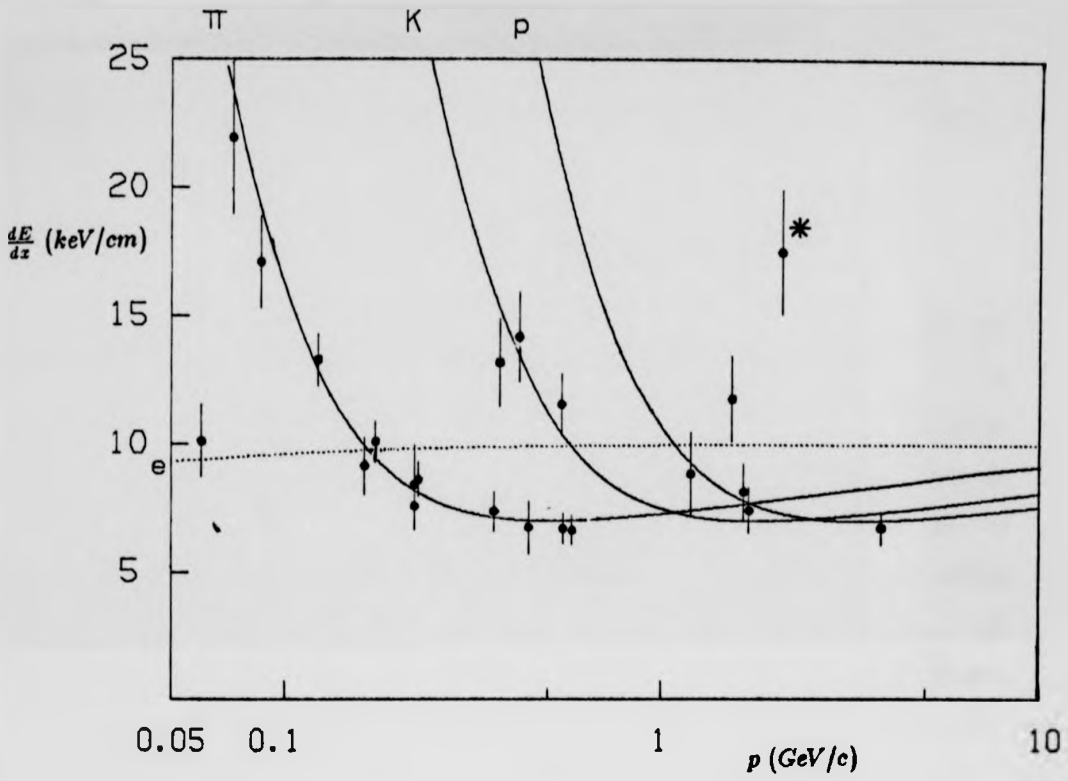

Figure 5.3. dE/dx as a function of momentum for electrons, pions, kaons and protons. The points are the dE/dx measurements obtained in a multihadronic event, that marked with an asterisk being probably the result of a deuteron formed in an interaction in the beampipe.

For each charged track, using the measured values of $\mathcal{E}$, its standard error $\sigma_{\mathcal{E}}$, p and its standard error σ_p, the quantity

$$\chi^2 = \left(\frac{p^T - p}{\sigma_p}\right)^2 + \left(\frac{\mathcal{E}^T - \mathcal{E}}{\sigma_{\mathcal{E}}}\right)^2$$

was calculated for the hypotheses that it be that of an electron, a pion, a kaon and a proton. The quantities p^T and $\mathcal{E}^T(p^T)$ come from the theoretical curve for the particle type in question, as plotted in figure 5.3. For each of the four hypotheses it was necessary to recalculate σ_p as a component of the momentum measurement error arises from multiple Coulomb scattering, the degree of which is dependent on the particle mass. For each hypothesis the value of χ^2 was minimised by varying p^T and hence $\mathcal{E}^T(p^T)$. Thus four minimum values of χ^2 were obtained, χ^2_e, χ^2_π, χ^2_K and χ^2_p. These are related to the likelihood that the track in question be an e, a π, a K or a p.

As the variation of $\mathcal{E}^T$ with p^T is slow in the momentum range under consideration, the values of the minima of χ^2 for the different particle hypotheses are dominated by the $\left((\mathcal{E}^T - \mathcal{E})/\sigma_{\mathcal{E}}\right)^2$ term.

From these values may be calculated the relative frequency with which a dE/dx measurement in the range $\mathcal{E}$ to $\mathcal{E} + d\mathcal{E}$, with a precision given by $\sigma_{\mathcal{E}}$, occurs for each particle type, assuming these measurements to be normally distributed. This is

$$\begin{aligned} f_i(\mathcal{E})d\mathcal{E} &= \frac{1}{\sqrt{2\pi}\sigma_{\mathcal{E}}} \exp\left[-\frac{1}{2}\left(\frac{\mathcal{E} - \mathcal{E}_i^T}{\sigma_{\mathcal{E}}}\right)^2\right] d\mathcal{E} \\ &= \frac{1}{\sqrt{2\pi}\sigma_{\mathcal{E}}} \exp\left[-\frac{\chi_i^2}{2}\right] d\mathcal{E} \end{aligned}$$

where the subscript i runs over the particle types e, π, K, p. To improve the accuracy of the assumption that the dE/dx values were normally distributed, only tracks for which fifteen or more dE/dx measurements had been made where used.

The required quantity, the probability that the track whose measured dE/dx

is $\mathcal{E}$ is that of an electron, is then

$$p_e(\mathcal{E}) = \frac{R_e f_e(\mathcal{E})}{\sum_i R_i f_i(\mathcal{E})} = \frac{R_e \exp\left[-\frac{\chi_e^2}{2}\right]}{\sum_i R_i \exp\left[-\frac{\chi_i^2}{2}\right]}$$

where the R_i are the relative numbers of the various track types, defined so that $\sum_i R_i = 1$, and are functions of the track momentum. They were obtained by fitting analytic functions to the ratios of particle types as functions of momentum obtained from the Monte-Carlo. Polynomials of order six were found to give perfectly adequate fits. The functions are illustrated in figure 5.4.

The R_i may also be dependent on other variables, perhaps including the event flavour and whether the jet in which the particle is found had as parent a gluon or a quark. Thus more precisely the above may be written

$$p_e(\mathcal{E}) = p_e(\mathcal{E}, p, \text{flavour, jet type,...}).$$

In the following section the accuracy with which the R may be represented simply as functions of momentum is investigated.

To check that the above formalism gives sensible results, consider the behaviour of p_e in the following three limiting cases:-

(a) The measured value of $\mathcal{E}$ is close to the $(p^T, \mathcal{E}^T(p^T))$ curve for electrons and the measurement error is small. In this case χ_e^2 is small and χ_π^2, χ_K^2 and χ_p^2 are large. Hence $\exp(-\chi_e^2/2) \approx 1$ and $\exp(-\chi_\pi^2/2) \approx \exp(-\chi_K^2/2) \approx \exp(-\chi_p^2/2) \approx 0$, thus $p_e \approx 1$.

(b) The error of the $\mathcal{E}$ measurement is large. In this case $\chi_e^2 \approx \chi_\pi^2 \approx \chi_K^2 \approx \chi_p^2$ are small and $p_e \approx R_e$, consistent with no information being available.

is $\mathcal{E}$ is that of an electron, is then

$$p_e(\mathcal{E}) = \frac{R_e f_e(\mathcal{E})}{\sum_t R_t f_t(\mathcal{E})} = \frac{R_e \exp\left[-\frac{\chi_e^2}{2}\right]}{\sum_t R_t \exp\left[-\frac{\chi_t^2}{2}\right]}$$

where the R_t are the relative numbers of the various track types, defined so that $\sum_t R_t = 1$, and are functions of the track momentum. They were obtained by fitting analytic functions to the ratios of particle types as functions of momentum obtained from the Monte-Carlo. Polynomials of order six were found to give perfectly adequate fits. The functions are illustrated in figure 5.4.

The R_t may also be dependent on other variables, perhaps including the event flavour and whether the jet in which the particle is found had as parent a gluon or a quark. Thus more precisely the above may be written

$$p_e(\mathcal{E}) = p_e(\mathcal{E}, p, \text{flavour}, \text{jet type}, \ldots).$$

In the following section the accuracy with which the R may be represented simply as functions of momentum is investigated.

To check that the above formalism gives sensible results, consider the behaviour of p_e in the following three limiting cases:-

(a) The measured value of $\mathcal{E}$ is close to the $(p^T, \mathcal{E}^T(p^T))$ curve for electrons and the measurement error is small. In this case χ_e^2 is small and χ_π^2, χ_K^2 and χ_p^2 are large. Hence $\exp(-\chi_e^2/2) \approx 1$ and $\exp(-\chi_\pi^2/2) \approx \exp(-\chi_K^2/2) \approx \exp(-\chi_p^2/2) \approx 0$, thus $p_e \approx 1$.

(b) The error of the $\mathcal{E}$ measurement is large. In this case $\chi_e^2 \approx \chi_\pi^2 \approx \chi_K^2 \approx \chi_p^2$ are small and $p_e \approx R_e$, consistent with no information being available.

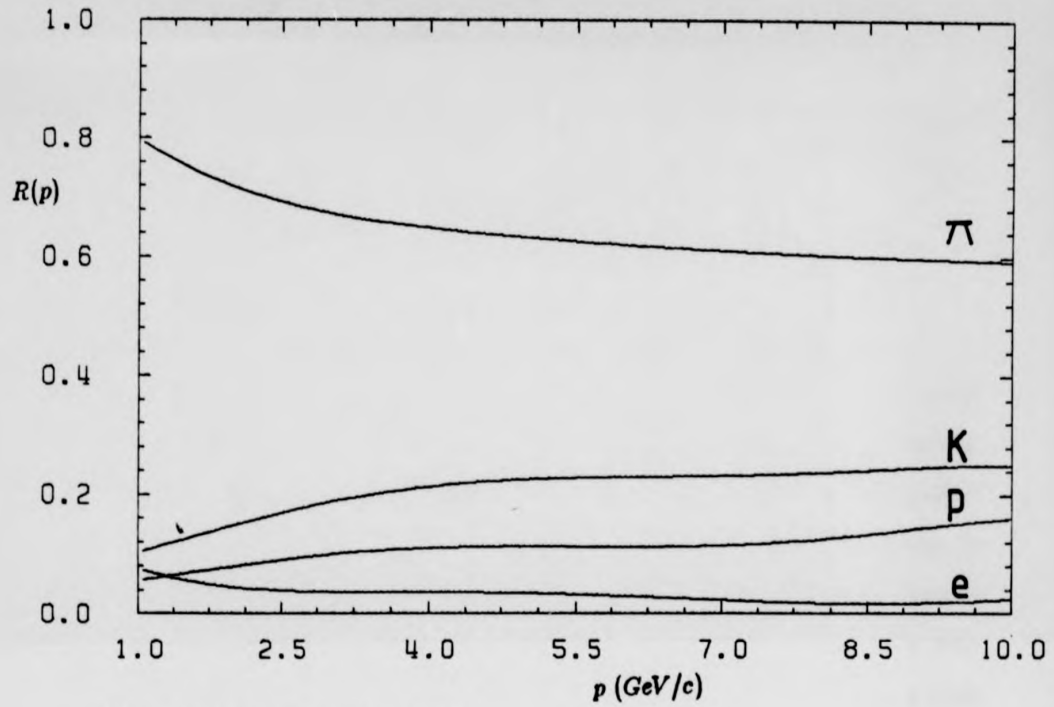

Figure 5.4. The functions $R_i(p)$.

(c) $\mathcal{E}$ is accurately measured, and consistent with the value expected for a π. In this case, interchanging the roles of the e and the π in (a) above, $p_e \approx 0$.

Thus p_e is seen to behave correctly.

There is one situation in which the p_e calculation above may give a large result for non-electron tracks. This will occur if, due to some error in a measurement, the value of $\mathcal{E}$ is spuriously high for the momentum of the track under consideration, or if a doubly charged particle is produced as a result of an interaction in the beampipe (see the example below). Such cases are rare as was determined by studying the distribution of $\mathcal{E}$ measurements in the momentum range used. Nevertheless they were guarded against by requiring that the measured dE/dx could reasonably be that of an electron. The probability of χ_e^2

$$p(\chi_e^2) = \frac{1}{\sqrt{2\pi}} \int_{-\infty}^{-\chi_e^2} \exp\left(-\frac{x^2}{2}\right) dx + \frac{1}{\sqrt{2\pi}} \int_{\chi_e^2}^{\infty} \exp\left(-\frac{x^2}{2}\right) dx$$
$$= 1 - \sqrt{\frac{2}{\pi}} \int_0^{\chi_e^2} \exp\left(-\frac{x^2}{2}\right) dx$$

was required to be greater than 0.05. Only 5% of genuine electron tracks give p and $\mathcal{E}$ measurements leading to this or larger values of $p(\chi_e^2)$. Rejecting tracks with $p(\chi_e^2) < 0.05$ thus rejects only 5% of the genuine electron tracks, while disposing of those tracks arising from doubly charged particles or in which some systematic effect has introduced a gross error in the dE/dx or p measurement.

The dE/dx against p plots in figure 5.3 have superimposed on them the measured dE/dx values of the tracks in a multihadronic event. A low energy electron, a track which is probably an electron with a momentum of about $1.2\,GeV$ and several kaons and pions can all be clearly seen. The point marked with an asterisk is the measurement for a track which originates in the beampipe and which is probably that of a deuteron, hence the large dE/dx value.

The accuracy of the p_e determination described above was checked using the lead-glass information as is described in the next section.

The Lead-Glass Information and Electron Selection.

Electrons entering the lead-glass are expected to lose all their remaining energy in an electromagnetic shower. In the momentum range considered here all other types of charged particles lose only a small fraction of their energy in passing through the electromagnetic calorimeter. Thus a comparison of the particle's momentum p with the energy it deposits in the electromagnetic calorimeter E_c enables the identification of electrons. In particular the quantity $Z = E_c/p$ is near one for electrons and smaller for other particle types.

Again only tracks with $|\cos\theta| < 0.8$ are considered, that is tracks which entered the barrel section of the electromagnetic calorimeter. As the endcap sections are shallower than the barrel section the quality of the E_c measurement obtained there is not as good as that for barrel tracks. The larger size of the endcap lead-glass blocks and the poorer θ determination for tracks close to the beampipe makes track shower association poorer in the endcaps. Furthermore, for tracks which enter the endcaps, the momentum measurement, determined from $p = p_{xy}/\sin\theta$, is also in general less accurate than that for barrel tracks. The combination of these factors leads to significantly poorer Z measurements in the endcaps.

In order to produce, from the Z measurement for a given track, the probability that the track be an electron, the Z distributions for electrons and other types of tracks must be determined. The development of electron showers in the lead-glass is accurately modelled in the Monte-Carlo. The electron Z distribution may thus be found by histogramming the Z values of Monte-Carlo electron data. The result is shown in figure 5.5. A peak is seen at one as expected, but this is far from the only feature of the distribution. There are a significant number of tracks with Z values both considerably less and considerably more than one.

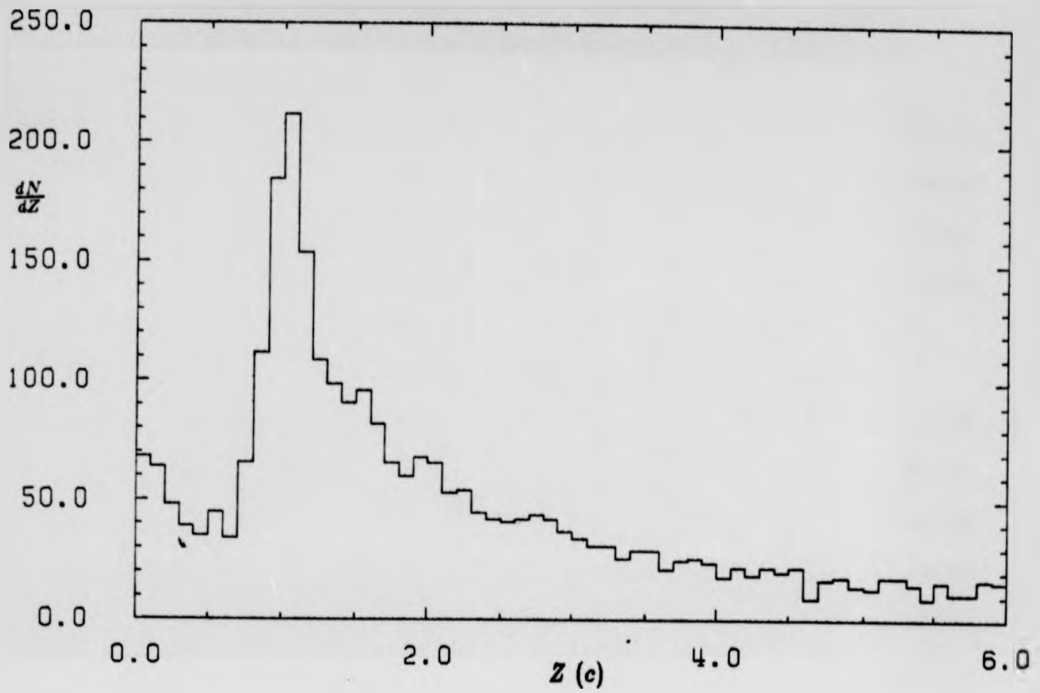

Figure 5.5. Monte-Carlo electron track Z distribution.

The electron tracks with $Z << 1$ are primarily the result of poorly made E_c measurements, in which the electromagnetic shower was not completely contained in the lead-glass. This gives rise to E_c values smaller than the energy, or momentum which is approximately equal to the energy for electrons at these momenta, thus $Z = E_c/p$ is less than one.

The electron tracks with $Z >> 1$ are due to three effects. The first is only significant for electrons. These, being light particles, have a reasonable probability of emitting a bremsstrahlung photon of significant energy as they pass through the material of the beampipe and the inner detector. If the electron leaves the interaction region with an energy or momentum of E, and then in the beampipe emits a photon of energy E_γ, the momentum that is measured in the inner detector is $p = E - E_\gamma$. The emitted photon and electron travel in close proximity as the radius of curvature of tracks in the momentum range studied here is large. They then produce electromagnetic showers at the points where they enter the electromagnetic calorimeter. These showers are often closer together than the spatial resolution of the lead-glass system, in which case they are seen as only one shower and assigned to the electron track. The measured electron shower energy is then $E_c = E$ and this gives $Z = E/(E - E_\gamma)$, which is greater than one.

The second effect occurs in both the Z distribution for electron tracks and that for non-electron tracks. It is also a result of the finite resolution with which the position of electromagnetic showers may be determined, the contamination of the electromagnetic showers being due to photons in the event coincidentally causing a shower so close to that due to the charged particle that the two showers cannot be resolved. This occurs relatively frequently as in a typical jet about seven charged particles and approximately the same number of photons are produced in a cone of half-angle only 15° (Bartel, 1985).

The third effect is associated with charged ρ decays. These produce one

charged and one neutral pion which decays into a photon pair. The charged pion and one of the photons are then quite likely to enter the lead-glass within the shower position resolution, again causing the measured value of Z to be large.

The peak at one in the electron Z distribution appears to be Gaussian and more precise study reveals that this is indeed the case. This arises as the measurments of both E_c and $1/p$ are normally distributed, for the tracks for which the effects mentioned above are not significant, hence the Z distribution around one has a Gaussian distribution.

The Z distribution for non-electron tracks was not taken directly from the Monte-Carlo, as the simulation of the electromagnetic showers for these tracks was not sufficiently accurate. Instead the Z distribution from the real data, with the (small) electron contribution subtracted out, was used. The subtraction required the use of the electron Z distribution shown in figure 5.5 and the relative numbers of electron and non-electron tracks. This method ensured that only the Monte-Carlo quantities which were accurately simulated were used. The Z distribution for all tracks, and the subtraction made from it, are shown in figure 5.6. The resulting Z distribution for non-electron tracks is shown in figure 5.7. It is peaked at a value of Z well below one, but as expected from the arguments above there is a tail out to high values of Z.

In addition to the effects described above, a small contribution to the high Z tail of the non-electron Z distribution arises from anti-protons. The annihilation of these in the lead-glass results in the deposition of an energy of approximately $1\,GeV$. This, together with the energy due to the anti-proton's motion, gives rise to tracks having $Z > 1$ for anti-protons with momenta at the low end of the range considered here.

The two Z distributions were then fitted using, in the non-electron case a

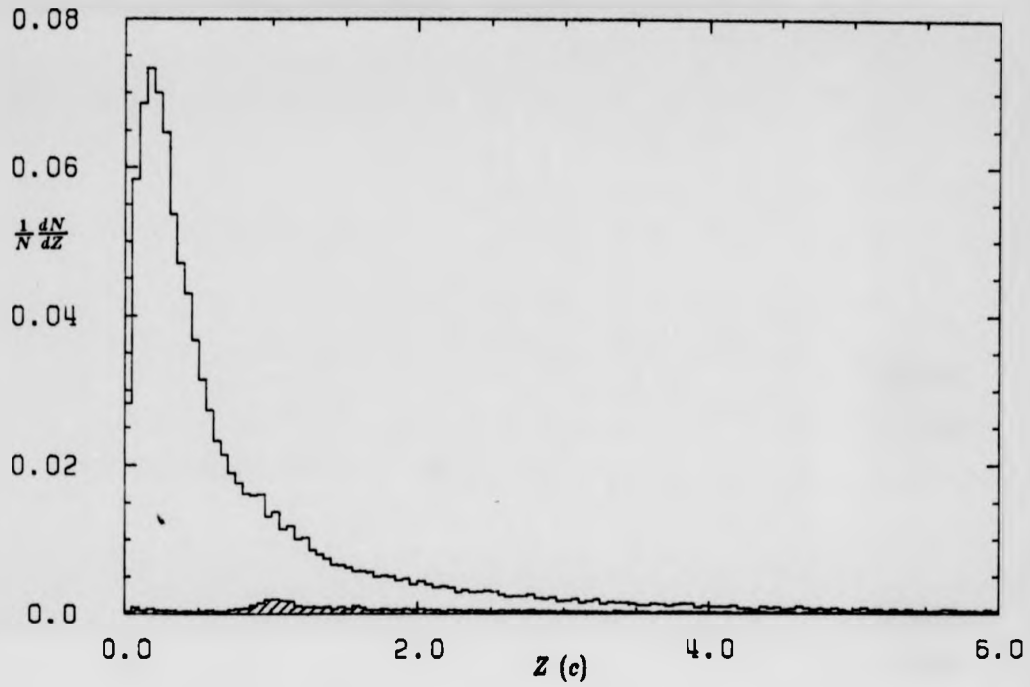

Figure 5.6. The Z distribution of all charged tracks from the real data, the electron contribution is shaded.

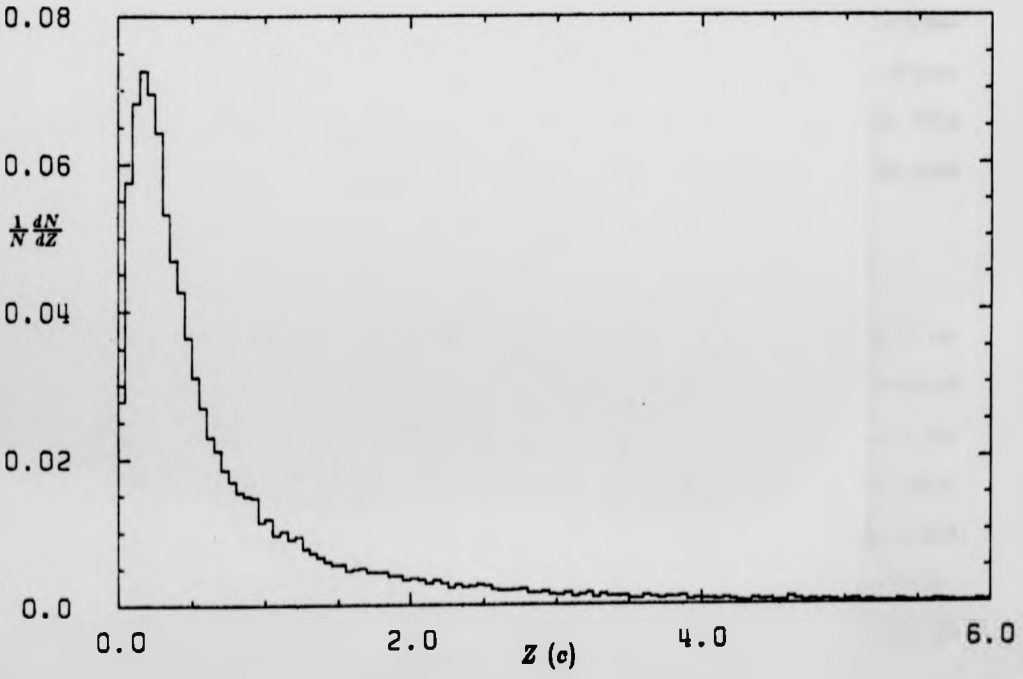

Figure 5.7. The Z distribution for non-electron tracks.

function of the form

$$\omega_\tau(Z) = \frac{\sum_{i=0}^{n} a_i Z^i}{1 + Z^{n+2}}$$

and in the electron case

$$\omega_e(Z) = \frac{\sum_{i=0}^{n} a_i Z^i}{1 + Z^{n+2}} + \frac{1}{\sqrt{2\pi}\sigma} \exp\left[-\frac{1}{2}\left(\frac{Z-\mu}{\sigma}\right)^2\right]$$

the a_i and the parameters of the Gaussian being free. The maximum likelihood technique was used, good fits being obtained with $n = 8$. These functions were then normalized to one.

Cross Checking the dE/dx Selection.

A check of the dE/dx selection and the accuracy of the Z distributions was performed as follows. Nine samples of tracks were selected, using the dE/dx selection variable p_e, and requiring for the first sample $0.1 < p_e < 0.2$, for the second $0.2 < p_e < 0.3$ and so on up to the ninth sample for which $0.9 < p_e < 1.0$. The Z distributions of these samples were then plotted. The histogram for the fourth and ninth samples are shown in figures 5.8 and 5.9 respectively. If the variable p_e correctly represents the probability that the tracks be those of electrons then these samples should consist of a proportion $\bar{p}_e$ of electron and $1 - \bar{p}_e$ of non-electron tracks, $\bar{p}_e$ being the mean value of p_e for the tracks in the sample. This was checked by fitting the normalized Z distributions for each of the samples with the function

$$F(Z) = r_e\omega_e(Z) + (1 - r_e)\omega_\tau(Z)$$

using the maximum likelihood method. The value of the free parameter r_e returned by the fit is then the proportion of electrons in the sample as determined using the lead-glass information. If the approximations made in calculating the dE/dx selection variable p_e are sufficiently accurate, namely the dE/dx distribution is Gaussian and the particle type ratios R_i may be reasonably represented as functions of momentum only, and the distributions ω_e and ω_τ are correctly determined, then the value of r_e for a sample of tracks selected as above should be

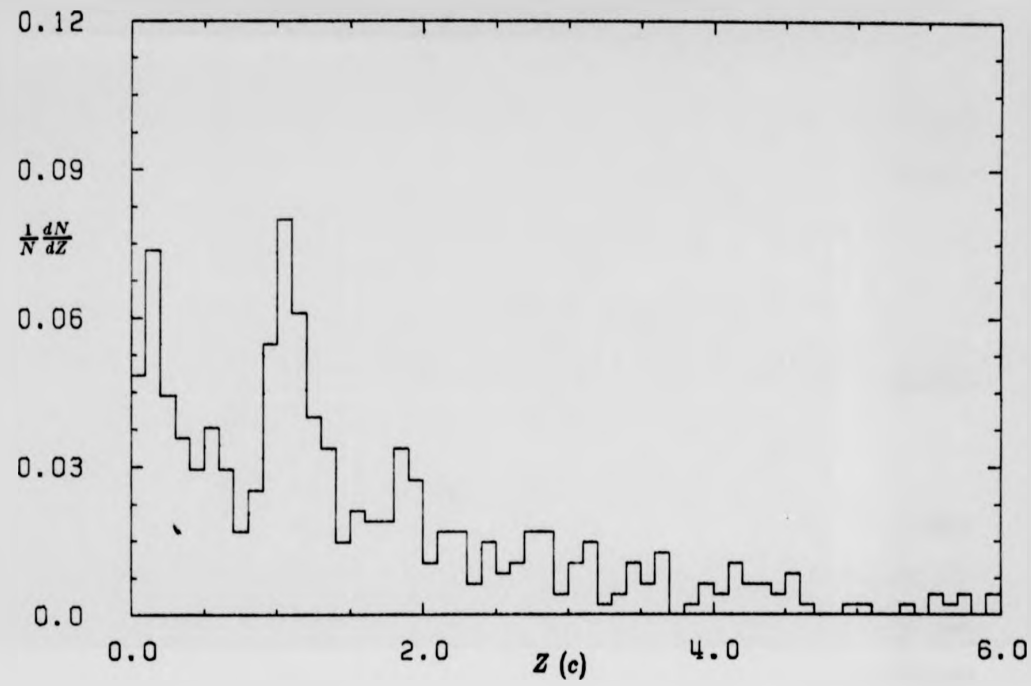

Figure 5.8. The Z distribution of the sample of tracks with $0.4 < p_e < 0.5$.

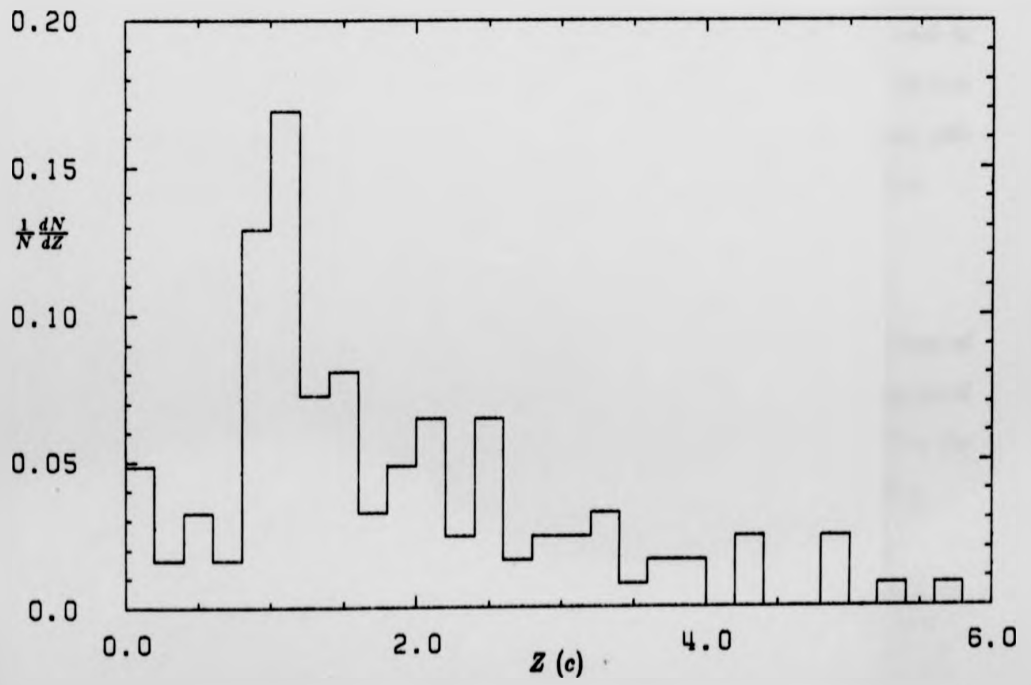

Figure 5.9. The Z distribution of the sample of tracks with $0.9 < p_e < 1.0$.

compatible with the value of $\bar{p}_e$. A plot of r_e against $\bar{p}_e$ should be a straight line through the origin with gradient one. That this is the case is illustrated in figure 5.10. The line illustrated is the result of a least squares fit using

$$r_e = m\bar{p}_e + c.$$

The values of m and c are 0.980 and 0.00975 respectively. The fit has a probability of χ^2 of 0.45.

A further indication that the above selection procedure is reliable is provided by figure 5.11. In this figure the Z values of all tracks with $p_e > 0.1$ are plotted. The electron peak at $Z = 1$ is clearly visible. The line is the $F(Z)$ curve in which r_e has been set to the mean value of p_e for the selected tracks and clearly represents the data well.

Selection Variable from the Lead-Glass Information.

Due to the asymmetry of the Z distribution it is not possible to use the same technique to form a selection variable using the Z information as was used to obtain p_e. However, from the relative frequency distributions of Z for electron and non-electron tracks, ω_e and ω_r respectively, the probability that a track with a measured value of $E_c/p = Z$ is that of an electron may be calculated. It is

$$q_e = \frac{R_e\omega_e}{R_e\omega_e + R_r\omega_r}$$

where $R_r = R_\pi + R_K + R_p$ and the R_i are the same particle ratios, functions of momentum, used in forming the dE/dx selection variable p_e. The disadvantage of using this as opposed to the previous technique is that the error with which the Z measurement was made cannot be incorporated in the determination of q_e.

compatible with the value of $\bar{p}_e$. A plot of r_e against $\bar{p}_e$ should be a straight line through the origin with gradient one. That this is the case is illustrated in figure 5.10. The line illustrated is the result of a least squares fit using

$$r_e = m\bar{p}_e + c.$$

The values of m and c are 0.980 and 0.00975 respectively. The fit has a probability of χ^2 of 0.45.

A further indication that the above selection procedure is reliable is provided by figure 5.11. In this figure the Z values of all tracks with $p_e > 0.1$ are plotted. The electron peak at $Z = 1$ is clearly visible. The line is the $F(Z)$ curve in which r_e has been set to the mean value of p_e for the selected tracks and clearly represents the data well.

Selection Variable from the Lead-Glass Information.

Due to the asymmetry of the Z distribution it is not possible to use the same technique to form a selection variable using the Z information as was used to obtain p_e. However, from the relative frequency distributions of Z for electron and non-electron tracks, ω_e and ω_r respectively, the probability that a track with a measured value of $E_c/p = Z$ is that of an electron may be calculated. It is

$$q_e = \frac{R_e\omega_e}{R_e\omega_e + R_r\omega_r}$$

where $R_r = R_\pi + R_K + R_p$ and the R_i are the same particle ratios, functions of momentum, used in forming the dE/dx selection variable p_e. The disadvantage of using this as opposed to the previous technique is that the error with which the Z measurement was made cannot be incorporated in the determination of q_e.

compatible with the value of $\bar{p}_e$. A plot of r_e against $\bar{p}_e$ should be a straight line through the origin with gradient one. That this is the case is illustrated in figure 5.10. The line illustrated is the result of a least squares fit using

$$r_e = m\bar{p}_e + c.$$

The values of m and c are 0.980 and 0.00975 respectively. The fit has a probability of χ^2 of 0.45.

A further indication that the above selection procedure is reliable is provided by figure 5.11. In this figure the Z values of all tracks with $p_e > 0.1$ are plotted. The electron peak at $Z = 1$ is clearly visible. The line is the $F(Z)$ curve in which r_e has been set to the mean value of p_e for the selected tracks and clearly represents the data well.

Selection Variable from the Lead-Glass Information.

Due to the asymmetry of the Z distribution it is not possible to use the same technique to form a selection variable using the Z information as was used to obtain p_e. However, from the relative frequency distributions of Z for electron and non-electron tracks, ω_e and ω_r respectively, the probability that a track with a measured value of $E_c/p = Z$ is that of an electron may be calculated. It is

$$q_e = \frac{R_e\omega_e}{R_e\omega_e + R_r\omega_r}$$

where $R_r = R_\pi + R_K + R_p$ and the R_i are the same particle ratios, functions of momentum, used in forming the dE/dx selection variable p_e. The disadvantage of using this as opposed to the previous technique is that the error with which the Z measurement was made cannot be incorporated in the determination of q_e.

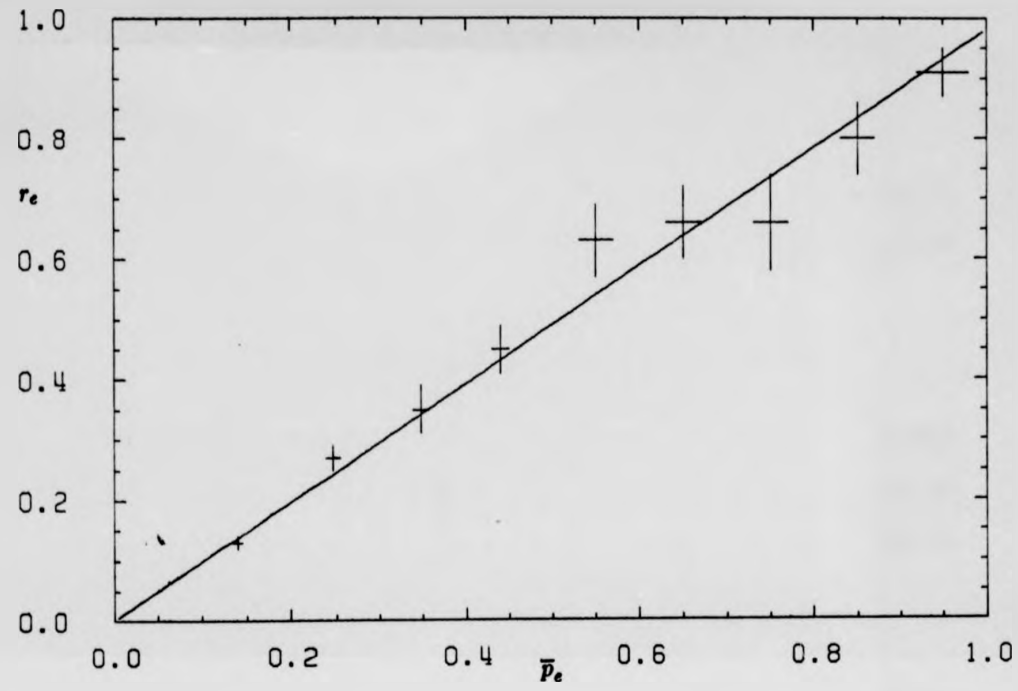

Figure 5.10. The purity of electron samples r_e as a function of the mean values of p_e for the samples.

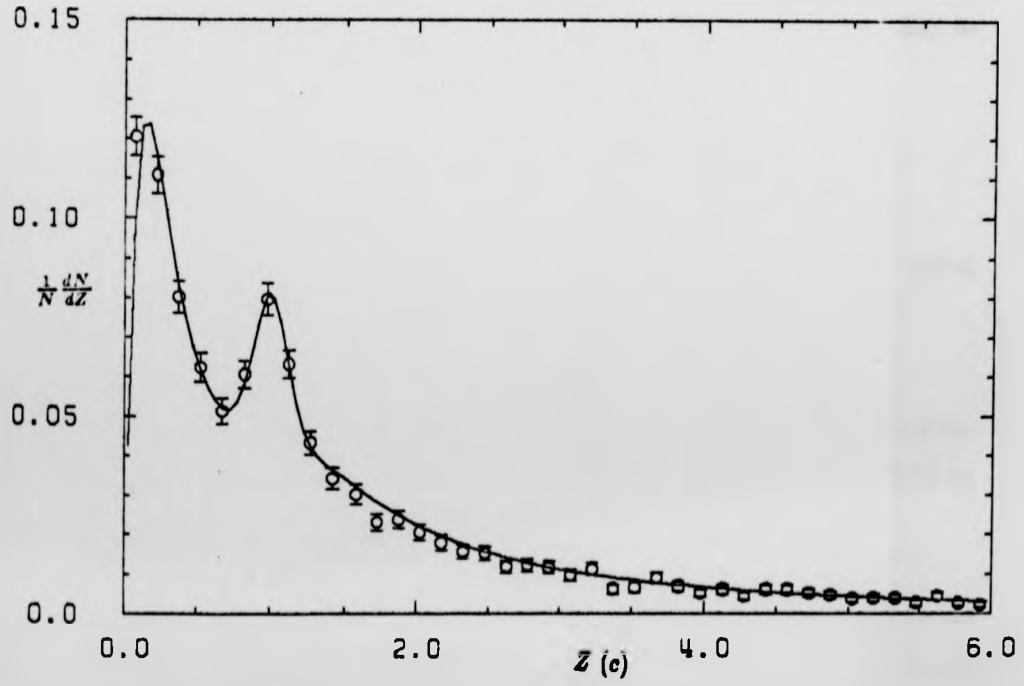

Figure 5.11. The Z distribution of all tracks with $p_e > 0.1$ (circles) compared with the distribution expected from the mean value of p_e (line).

Combination of the Selection Information.

Combining all the track type identification information available, the probability that a track with a measured value of dE/dx of $\mathcal{E}$, with error $\sigma_{\mathcal{E}}$ and $E_c/p = Z$ is an electron track is

$$P_e = \frac{R_e \rho_e(\mathcal{E}, Z)}{R_e \rho_e(\mathcal{E}, Z) + R_\tau \rho_\tau(\mathcal{E}, Z)}$$

where ρ_e is the two-dimensional relative frequency distribution of $\mathcal{E}$ and Z for electron tracks and ρ_τ that for non-electron tracks. As Z and $\mathcal{E}$ are independent, the ρ are equivalent to the products of the relevant one-dimensional relative frequency functions. Thus

$$\rho_e(\mathcal{E}, Z) = \delta_e(\mathcal{E})\omega_e(Z)$$

where $\delta_e(\mathcal{E})$ is the $\mathcal{E}$ relative frequency function for electron tracks. From the previous discussion this is

$$\delta_e(\mathcal{E}) = \frac{1}{\sqrt{2\pi}\sigma_{\mathcal{E}}} \exp\left[-\frac{\chi_e^2}{2}\right].$$

Similar expressions may be written for δ_π, δ_K and δ_p from which ρ_τ may be calculated.

$$\rho_\tau(\mathcal{E}, Z) = \frac{1}{R_\tau}\Big(R_\pi \rho_\pi(\mathcal{E}, Z) + R_K \rho_K(\mathcal{E}, Z) + R_p \rho_p(\mathcal{E}, Z)\Big).$$

The combined probability P_e may alternatively be calculated from p_e and q_e using

$$P_e(\mathcal{E}, Z) = \frac{R_\tau p_e(\mathcal{E}) q_e(Z)}{R_\tau p_e(\mathcal{E}) q_e(Z) + R_e p_\tau(\mathcal{E}) q_\tau(Z)}$$

as may be checked by substitution. Calculating P_e in this manner has the advantage that, for tracks in which only one of $\mathcal{E}$ and Z was measured, P_e may be set to the one-dimensional value which was available.

The above analysis was carried out for all barrel tracks. Only those tracks for which both Z and $\mathcal{E}$ information was available were used in the following

study to reduce the risk of systematic errors occurring in the electron selection. Electron signals are faked by only one type of rarely occurring track, namely anti-protons with a momentum of about $1\,GeV/c$. These have about the same dE/dx as electrons and also, as they annihilate in the lead-glass, deposit a large amount of energy in the electromagnetic calorimeter. These tracks were removed as far as possible using the TOF information, the resolution of the TOF system being quite adequate for separating $1\,GeV/c$ electrons and anti-protons. The transverse momentum spectrum of the remaining $1\,GeV/c$ anti-protons is very different from that of the prompt electrons and thus they do not affect the measurement of the c and b asymmetries.

Chapter 6

Flavour Separation

Having a method for identifying electrons in multihadronic events, the next problem that must be addressed is that of separating the events according to their flavour. There are two ways in which this may be done:

(a) by identifying a particular particle which occurs predominantly in events of only one flavour, for example D and D^* mesons which occur essentially only in c events;

(b) by studying the mass of the primary quark, heavy primary quarks giving rise to characteristic signatures.

Method (a) has been used with some success (eg. Bartel, 1984b), the problem being that of finding a reasonable number of events in which the particle type in question was produced. As there is no easily identifiable particle which occurs predominantly in b events, this technique will not be considered here.

In practice, to exploit method (b), some variable x, which may be multi-dimensional and whose distribution is dependent on the initial quark masses must be found. For an ideal separation variable, the probability density functions of x for the different flavours would be distinct, as illustrated in figure 6.1. Cuts at the indicated values of x would then give complete flavour separation. Unfortunately no such variable has been found and it is unlikely that one will be. Real separation variables have probability density functions that overlap considerably between flavours, as illustrated in figure 6.2. In this case the probability density functions for d, u and s quark events are so similar, as the quark masses are similar, that no separation is possible between these flavours. This is the case for all the separation variables that will be considered in the following so for convenience these three flavours will henceforth be collectively labelled r.

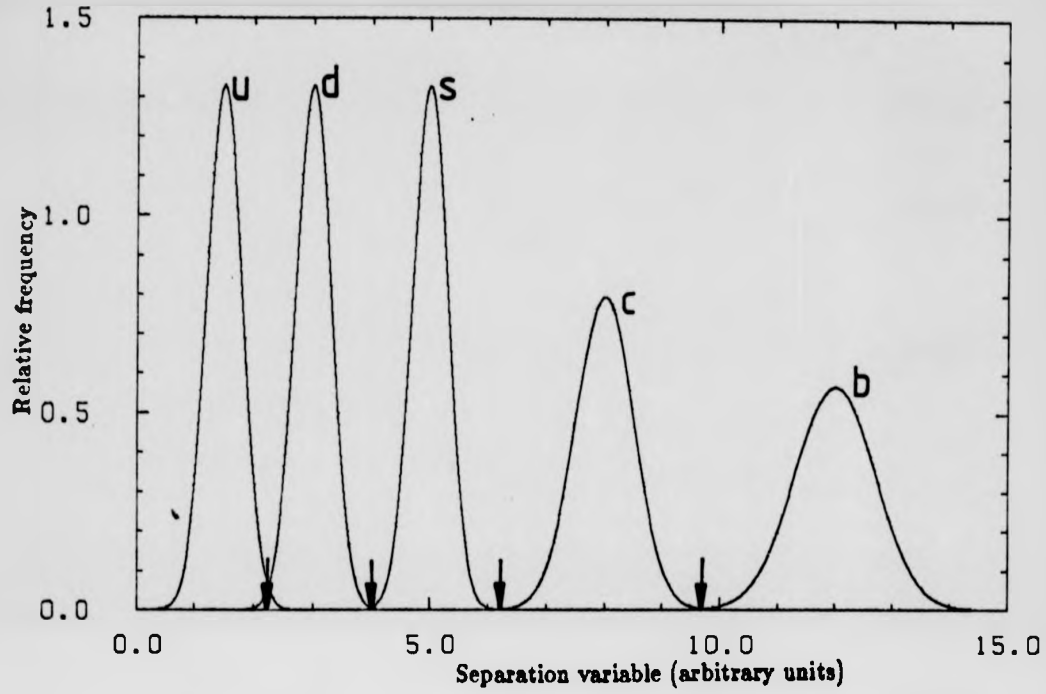

Figure 6.1. An ideal separation variable. The arrows indicate cuts that give almost complete flavour separation.

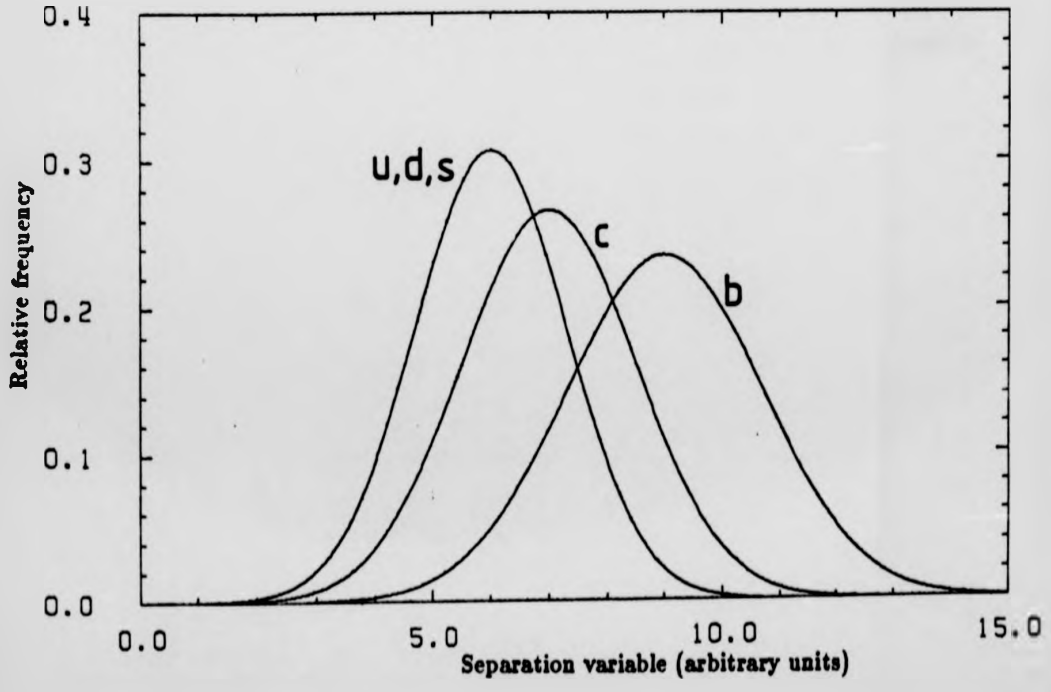

Figure 6.2. A typical separation variable.

In order to find the best separation variable it is necessary to quantify the amount of overlap of the probability functions, this being the factor that determines the degree of separation that may be obtained. This may be done as follows (Marshall, 1984a).

Let the probability density functions for r, c and b be $\rho_r(x)$, $\rho_c(x)$ and $\rho_b(x)$ respectively. Normalize these functions so that

$$\int_{-\infty}^{\infty} \rho_i^2(x)\,dx = 1$$

for $i = r, c, b$. Consider the matrix $\mathbf{M}$ formed by the coefficients

$$M_{ij} = \int_{-\infty}^{\infty} \rho_i(x)\rho_j(x)\,dx$$

where j also runs over r, c and b. The diagonal elements of $\mathbf{M}$ are then by definition one and the off-diagonal elements between zero and one. $M_{ij} = 0$ implies there is no overlap between the i and j distributions, that is the separation in x is complete. $M_{ij} = 1$ implies that $\rho_i(x) \equiv \rho_j(x)$ and x allows no separation between the flavours i and j. The smaller the value of M_{ij} the better the separation between the flavours i and j achievable using the variable x.

This technique was used to study the following separation variables:–

(a) Thrust T

(b) Sphericity S

(c) Transverse mass M

(d) Electron transverse momentum $p_T(e)$

(e) Electron isolation I

(f) Multiplicity N

These are defined as follows.

(a) Thrust.

The thrust of a multihadronic event is the quantity

$$T = \max \left[\frac{\sum_i |p_L|_i}{\sum_i p_i} \right]$$

The maximisation is performed by variation of the direction of the axis along which the modulus of the component of the i^{th} track's momentum, $|p_L|_i$, is calculated. p_i is the absolute value of the track's momentum, i running over all the charged and neutral tracks in the event. The direction which maximises the expression above is termed the thrust axis. Monte-Carlo studies show that it represents the initial $q\bar{q}$ direction to an accuracy of about 5°. The maximum possible value of T, indicating that the event has a very pronounced two-jet shape, is one. The minimum value, indicating that the event is spherical, is 1/2. The flavour selecting power of T arises as heavy quark events tend to be somewhat more spherical than other events, due to the tracks from the weak decay of the heavy quark which receive momentum transverse to the quark direction in the decay.

(b) Sphericity.

The sphericity is determined from the tensor

$$T_{\alpha\beta} = \frac{\sum_i (p_i)_\alpha (p_i)_\beta}{\sum_i p_i^2},$$

i running over all charged and neutral tracks in an event, apart from those observed to come from a decay, in which case the momentum of the parent particle was used. This procedure is advisable as the quadratic manner in which the track momenta enter the sphericity calculation means that decays are not correctly treated. The $(p_i)_\alpha$ are the x, y and z components of the momentum of the i^{th} track, as are the $(p_i)_\beta$. Diagonalization of $T_{\alpha\beta}$ yields the unit eigenvectors $\hat{\mathbf{q}}_1$, $\hat{\mathbf{q}}_2$ and $\hat{\mathbf{q}}_3$, and the corresponding eigenvalues

$$Q_j = \frac{\sum_i (\mathbf{p}_i \cdot \hat{\mathbf{q}}_j)^2}{\sum_i p_i^2}$$

These, ordered so that $Q_1 < Q_2 < Q_3$, describe respectively the flatness, width and length of an event in momentum space. The eigenvector $\hat{\mathbf{q}}_3$ is the event axis and represents the $q\bar{q}$ direction to about the same accuracy as the thrust axis; $\hat{\mathbf{q}}_1$ is normal to the event plane and $\hat{\mathbf{q}}_2$ is a vector in the event plane.

The sphericity is defined by

$$S = \frac{3}{2}(Q_1 + Q_2)$$
$$= \frac{3}{2}(1 - Q_3).$$

The maximum value of S is one, and indicates a spherical event shape. The minimum value is zero and indicates a two jet event shape. The usefulness of S as a separation variable arises as described above for thrust.

(c) Transverse Mass.

The transverse mass M is defined as

$$M = 2\frac{E_{\text{beam}}}{E_{\text{vis}}} \sum_i |\mathbf{E}_i \cdot \hat{\mathbf{n}}|$$

where

$$\mathbf{E}_i = E_i \frac{\mathbf{p}_i}{p_i}$$

that is a vector with the magnitude of the particle energy and the direction of the particle momentum. In practice $\mathbf{E}_i$ was calculated assuming all charged particles to be pions and all neutrals to be photons. The vector $\hat{\mathbf{n}}$ is the unit vector normal to the event plane, the $\hat{\mathbf{q}}_1$ vector was used here. The factor $2E_{\text{beam}}/E_{\text{vis}}$ makes M insensitive to the loss of particles due to detection inefficiencies.

This variable is directly related to the mass of the parent quarks in an event, as may be seen by the following argument. Consider a particle of mass m which decays isotropically in its rest frame. The energy per unit solid angle is then e where

$$4\pi e = m.$$

Calculate M

$$M = \sum_i |\mathbf{E}_i \cdot \hat{\mathbf{n}}|$$
$$= \sum_i |E_i \sin\theta_i \cos\phi_i|$$

where an orthonormal coordinate system with axes $\hat{\mathbf{l}}$, $\hat{\mathbf{m}}$ and $\hat{\mathbf{n}}$ with the accompanying polar coordinates θ and ϕ has been defined, as illustrated in figure 6.3. The axis $\hat{\mathbf{l}}$ may be considered to be the jet axis and $\hat{\mathbf{m}}$ a vector in the event plane in the case that the particle in question is the initial quark or anti-quark in a multihadronic event. Then

$$M = \sum_i E_i \sin\theta_i |\cos\phi_i|$$
$$= \iint_\Omega e \sin\theta_i |\cos\phi_i| \, d\cos\theta \, d\phi$$
$$= e \int_0^1 \sin\theta \left[2 \int_{-\frac{\pi}{2}}^{\frac{\pi}{2}} \cos\phi \, d\phi \right] d\cos\theta$$
$$= 2\pi e$$
$$= \frac{m}{2}.$$

Returning to the multihadronic event this is the half the mass of the quark plus some contribution due to the fragmentation process. Summing over the initial quark and anti-quark, M for a multihadronic event is the quark mass plus the fragmentation contribution.

As only components out of the event plane are considered in forming M it is insensitive to the effects of single energetic gluon bremsstrahlung. This is a major advantage of M over the variables T and S in separation applications.

It has been suggested that the contribution to M arising from fragmentation is flavour independent (Marshall, 1984a). If this is the case then M provides a means of comparing the quark masses. It is certainly an excellent variable to use in the search for new particle production in electron positron annihilation. A new massive particle which decayed in such a manner as to leave a significant amount

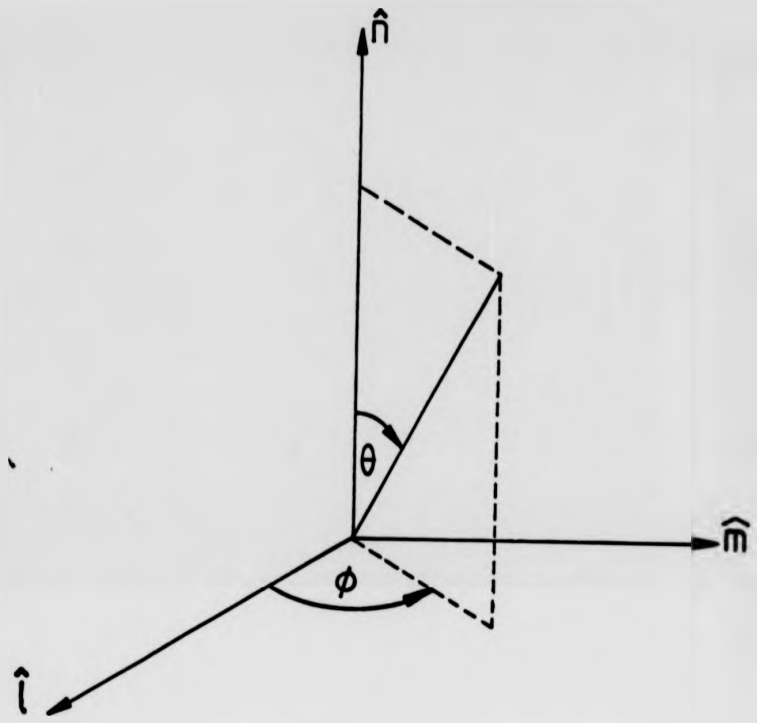

Figure 6.3. The coordinate system used in discussion of M.

of energy in the detector would be clearly visible in the M distribution (Chrin, 1984).

(d) Electron Transverse Momentum.

The electron transverse momentum, $p_T(e)$, is the component of an electron's momentum transverse to the event axis, represented by the sphericity axis $\hat{\mathbf{q}}_3$ here. If the electron had as parent a massive quark, this tends to be larger than the transverse momentum of electrons from other sources, due to the large amount of energy available in the heavy quark decay. The transverse momentum of electrons or muons is probably the most widely used flavour separation variable.

As may be deduced from the above the p_T of an electron also provides a means of separating prompt electrons from electrons from background sources in c and b events.

(e) Electron Isolation.

The electron isolation is defined to be the energy in a cone of half angle θ_c about the electron direction, excluding that of the electron itself ($\theta_c = \pi/6$ was used here). The idea being that if the electron is from a heavy quark decay it will tend to be thrown clear of the other particles in the event and thus I will be small. If the electron is from some other source then it will tend to be produced surrounded by other particles and I will be large. Two problems suggest themselves immediately. It would seem likely that I will be highly (negatively) correlated with the electron transverse momentum and also that I will be strongly dependent on the details of the fragmentation process. However it is possible that I could be useful in distinguishing electrons that have a large transverse momentum because they were produced in a hard gluon jet from those which have a large transverse momentum due to their production in the decay of a heavy quark.

(f) Multiplicity.

As was stated in the second chapter, the decay of a heavy quark often gives rise to a large number of particles and it may be possible to use this fact to identify heavy quark events. Unfortunately this effect is much reduced for semi-leptonic decays. Thus in the events under study, in which the electron is required in order to make it possible to tag the quark charge, the multiplicity is not likely to be a particularly powerful selection variable. However, in studies in which a prompt lepton is not required, perhaps including measurements of the b lifetime, multiplicity may well deserve attention as a separation variable.

Comparison of Separation variables.

The comparison of the usefulness in flavour separation of the variables above was performed as follows. Distributions of the variables were obtained from the Monte-Carlo for r, c and b events. Analytic functions of suitable form were fitted to these distributions. The normalization factors and elements of M_{ij} were obtained by numerically integrating the functions over a suitable range, the Trapezium rule

$$\int_{x_0}^{x_n} \rho_i \rho_j \, dx \approx \frac{x_n - x_0}{2n} \left(\rho_i(x_0)\rho_j(x_0) + \rho_i(x_n)\rho_j(x_n) + 2 \sum_{k=1}^{n-1} \rho_i(x_k)\rho_j(x_k) \right)$$

being used. The results are shown in the table below.

Variable	M_{cb}	M_{rb}	M_{rc}
Thrust	0.84	0.79	0.99
Sphericity	0.78	0.73	0.98
Transverse Mass	0.74	0.70	0.99
Electron p_T	0.72	0.54	0.92
Electron Isolation	0.78	0.72	0.97
Multiplicity	0.80	0.75	0.99

The most powerful separation variables are $p_T(e)$ and M.

Combination of Separation variables.

It would obviously be desirable to combine the separation variables above in order to ensure that all the available information pertinent to flavour identification is used. Here care is necessary. As the above are not independent, the probability distribution functions for a multi-dimensional separation variable formed from them cannot generally be represented by the product of the one-dimensional distributions involved. The probability density functions of the multi-dimensional variable must be obtained from multi-dimensional histograms of the $T, S, M, \ldots$ distributions. This introduces a practical problem. The amount of Monte-Carlo data that must be studied to reasonably define the distributions and the number of parameters required to describe them, for example the number of free parameters in a fit needed to obtain a reasonable analytic representation of the distribution, increases as the square of the dimensionality, thus the calculations involved rapidly become unwieldy. Furthermore, the amount of additional information included by increasing the number of variables used is only significant if the newly included variables do not duplicate information already present. For example if event shape information is used in the form of the variable T, addition of S is unlikely to lead to a significant improvement in the separation. The independence of the probability density functions for the variables above indicates the degree to which the information they contain is duplicated; completely independent variables containing no shared information and vice versa.

The (linear) dependence of two variables x_1 and x_2 may be investigated using the correlation coefficient formed from the variance of the x_1 and x_2 distributions and the covariance of their combined distribution. The correlation coefficient is

$$c = \frac{\mathrm{cov}(x_1, x_2)}{\sqrt{\mathrm{var}(x_1)}\sqrt{\mathrm{var}(x_2)}}$$

where, in terms of the expectation value defined by

$$\mathrm{E}(x) = \int_{-\infty}^{\infty} x f(x)\, dx$$
$$= \bar{x}$$

and the obvious extension of this expression to two dimensions, the variance of x_1 is

$$\mathrm{var}(x_1) = \mathrm{E}(x_1 - \bar{x}_1)$$

with an equivalent result for $\mathrm{var}(x_2)$ and the covariance is

$$\mathrm{cov}(x_1, x_2) = \mathrm{E}(x_1 x_2) - \bar{x}_1 \bar{x}_2.$$

A value of $c = 0$ indicates that the distributions in question are completely independent and vice versa for a value of plus or minus one. It must be noted that a correlation coefficient of zero is only a necessary condition for independence, not a sufficient one. Variables which are dependent on one another through some non-linear relation may have correlation coefficients of zero. For the variables of interest here, the relationships, if they exist, are likely to be linear and thus an analysis using the correlation coefficient is acceptable.

Returning now to the problem which prompted the above discussion, how many of the above variables is it worth combining to use in the separation of flavours in this case? The previously mentioned practical problems limit the number which can reasonably be used together to two or at most three. The obvious choice is to use transverse mass and electron transverse momentum p_T. (From now on p_T will be undertood to refer to electron transverse momentum.) The correlation coefficients of the M and p_T distributions are around 0.1, with slight variations between flavours, the correlation coefficient for b events being smaller, that for r events about 0.2. This implies that the information content of the two variables is significantly different and they are well worth using together.

It was decided not to include a third separation variable, as for thrust and sphericity the separation obtainable is not enough to warrant the difficulties of

their inclusion, multiplicity is also ineffective once the requirement is made that the event contain a prompt lepton and I suffers from the previously mentioned fragmentation dependence, more detailed study of this being necessary before it is understood sufficiently well to be useable as a separation variable.

Separation Techniques.

Having decided on the use of M and p_T as separation variables the problem of how best to use them arises. There are basically three techniques available. These are:

(a) using cuts;

(b) using weights;

(c) the maximum likelihood method.

Method (a) is probably the most frequently used separation technique in High Energy Physics and where the errors arising from statistical considerations are of the same size or smaller than those due to systematic effects the loss of information entailed in the use of cuts is probably justifiable as the technique is easily intuitively understood. In the case under consideration here this is not so and a more sophisticated technique must be used.

Method (b) is described by Barlow (1985). It is closely related to what is referred to as the method of moments by Marshall (1984a), although this latter does not use the optimum weight functions. Restricting the discussion, for simplicity's sake, to the case in which it is desired to determine the number of signal N_S and background N_B events in a mixture of the two the basic idea is as follows. The signal in question may be a particular flavour, or prompt as opposed to non-prompt electrons. Each event is weighted according to the probability that it comes from the signal distribution $S(x)$, x being the chosen separation variable.

If the background distribution is $B(x)$, this is

$$w(x) = \frac{N_S S(x)}{N_S S(x) + N_B B(x)}.$$

It can be shown that this is the best possible weight function, the results obtained using it being as good as those obtained using the maximum likelihood technique. The mean value of the weight function over the signal x distribution is

$$\overline{w}_S = \int_{-\infty}^{\infty} w(x) S(x)\, dx$$

and similarly

$$\overline{w}_B = \int_{-\infty}^{\infty} w(x) B(x)\, dx.$$

After weighting all of the N events in the sample according to their x values, the sum of the weightings is

$$N_w = \overline{w}_S N_S + \overline{w}_B N_B$$

and obviously

$$N = N_S + N_B.$$

These equations may be solved for the required N_S and N_B the results being

$$\begin{aligned} N_S &= \frac{N_w - \overline{w}_B N}{\overline{w}_S - \overline{w}_B} \\ &= \sum_{i=1}^{N} \left(\frac{w(x_i) - \overline{w}_B}{\overline{w}_S - \overline{w}_B} \right) \end{aligned}$$

and

$$\begin{aligned} N_B &= \frac{N_w - \overline{w}_S N}{\overline{w}_B - \overline{w}_S} \\ &= \sum_{i=1}^{N} \left(\frac{w(x_i) - \overline{w}_S}{\overline{w}_B - \overline{w}_S} \right) \end{aligned}$$

with errors given by

$$\sigma_S = \left[\sum_{i=1}^{N} \left(\frac{w(x_i) - \overline{w}_B}{\overline{w}_S - \overline{w}_B} \right)^2 \right]^{1/2}$$

and

$$\sigma_B = \left[\sum_{i=1}^{N} \left(\frac{w(x_i) - \overline{w}_S}{\overline{w}_B - \overline{w}_S} \right)^2 \right]^{1/2}$$

If the background distribution is $B(x)$, this is

$$w(x) = \frac{N_S S(x)}{N_S S(x) + N_B B(x)}.$$

It can be shown that this is the best possible weight function, the results obtained using it being as good as those obtained using the maximum likelihood technique. The mean value of the weight function over the signal x distribution is

$$\overline{w}_S = \int_{-\infty}^{\infty} w(x) S(x)\, dx$$

and similarly

$$\overline{w}_B = \int_{-\infty}^{\infty} w(x) B(x)\, dx.$$

After weighting all of the N events in the sample according to their x values, the sum of the weightings is

$$N_w = \overline{w}_S N_S + \overline{w}_B N_B$$

and obviously

$$N = N_S + N_B.$$

These equations may be solved for the required N_S and N_B the results being

$$\begin{aligned} N_S &= \frac{N_w - \overline{w}_B N}{\overline{w}_S - \overline{w}_B} \\ &= \sum_{i=1}^{N} \left(\frac{w(x_i) - \overline{w}_B}{\overline{w}_S - \overline{w}_B} \right) \end{aligned}$$

and

$$\begin{aligned} N_B &= \frac{N_w - \overline{w}_S N}{\overline{w}_B - \overline{w}_S} \\ &= \sum_{i=1}^{N} \left(\frac{w(x_i) - \overline{w}_S}{\overline{w}_B - \overline{w}_S} \right) \end{aligned}$$

with errors given by

$$\sigma_S = \left[\sum_{i=1}^{N} \left(\frac{w(x_i) - \overline{w}_B}{\overline{w}_S - \overline{w}_B} \right)^2 \right]^{1/2}$$

and

$$\sigma_B = \left[\sum_{i=1}^{N} \left(\frac{w(x_i) - \overline{w}_S}{\overline{w}_B - \overline{w}_S} \right)^2 \right]^{1/2}$$

If the background distribution is $B(x)$, this is

$$w(x) = \frac{N_S S(x)}{N_S S(x) + N_B B(x)}.$$

It can be shown that this is the best possible weight function, the results obtained using it being as good as those obtained using the maximum likelihood technique. The mean value of the weight function over the signal x distribution is

$$\overline{w}_S = \int_{-\infty}^{\infty} w(x) S(x)\, dx$$

and similarly

$$\overline{w}_B = \int_{-\infty}^{\infty} w(x) B(x)\, dx.$$

After weighting all of the N events in the sample according to their x values, the sum of the weightings is

$$N_w = \overline{w}_S N_S + \overline{w}_B N_B$$

and obviously

$$N = N_S + N_B.$$

These equations may be solved for the required N_S and N_B the results being

$$\begin{aligned} N_S &= \frac{N_w - \overline{w}_B N}{\overline{w}_S - \overline{w}_B} \\ &= \sum_{i=1}^{N} \left(\frac{w(x_i) - \overline{w}_B}{\overline{w}_S - \overline{w}_B} \right) \end{aligned}$$

and

$$\begin{aligned} N_B &= \frac{N_w - \overline{w}_S N}{\overline{w}_B - \overline{w}_S} \\ &= \sum_{i=1}^{N} \left(\frac{w(x_i) - \overline{w}_S}{\overline{w}_B - \overline{w}_S} \right) \end{aligned}$$

with errors given by

$$\sigma_S = \left[\sum_{i=1}^{N} \left(\frac{w(x_i) - \overline{w}_B}{\overline{w}_S - \overline{w}_B} \right)^2 \right]^{1/2}$$

and

$$\sigma_B = \left[\sum_{i=1}^{N} \left(\frac{w(x_i) - \overline{w}_S}{\overline{w}_B - \overline{w}_S} \right)^2 \right]^{1/2}$$

respectively.

It may be objected that it was necessary to know the relative numbers of signal and background events in order to be able to find the weight function, and hence that the above argument is circular. It is true that the optimum weight function can only be defined if N_S and N_B are known, but the above method gives correct answers for N_S and N_B regardless of the input values and the precision decreases only slowly as the accuracy of the input estimates worsen. The process can be iterated if the values of N_S and N_B calculated as above differ wildly from the input estimates.

Method (c), that of maximum likelihood, is a well known statistical technique. It can be shown to be efficient, that is it gives the most accurate results possible using the information available, and unbiassed, that is it gives asymptotically the correct results (Wetherill, 1981). To illustrate its application, consider the problem above, the maximum likelihood solution of which proceeds as follows. Let

$$l_i = N_S S(x_i) + N_B B(x_i).$$

This is simply the probability density function of x evaluated for the i^{th} event. The likelihood function is then defined to be

$$\mathcal{L} = \prod_{i=1}^{N} l_i$$

its value represents the likelihood of the occurence of N events with $x = x_1 \ldots x_N$ for the given values of N_S and N_B. The most likely value of these parameters may be found by maximization of the likelihood function by varying N_S and N_B. Equivalently and often more conveniently, the logarithm of the likelihood function

$$\begin{aligned} L &= \ln(\mathcal{L}) \\ &= \sum_{i=1}^{N} \ln(l_i) \end{aligned}$$

may be maximised. That is the equations

$$\frac{\partial L}{\partial N_S} = 0$$

$$\Rightarrow \sum_{i=1}^{N} \frac{S(x_i)}{N_S S(x_i) + N_B(x_i)} = 0$$

and

$$\frac{\partial L}{\partial N_B} = 0$$

$$\Rightarrow \sum_{i=1}^{N} \frac{B(x_i)}{N_S S(x_i) + N_B(x_i)} = 0$$

must be simultaneously solved for N_S and N_B.

The errors of the determination are obviously dependent on the sharpness of the peak in likelihood space at which the solution values of N_S and N_B occur. Mathematically this is described by the values of the second derivatives of L at this point. A more detailed treatment shows that the errors may be obtained from the diagonal components of the inverse Hessian matrix. The Hessian matrix **H** is in fact the covariance matrix and is defined, as expected from the above, in terms of the second derivatives of L.

$$\mathbf{H} = \begin{pmatrix} -\mathrm{E}\left(\frac{\partial^2 L}{\partial N_S^2}\right) & -\mathrm{E}\left(\frac{\partial^2 L}{\partial N_S \partial N_B}\right) \\ -\mathrm{E}\left(\frac{\partial^2 L}{\partial N_B \partial N_S}\right) & -\mathrm{E}\left(\frac{\partial^2 L}{\partial N_B^2}\right) \end{pmatrix}.$$

The expectation value is calculated, as previously defined, with N_S and N_B taking their solution values. Using

$$\frac{\partial^2 L}{\partial N_S \partial N_B} = \frac{\partial^2 L}{\partial N_B \partial N_S}$$

and inverting the Hessian matrix the errors are

$$\sigma_S = \left[\frac{H_{22}}{H_{11}H_{22} - H_{12}^2}\right]^{1/2}$$

and

$$\sigma_B = \left[\frac{H_{11}}{H_{11}H_{22} - H_{12}^2}\right]^{1/2}$$

the H_{ij} being the components of the Hessian matrix. If the cross terms are small these errors reduce to

$$\sigma_S = \frac{1}{\sqrt{H_{11}}}$$

and

$$\sigma_B = \frac{1}{\sqrt{H_{22}}}.$$

Under very general conditions, the likelihood function is Gaussian in form. In this case the logarithm of the likelihood function is a paraboloid and its second derivatives are all constant, therefore

$$\mathrm{E}\left(\frac{\partial^2 L}{\partial N_S^2}\right) = \frac{\partial^2 L}{\partial N_S^2}.$$

Indeed, where

$$\mathrm{E}\left(\frac{\partial^2 L}{\partial N_S^2}\right) \neq \frac{\partial^2 L}{\partial N_S^2}$$

it is preferable to use the latter (Wetherill, 1981).

As described above the methods of weights and maximum likelihood are equivalent. They could both be used to determine, say, the number of events containing electrons from b and c quark decays in a sample of inclusive electron events of known purity. Hence the number of events in which the quarks were produced in the forward and backward b and c directions could be determined, from which the b and c asymmetries could be calculated. There is however a better method of obtaining the asymmetry from the measurements of the quark directions. This avoids the loss of information arising as a result of the forward backward binning and also removes the need to apply acceptance corrections.

Chapter 7

Electroweak Asymmetry Measurement Errors and Acceptance Corrections

Assuming that the methods of the previous chapter allow the identification of c and b events and the prompt electrons in those events and that therefrom the production angles θ of the c and b quarks can be obtained, the next problem is that of obtaining the asymmetries from those measurements.

At a given energy the probability density function of the variable $x = \cos\theta$ is expected in the standard model, for each quark flavour or lepton, to be

$$\rho(x) = \frac{3}{8}(1 + x^2) + Ax,$$

A being dependent on the whether the particle is a lepton or a quark and if the latter on its flavour, as given in chapter two. Suppose the experimental data consist of N measurements of the angle θ. How can A best be obtained from these data?

The most obvious technique is that suggested in the previous chapter, namely to count the numbers of forward and backward events, N_F and N_B respectively, and to form

$$A = \frac{N_F - N_B}{N}.$$

The error in such a determination may be found by using the binomial nature of the forward backward distribution. Let the probability of obtaining a forward event be p and that of obtaining a backward event $q = 1 - p$. Then

$$\begin{aligned} A &= \frac{p - q}{p + q} \\ &= 2p - 1 \\ \Rightarrow p &= \frac{1 + A}{2} \\ q &= \frac{1 - A}{2}. \end{aligned}$$

The error of the asymmetry measurement is, from the properties of the binomial distribution,

$$\begin{aligned}\sigma_A &= 2\sigma_p \\ &= 2\sqrt{\frac{pq}{N}} \\ &= \sqrt{\frac{1-A^2}{N}}.\end{aligned}$$

This result is for a perfect experiment, that is one in which the acceptance is one over the full angular range. In fact for $|x|$ large, that is near the beampipe, the acceptance is bound to decrease for any real experiment. Suppose the detector has 100% acceptance for $|x| < l$ and zero acceptance outside this range. Using the above technique, the measured asymmetry is

$$\begin{aligned}A' &= \frac{\int_0^l \rho(x)\,dx - \int_{-l}^0 \rho(x)\,dx}{\int_{-l}^l \rho(x)\,dx} \\ &= kA\end{aligned}$$

where $k = 4l/(3+l^2)$. A is then determined from A' by multiplying by the correction factor $1/k$. The error

$$\begin{aligned}\sigma_{A'} &= \sqrt{\frac{1-A'^2}{N}} \\ &= \sqrt{\frac{1-k^2A^2}{N}} \\ &> \sigma_A.\end{aligned}$$

The trivial increase in error due to the smaller data sample collected from an experiment with less than perfect acceptance has been removed; the results are for a sample of N observed events in each case.

The above illustrates the importance of good acceptance at large angles for the accurate measurement of electroweak asymmetries, but is still not a good model of a real experiment's acceptance.

For the JADE detector, due to its symmetry in the polar angle which has been extensively checked (Bartel, 1982 and 1984a), the acceptance may be represented

by a function $E(x)$, symmetric in x, which falls from a maximum at $x = 0$ as $|x|$ increases. The asymmetry measured using the counting technique above is thus

$$A' = \frac{\int_0^1 E(x)\rho(x)\,dx - \int_{-1}^0 E(x)\rho(x)\,dx}{\int_{-1}^1 E(x)\rho(x)\,dx}.$$

Using the symmetry $E(x) = E(-x)$ the factor k relating the measured and actual asymmetries becomes

$$k = \frac{8\int_0^1 xE(x)\,dx}{3\int_0^1 (1+x^2)E(x)\,dx}.$$

The problem of determing the k factor and hence correcting for acceptance effects may be solved by the use of the Monte-Carlo. However, for distributions of the form above a neater technique exists.

Consider the likelihood function

$$\mathcal{L} = \prod_{i=1}^{N} l_i$$

where

$$\begin{aligned} l_i &= E(x_i)\rho(x_i) \\ &= E(x_i)\left[\frac{3}{8}(1+x_i^2) + Ax_i\right]. \end{aligned}$$

The maximum likelihood estimate for A is then found by maximising the logarithm of this function

$$L = \sum_{i=1}^{N} \ln(l_i)$$

that is by solving

$$\frac{\partial}{\partial A}\sum_{i=1}^{N}\left\{\ln\left[E(x_i)\right] + \ln\left[\frac{3}{8}(1+x_i^2) + Ax_i\right]\right\} = 0.$$

As the acceptance function is not dependent on the asymmetry

$$\begin{aligned} \frac{\partial}{\partial A}\ln\left|E(x)\right| &= \frac{1}{E(x)}\frac{\partial}{\partial A}E(x) \\ &= 0 \end{aligned}$$

by a function $E(x)$, symmetric in x, which falls from a maximum at $x = 0$ as $|x|$ increases. The asymmetry measured using the counting technique above is thus

$$A' = \frac{\int_0^1 E(x)\rho(x)\,dx - \int_{-1}^0 E(x)\rho(x)\,dx}{\int_{-1}^1 E(x)\rho(x)\,dx}.$$

Using the symmetry $E(x) = E(-x)$ the factor k relating the measured and actual asymmetries becomes

$$k = \frac{8\int_0^1 xE(x)\,dx}{3\int_0^1 (1+x^2)E(x)\,dx}.$$

The problem of determing the k factor and hence correcting for acceptance effects may be solved by the use of the Monte-Carlo. However, for distributions of the form above a neater technique exists.

Consider the likelihood function

$$\mathcal{L} = \prod_{i=1}^{N} l_i$$

where

$$\begin{aligned} l_i &= E(x_i)\rho(x_i) \\ &= E(x_i)\left[\frac{3}{8}(1+x_i^2) + Ax_i\right]. \end{aligned}$$

The maximum likelihood estimate for A is then found by maximising the logarithm of this function

$$L = \sum_{i=1}^{N} \ln(l_i)$$

that is by solving

$$\frac{\partial}{\partial A}\sum_{i=1}^{N}\left\{\ln\left[E(x_i)\right] + \ln\left[\frac{3}{8}(1+x_i^2) + Ax_i\right]\right\} = 0.$$

As the acceptance function is not dependent on the asymmetry

$$\begin{aligned} \frac{\partial}{\partial A}\ln\left[E(x)\right] &= \frac{1}{E(x)}\frac{\partial}{\partial A}E(x) \\ &= 0 \end{aligned}$$

and the above becomes

$$\sum_{i=1}^{N} \left\{ \frac{x_i}{\frac{3}{8}(1+x_i^2) + Ax_i} \right\} = 0$$

or

$$\sum_{i=1}^{N} \frac{x_i}{\rho(x_i)} = 0$$

which is independent of the acceptance function.

Unfortunately this equation has no analytical solution, but in practice this is no handicap as many highly efficient algorithms are available for the numerical solution of just this kind of problem. Alternatively the value of $\partial L/\partial A$ may be calculated for several values of A in the allowed range $-3/4 < A < 3/4$ and the points $(A, \partial L/\partial A)$ graphed. The intercept with zero may then be found by interpolation. The allowed range of A is smaller than the $-1 < A < 1$ that might be expected due to the assumption that the x probability density function is $\rho(x)$. This must be positive for all x which constrains the allowed values of A as above. For the expected Gaussian form of the likelihood function, the first derivative of its logarithm is a straight line and thus the interpolation is easily performed.

The error of the estimate of A is

$$\sigma_A = \left[-\mathrm{E}\left(\frac{\partial^2 L}{\partial A^2} \right) \right]^{-1/2}$$

where

$$\frac{\partial^2 L}{\partial A^2} = \sum_{i=1}^{N} - \left(\frac{x}{\rho(x)} \right)^2 .$$

In order to compare the precision of this method with the counting technique the following must be evaluated

$$\begin{aligned} \mathrm{E}\left(\frac{\partial^2 L}{\partial A^2} \right) &= N \int_{-1}^{1} \frac{-x^2}{\rho^2(x)} E(x)\rho(x)\, dx \\ &= N \int_{-1}^{1} \frac{-x^2}{\rho(x)} E(x)\, dx. \end{aligned}$$

For $E(x) \equiv 1$ this integral may be done and for $A < 0.7$ the result may be accurately parameterised, giving (Marshall, 1984b)

$$\sigma_A = \sqrt{\frac{1}{N}\left(\frac{7}{8} - \frac{4}{3}A^2\right)}.$$

Comparing this with the previous result for the counting technique with 100% acceptance, for the expected b asymmetry at $35\,GeV$ the statistical errors obtained using this method are about 10% smaller than those obtained using the counting technique. In addition in the case of less than full acceptance, systematic errors are smaller as no acceptance corrections are necessary.

For the case of a series of N discrete measurements of x, provided N is reasonably large,

$$\mathrm{E}\left(\frac{\partial^2 L}{\partial A^2}\right) = \frac{\partial^2 L}{\partial A^2}$$

and hence

$$\sigma_A = \left[\sum_{i=1}^{N}\left(\frac{x_i}{\rho(x_i)}\right)^2\right]^{-1/2}.$$

Chapter 8

THE c AND b ASYMMETRIES

The information required in order to perform a maximum likelihood fit to extract the c and b asymmetries, using the ideas that have been discussed, was extracted from the data as follows.

Multihadronic events observed at centre of mass energies in the range 33 to 37 GeV, with a mean energy of 34.9 GeV, were searched for electron tracks using the previously described method. All tracks with $P_e > 0.1$ were considered as potential electrons. The event axes of the events containing these tracks were calculated using the sphericity analysis. The momenta of the potential electrons transverse to this axis, p_T, were then calculated, as were the transverse masses, M, of the events.

In order to determine the quark direction, the sphericity axis $\hat{\mathbf{q}}_3$ was given a sense such that

$$\mathbf{p}_e \cdot \hat{\mathbf{q}}_3 = q_e$$

where $\mathbf{p}_e$ was the electron momentum vector and q_e its charge. The $\hat{\mathbf{q}}_3$ vector then represents the direction of a positively charged quark, if the track used to give a sense to the direction was that of an electron from the decay of a heavy quark. The required information, the cosine of the polar angle of production of the quark, is then the z component of the $\hat{\mathbf{q}}_3$ vector. As the JADE coordinate system has the z axis in the direction of the positrons, not the electrons, the 3rd component of $\hat{\mathbf{q}}_3$ is $-1 \times \cos\theta$ in the coordinate system used in the discussion of the asymmetry. Thus the scheme for giving a sense to $\hat{\mathbf{q}}_3$ outlined above gives $\cos\theta$ as for negative quarks in the JADE coordinate system.

For each potential electron track P_e, p_T, M and $\cos\theta$ were stored on disc,

making the information readily accessible to the routines used for calculating the likelihood function.

In order to construct the probability density function describing the distribution of the variables above, from which the likelihood function may be calculated, it is necessary to consider the distributions of the variables above for the various possible sources of potential electron tracks.

The first class of these are genuine electron tracks, the probability of this being indicated by the value of P_e for each track. These consist of both the prompt electrons of interest and electrons from various background sources.

The prompt electrons are produced primarily through the decays illustrated in figure 8.1 and 8.2. The charge of electrons so produced correctly tags that of the parent quarks. They are labelled *be* and *ce* for those produced in *b* and *c* flavoured events respectively. In *b* events a small number of electrons came from the decay illustrated in figure 8.3 and some from the decay illustrated in figure 8.4 and similar processes involving other intermediary particles. The first of these production mechanisms results in electrons whose charge has opposite sign to that of the parent quark. These must be distinguished from those arising from the primary decay and are labelled *bce*. The production mechanism in figure 8.4 gives rise to electrons whose charge has the same sign as that of the parent quark and these are considered under the label *be* together with those from the dominant semi-electronic *b* decay.

The p_T distributions of the electrons from all these sources are shown in figures 8.5, 8.6 and 8.7.

The angular distributions of the event axes whose sense was determined using the *be* and *ce* tracks is that of the parent quark. For the *bce* tracks it is that

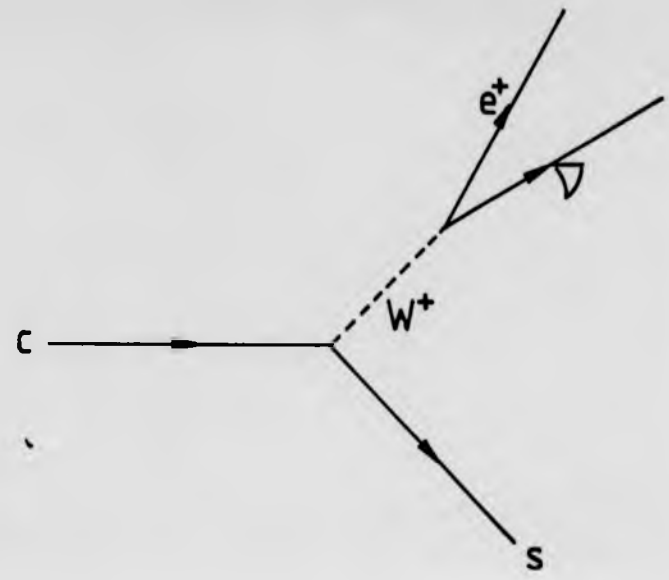

Figure 8.1. Electronic decay of a c quark.

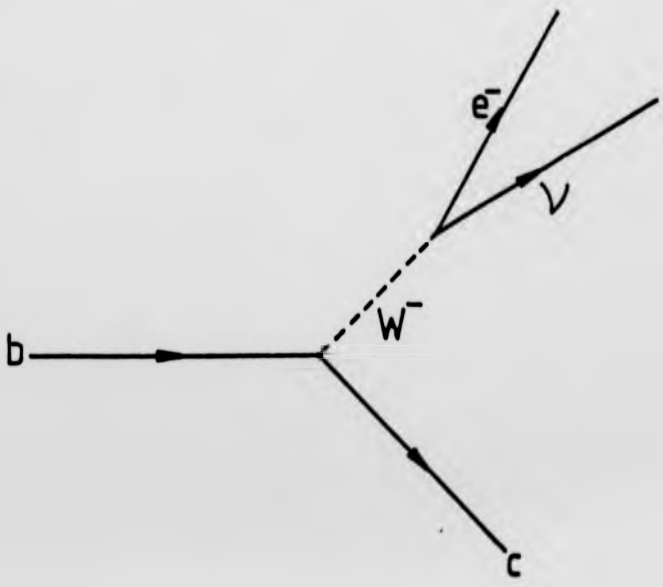

Figure 8.2. Electronic decay of a b quark.

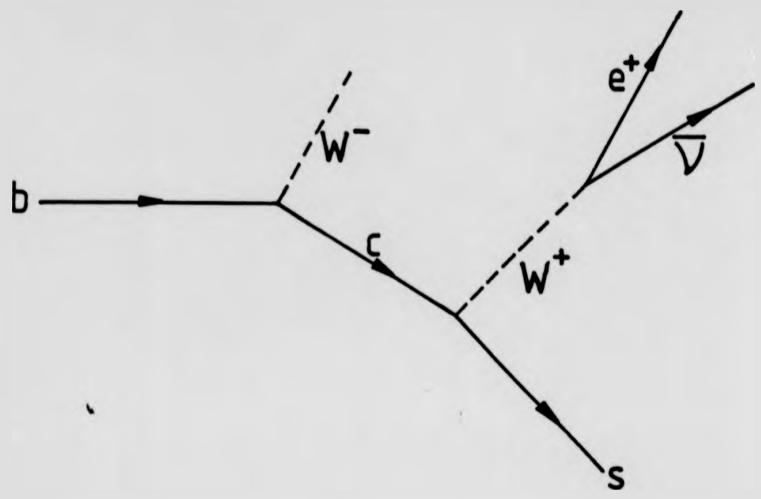

Figure 8.3. The cascade decay $b \to c \to e^+$.

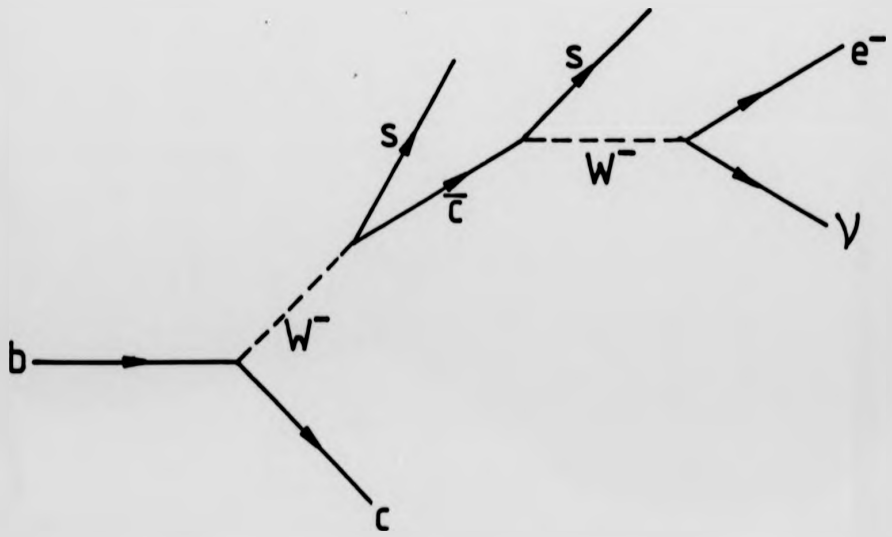

Figure 8.4. The cascade decay $b \to \bar{c} \to e^-$.

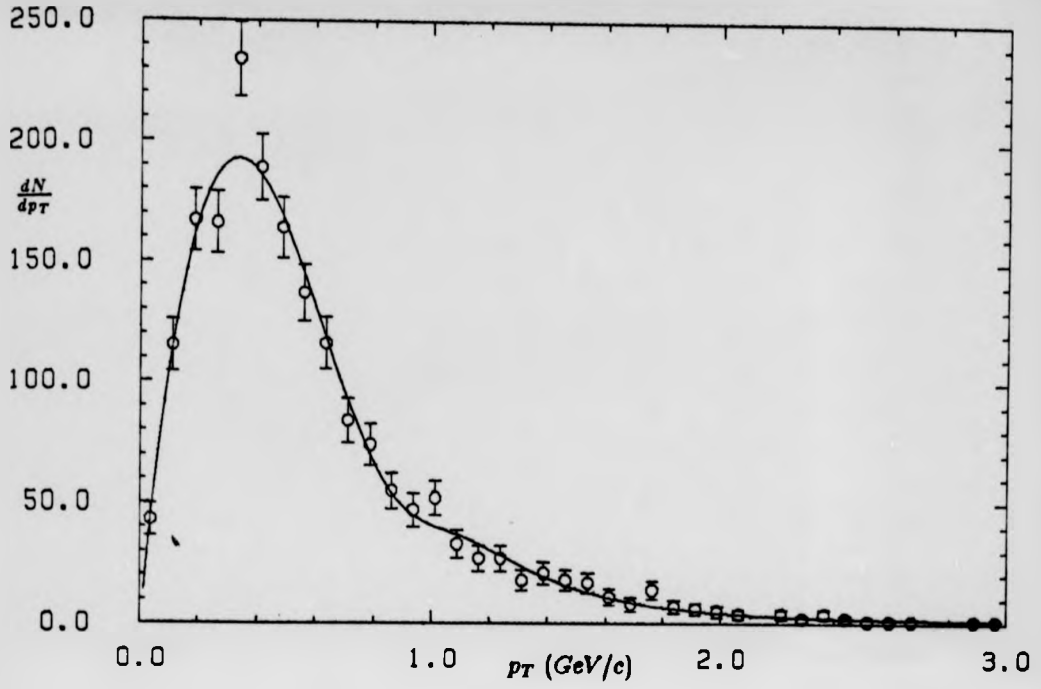

Figure 8.5. Monte-Carlo p_T spectrum for electrons from decay $c \rightarrow e$.

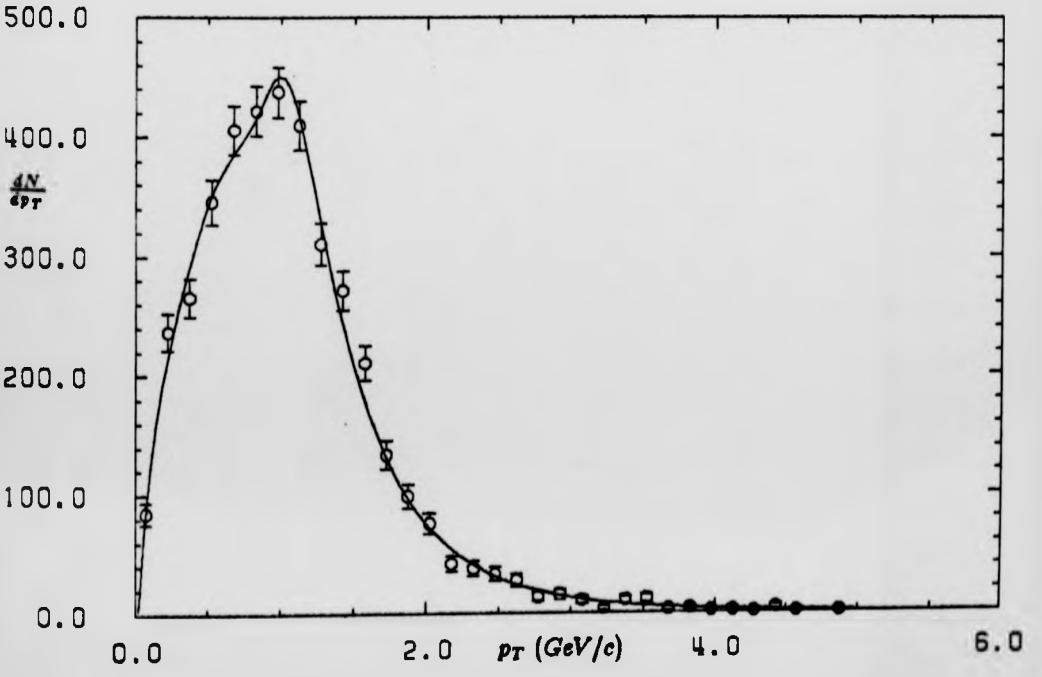

Figure 8.6. Monte-Carlo p_T spectrum for electrons from decay $b \rightarrow e$.

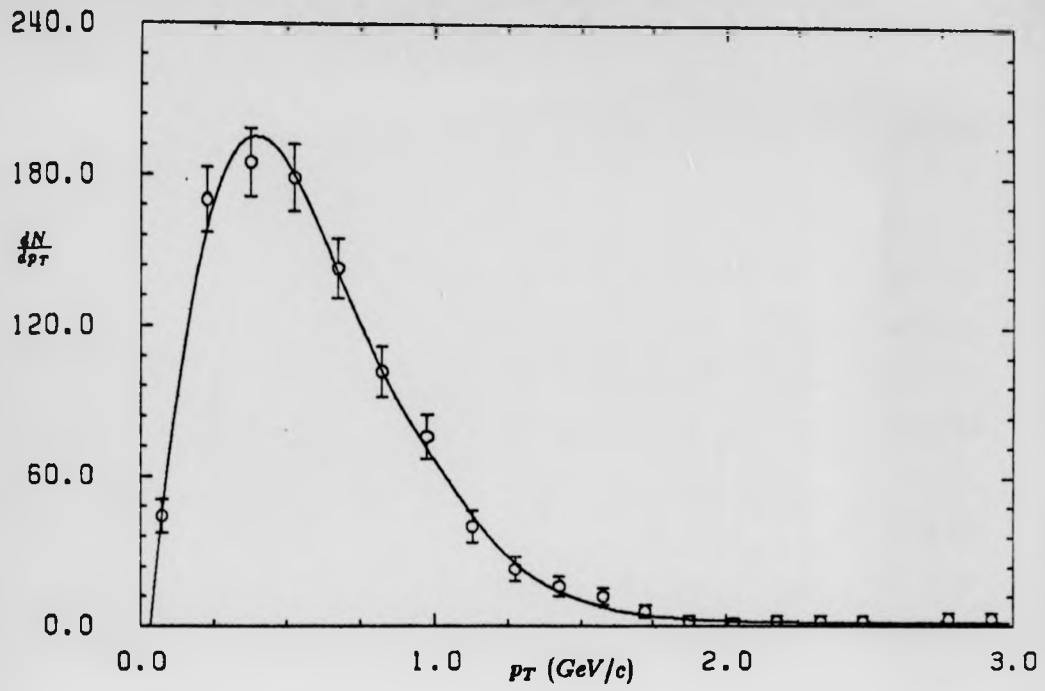

Figure 8.7. Monte-Carlo p_T spectrum for electrons from decay $b \rightarrow c \rightarrow e$.

of the b quark but with the sign of the asymmetric term reversed. One possible complication must be considered here.

The energy released in the weak decays of heavy quarks is considerable, for example an electron produced in the decay of a b quark in a B meson may acquire an energy of up to about $2.2\,GeV$. If the fragmentation occurred in such a way that the B meson received only a small amount of the available momentum and energy, then it is possible that an electron whose momentum from the decay is in the opposite direction to that of the B meson appear in the 'wrong' jet. A similar effect may occur in c events though with lower probability. This results in an incorrect tagging of the quark charge. Suppose the probability of this occurring is p, then the measured asymmetry, ignoring all problems of separation and so on, is

$$A' = (1 - p) - pA$$
$$= (1 - 2p)A$$

as the events with wrong jet electrons appear to have opposite asymmetry to those that are correctly tagged.

The probability of the occurence of such wrong jet electrons was investigated using the Monte-Carlo. For b events it was found to be about 2% and for c events less than 0.5%. These values are dependent on the form of the fragmentation function, but even the assumption of a flat fragmentation function increased the b value to only 6%. The p_T of the electrons involved was always small and therefore their effect in the maximum likelihood fit was negligible. Thus no correction was made for the 'wrong jet' electron effect.

The remaining electrons are non-prompt, that is not from heavy quark decays. Monte-Carlo studies indicate that 95% of these are the result of photon conversions. The photons come primarily from the decay of neutral pions produced in the fragmentation, $\pi^0 \rightarrow \gamma\gamma$. A $5\,GeV$ photon produced close to the

interaction point and travelling normal to the beam axis has a probability of 15% of undergoing conversion in the beampipe, pressure vessel or Jet chamber, a figure resulting from the 0.16 radiation lengths of material through which it must pass. Most of the rest of the background electron tracks come from the Dalitz decay $\pi^0 \rightarrow e^+e^-\gamma$. Less than one per cent come from other sources. The p_T distributions of these background electrons were found to be slightly dependent on the flavour of the event in which they occurred and thus it is convenient to distinguish between be', ce' and re', background electrons in b, c and r events respectively. The p_T spectrum of background electrons in d, u and s events is illustrated in figure 8.8. The angular distribution of event axes whose sense was determined using these tracks is symmetric for each flavour, electrons produced from photon conversions having no memory of the charge of the parent quark.

The second type of background is that due to non-electron tracks. The probability that a track is not that of an electron being given by $P_r = 1 - P_e$. These, primarily charged pion, tracks were also found to have p_T spectra somewhat dependent on the flavour of the event in which they occurred and for b, c and r flavoured events were labelled br, cr and rr respectively. The p_T spectrum of non-electron tracks in d, u and s events is illustrated in figure 8.9.

The angular distribution of the axes whose direction was determined from these tracks was not completely symmetric for a given flavour. Some memory of the charge of the parent quark was retained. The possibility of using this to determine the quark charge has been investigated by Wyatt (1983). Monte-Carlo studies indicated that the probability of a randomly selected charged particle, not including electrons, having the same charge as the parent quark of the jet in which it occurred rose linearly from 0.55 for tracks with very small p_T to a maximum of 0.60 for tracks with a p_T of around $3\,GeV/c$. This is only a slight increase over the probability of a half obtained if the particles carry no information concerning

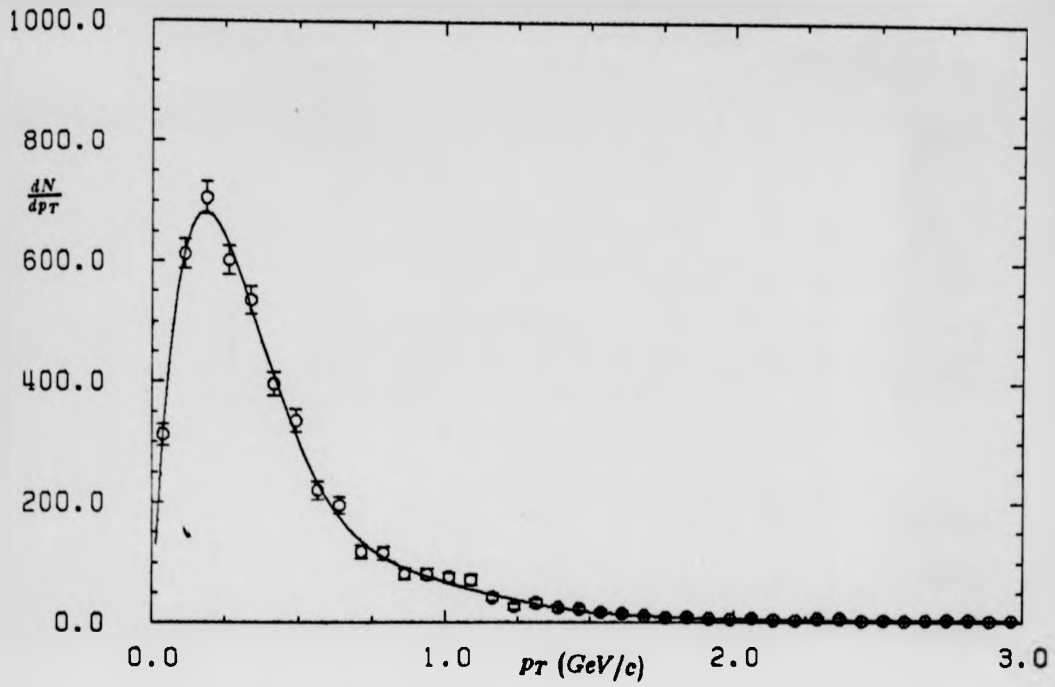

Figure 8.8. The Monte-Carlo background electron p_T spectrum for d, u and s flavoured events.

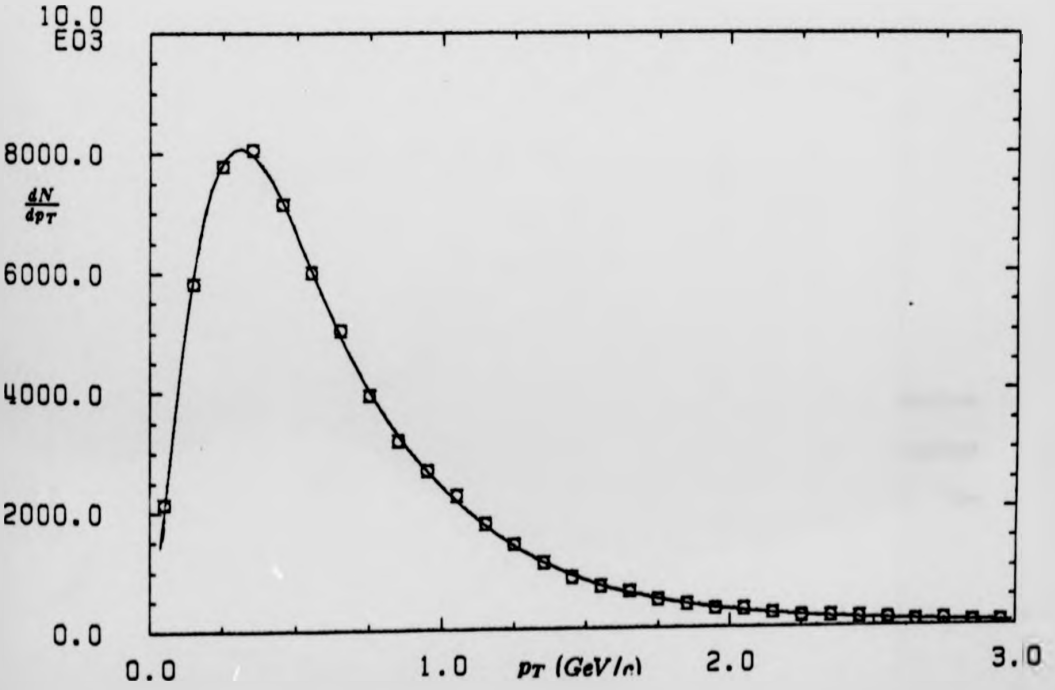

Figure 8.9. The Monte-Carlo non-electron p_T spectrum for d, u and s flavoured events.

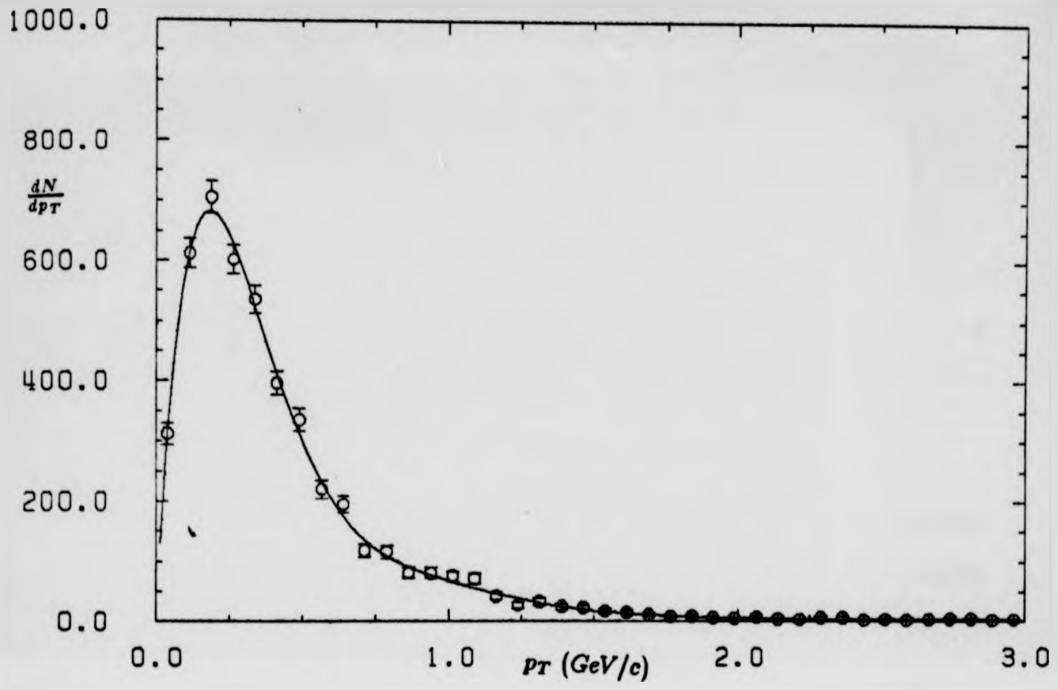

Figure 8.8. The Monte-Carlo background electron p_T spectrum for d, u and s flavoured events.

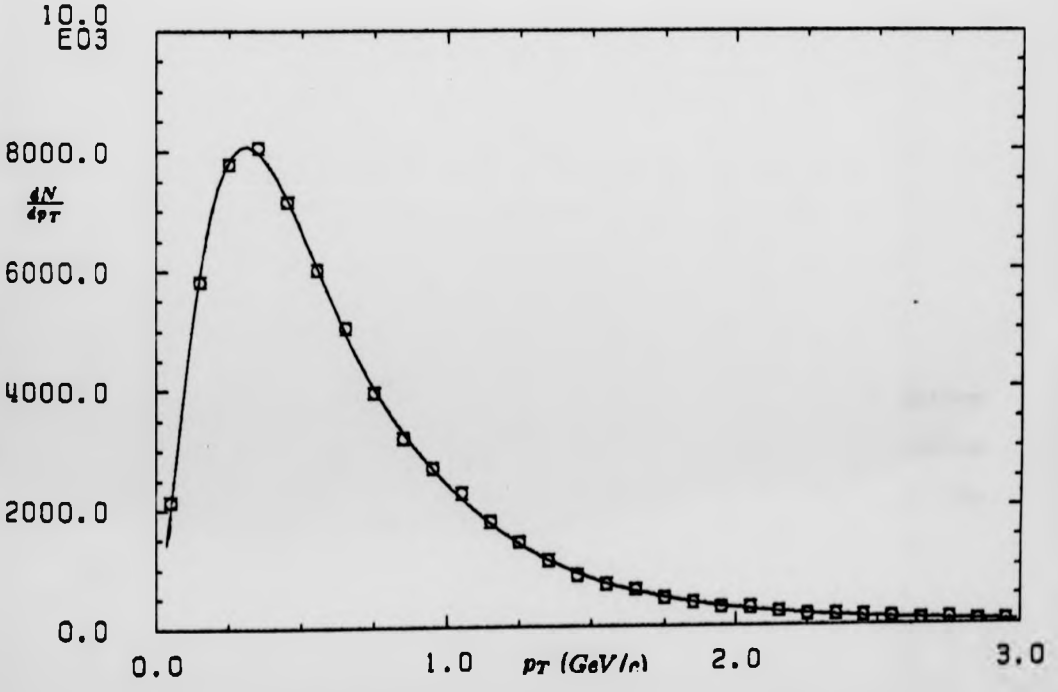

Figure 8.9. The Monte-Carlo non-electron p_T spectrum for d, u and s flavoured events.

the charge of the parent quark. Using the same argument as for the wrong jet electrons, the asymmetry measured using this effect would at most be a fifth of the genuine asymmetry. Nonetheless, attempts were made to include this information in the likelihood function. The result was that the function behaved badly, no maximum existing. This was probably due to poor understanding of the fine detail of the fragmentation process making the figures for the probabilities given above incorrect.

The remaining distributions of importance are those of the transverse mass. These, illustrated in figures 8.10, 8.11 and 8.12, are primarily dependent on the event flavours, although there is also a slight decrease in the mean event mass for events containing a prompt electron.

Following the discussion above the probability density function required can now be written down. The electronic part is

$$\begin{aligned} l^e(M,p_T,\cos\theta) = N_b^e \Big\{ & r_{be}\rho_{be}(M,p_T)\left[S(\cos\theta) + A_b\cos\theta\right] \\ & + r_{bce}\rho_{bce}(M,p_T)\left[S(\cos\theta) - A_b\cos\theta\right] \\ & + r_{be'}\rho_{be'}(M,p_T)S(\cos\theta)\Big\} + \\ N_c^e \Big\{ & r_{ce}\rho_{ce}(M,p_T)\left[S(\cos\theta) - A_c\cos\theta\right] \\ & + r_{ce'}\rho_{ce'}(M,p_T)S(\cos\theta)\Big\} + \\ & N_\tau^e\rho_{\tau e'}(M,p_T)S(\cos\theta). \end{aligned}$$

In this expression the N^e are the relative frequencies of occurrence of an electron track in the event flavour concerned, the relative frequencies with which the various classes of electrons occur within that flavour being indicated by the r's. The function

$$S(\cos\theta) = \frac{3}{8}(1+\cos^2\theta)$$

is the symmetric part of the angular distribution.

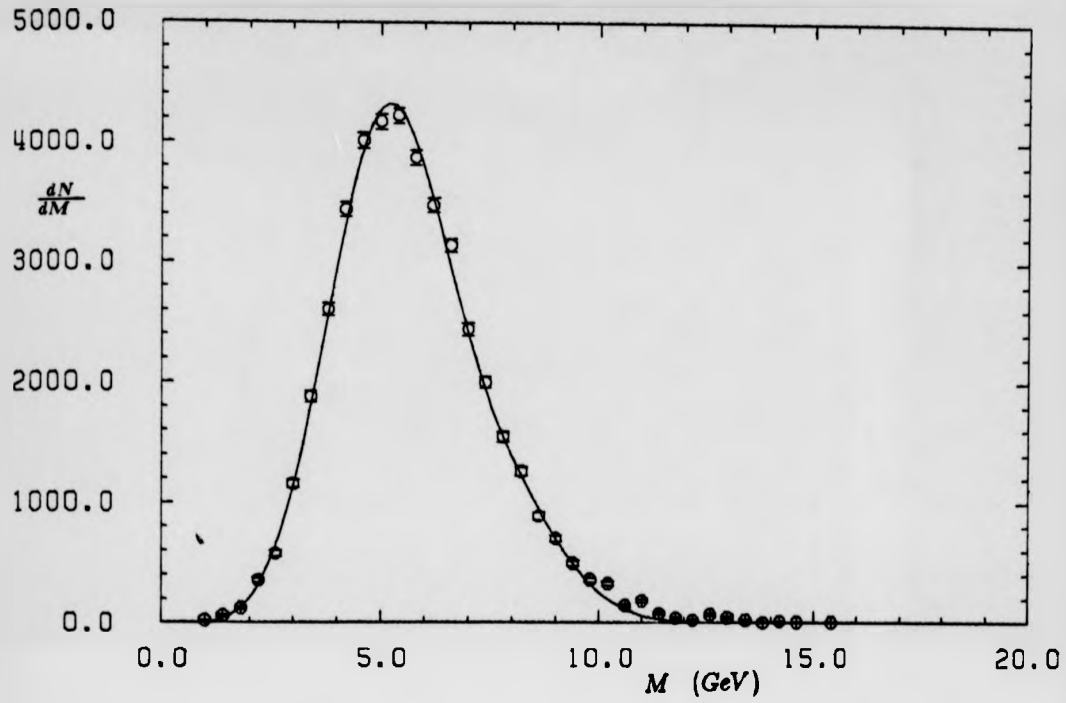

Figure 8.10. The Monte-Carlo M spectrum for d, u and s flavoured events.

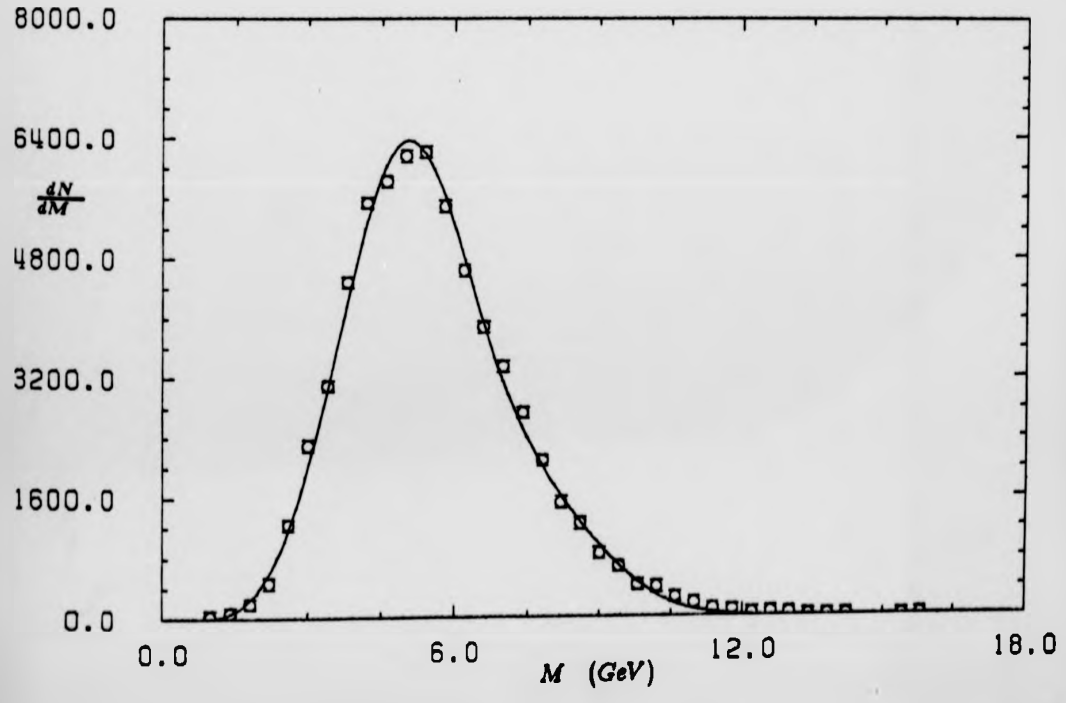

Figure 8.11. The Monte-Carlo M spectrum for c flavoured events.

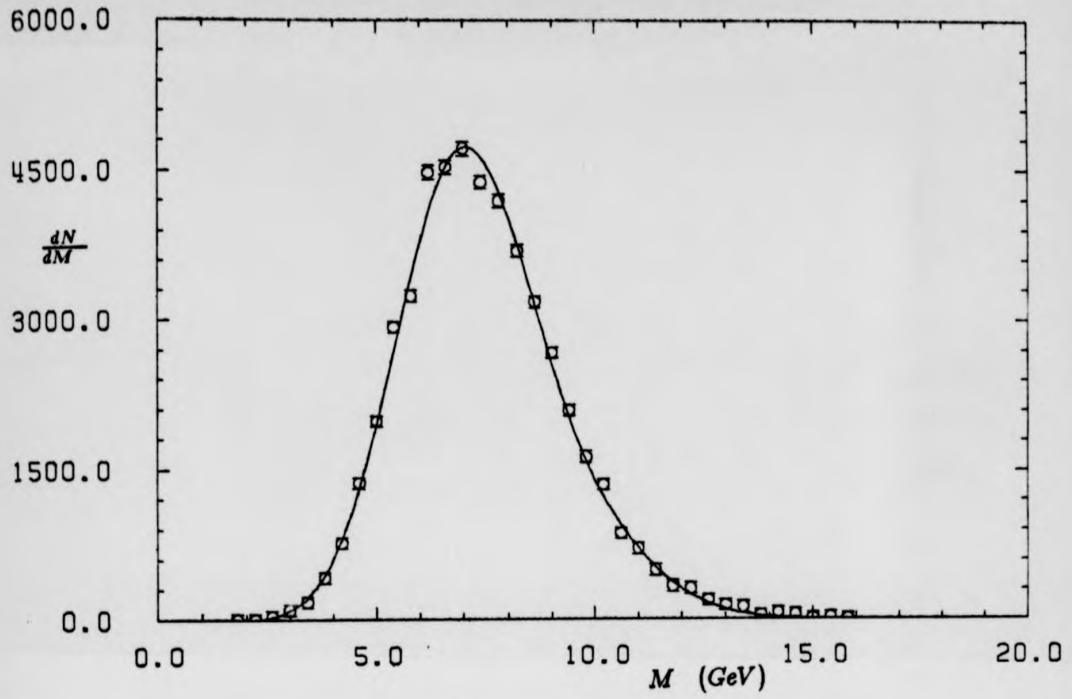

Figure 8.12. The Monte-Carlo M spectrum for b flavoured events.

Similarly the non-electron probability distribution function is

$$l^r(M, p_T, \cos\theta) = N_b^r \rho_{br}(M, p_T) S(\cos\theta) + N_c^r \rho_{cr}(M, p_T) S(\cos\theta) + N_r^r \rho_{rr}(M, p_T) S(\cos\theta).$$

The values of the N and r were obtained from the Monte-Carlo. The $\rho(M, p_T)$ were represented, as previously described, using analytical functions obtained from the fits to the relevant Monte-Carlo data distributions shown in the previous figures.

Combining the above the complete probability density function is

$$l = P_e l^e + P_r l^r.$$

The likelihood function is then

$$\mathcal{L} = \prod_{i=1}^{N} l_i$$

where l_i is the probability density function evaluated using the M, p_T and $\cos\theta$ values for the i^{th} track, there being N tracks in all. Its logarithm is

$$L = \sum_{i=1}^{N} \ln l_i.$$

To obtain the maximum likelihood estimates of A_c and A_b the above was maximised with respect to the c and b asymmetries. That is the simultaneous equations

$$\frac{\partial L}{\partial A_c} = 0$$

and

$$\frac{\partial L}{\partial A_b} = 0$$

were solved. Inserting the above form for L and performing the differentiations these equations become

$$\sum_{i=1}^{N} \frac{N_c^e r_{ce} \rho_{ce} \cos\theta}{l_i} = 0$$

and

$$\sum_{i=1}^{N} \frac{N_b^e\left(r_{be}\rho_{be} - r_{bce}\rho_{bce}(M, p_T)\right)\cos\theta}{l_i} = 0.$$

The covariance matrix was formed from the quantities

$$\begin{aligned} H_{11} &= \frac{\partial^2 L}{\partial A_c^2} \\ H_{12} &= \frac{\partial^2 L}{\partial A_c \partial A_b} \\ &= \frac{\partial^2 L}{\partial A_b \partial A_c} \\ &= H_{21} \end{aligned}$$

and

$$H_{22} = \frac{\partial^2 L}{\partial A_b^2}$$

where

$$\frac{\partial^2 L}{\partial A_c^2} = \sum_{i=1}^{N} -\frac{\left[N_c^e r_{ce}\rho_{ce}\cos\theta\right]^2}{l_i^2},$$

$$\frac{\partial^2 L}{\partial A_c \partial A_b} = \sum_{i=1}^{N} -\frac{\left[N_c^e r_{ce}\rho_{ce}\cos\theta\right]\left[N_b^e\left(r_{be}\rho_{be} - r_{bce}\rho_{bce}\right)\cos\theta\right]}{l_i^2}$$

and

$$\frac{\partial^2 L}{\partial A_b^2} = \sum_{i=1}^{N} -\frac{\left[N_b^e\left(r_{be}\rho_{be} - r_{bce}\rho_{bce}(M, p_T)\right)\cos\theta\right]^2}{l_i^2}$$

with A_c and A_b taking the values at the solution point of the simultaneous equations. The error of the c asymmetry measurement is then

$$\sigma_c = \frac{H_{22}}{H_{11}H_{22} - H_{12}^2}$$

and that of the b asymmetry measurement

$$\sigma_b = \frac{H_{11}}{H_{11}H_{22} - H_{12}^2}.$$

Results.

The electron search found 7511 barrel tracks with a value of $P_e > 0.1$. The P_e, $\cos\theta$, M and p_T distributions associated with these tracks are shown in figures 8.13 to 8.16. The asymmetry of the raw $\cos\theta$ distribution is 0.0046 ± 0.0056. Figures 8.17 and 8.18 show the M distribution of the events containing tracks with $P_e > 0.8$ and the p_T distribution of those tracks. The distributions of these quantities from the Monte-Carlo are also illustrated and match the data distributions well, giving confidence that the Monte-Carlo simulation of the electron data is good.

The fitting procedure described above returned the values

$$A_c = -0.15 \pm 0.15$$

and

$$A_b = -0.24 \pm 0.16\,.$$

Systematic effects from two sources were investigated. To study the influence of the fragmentation parameters chosen the constants N and r and the $\rho(M, p_T)$ functions were recalculated using Monte-Carlo data generated with the harder parameters $\epsilon_c = 0.026$ and $\epsilon_b = 0.009$ and also with the softer parameters $\epsilon_c = 0.072$ and $\epsilon_b = 0.030$. These caused changes of about 17% and 12% in the c and b asymmetries respectively. The effects of errors in the branching ratios were simulated by varying the relevant N and r by amounts proportional to the measurement errors for these quantities given in chapter two. The resulting changes in the asymmetries were 8% and 3% respectively. Adding these figures in quadrature gives a systematic error of about ± 0.03 for both the c and b asymmetry measurements. So

$$A_c = -0.15 \pm 0.15 \pm 0.03$$

$$A_b = -0.24 \pm 0.16 \pm 0.03$$

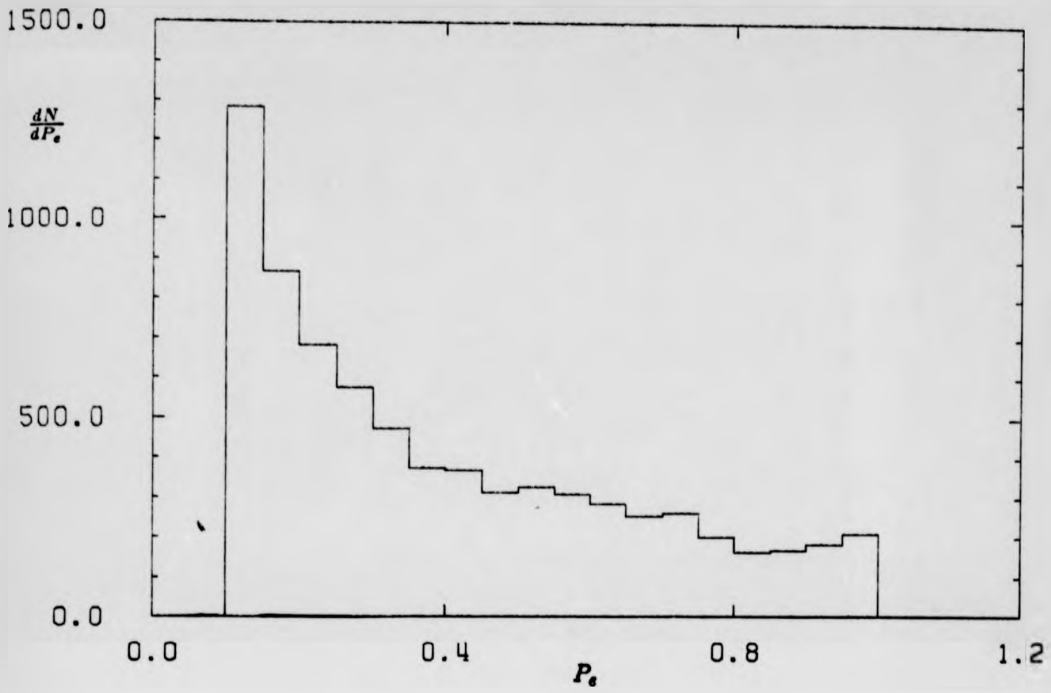

Figure 8.13. The distribution of the electron selection variable P_e.

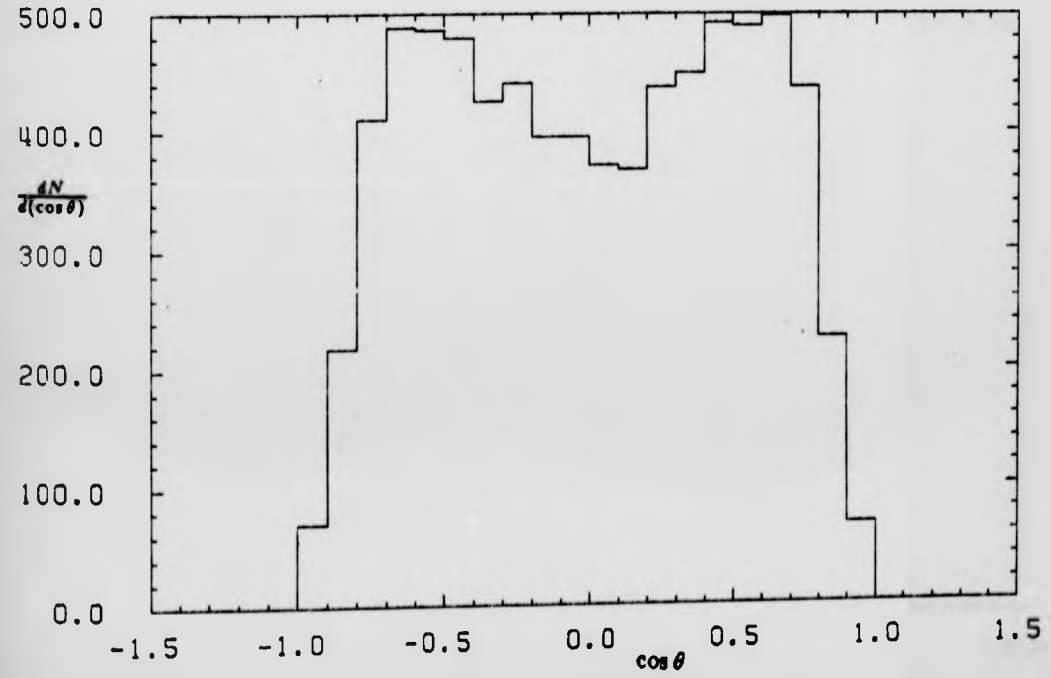

Figure 8.14. The $\cos\theta$ distribution of the electron events.

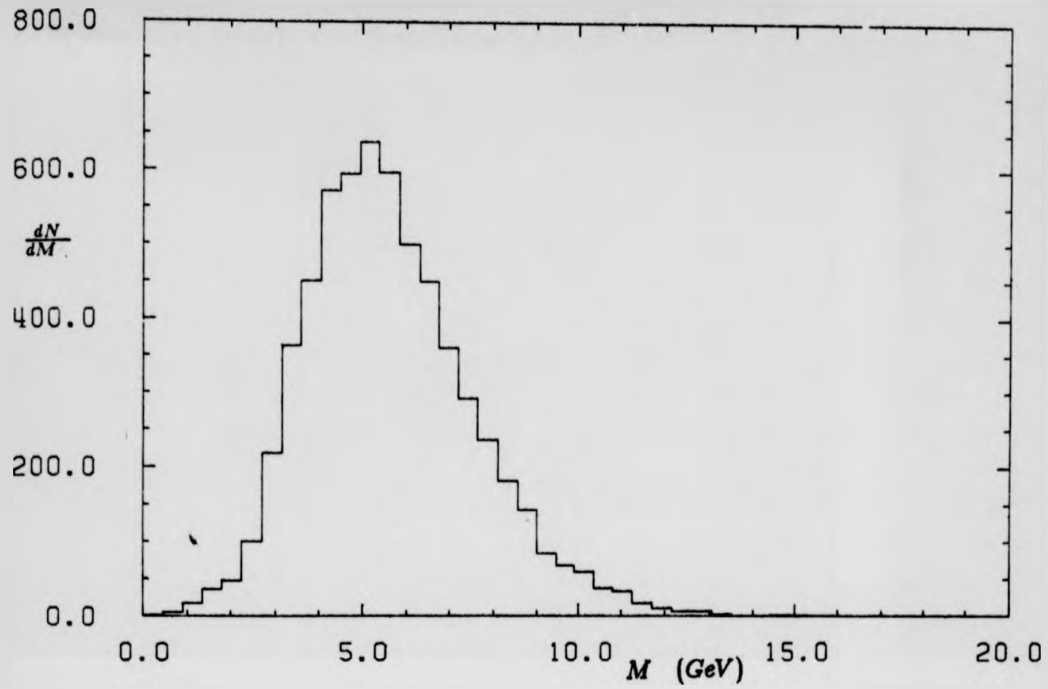

Figure 8.15. The M distribution of the events containing a track with $P_e > 0.1$.

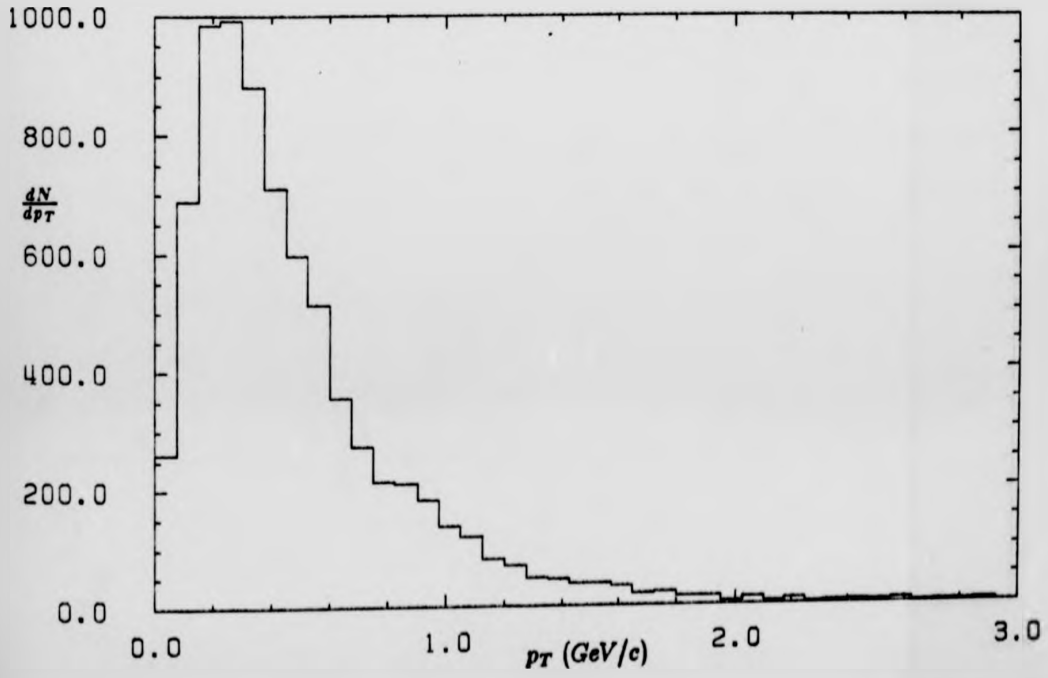

Figure 8.16. The p_T distribution of the tracks with $P_e > 0.1$.

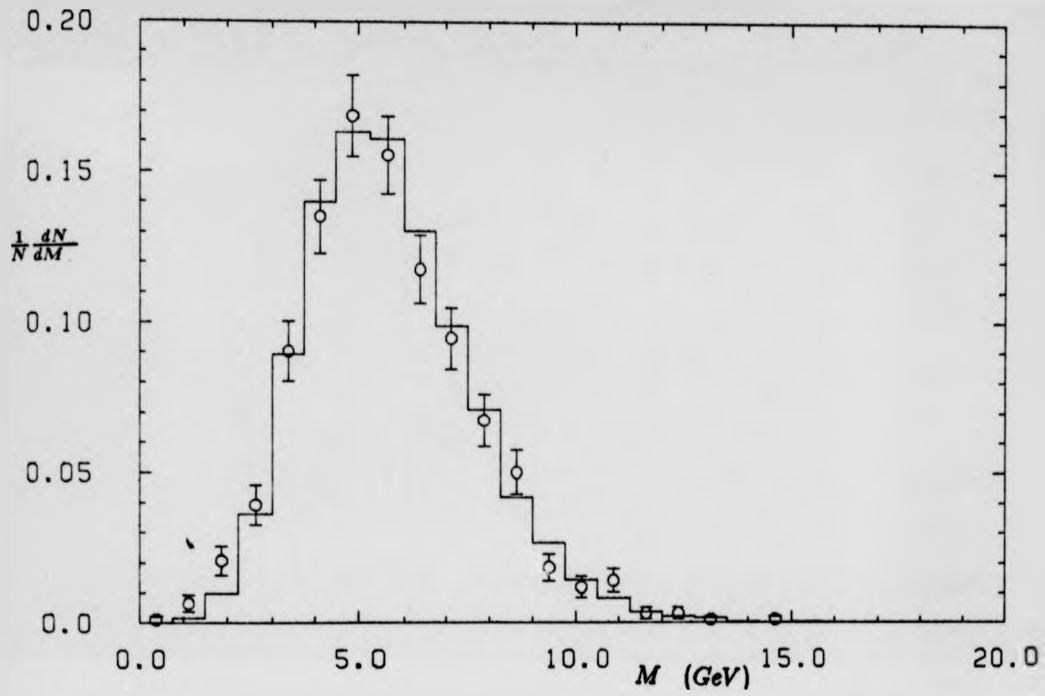

Figure 8.17. The M distribution of the events containing tracks with $P_e > 0.8$ (circles) compared with the Monte-Carlo expectations (solid line).

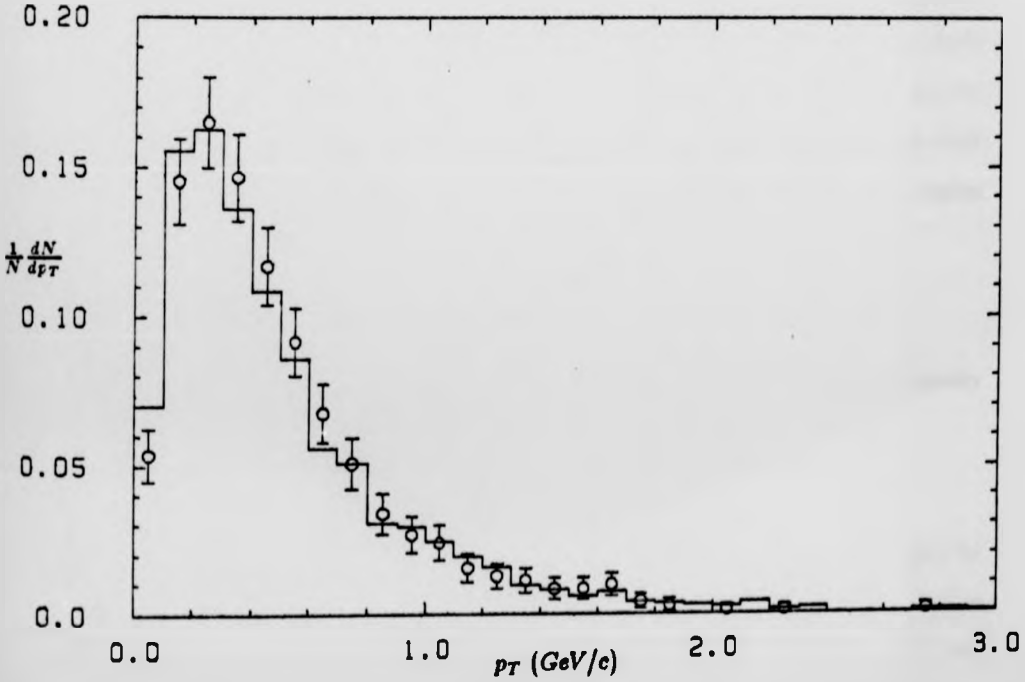

Figure 8.18. The p_T distribution of the tracks with $P_e > 0.8$ (circles) compared with the Monte-Carlo expectations (solid line).

in good agreement with the expectations of the Standard Model as obtained in the second chapter, namely

$$A_c^{(1)} = -0.13$$

and

$$A_b^{(1)} = -0.23 .$$

That the errors with which these numbers are determined are reasonable may be checked as follows. The summed probability that the tracks be due to electrons, for all the tracks used in the fit, is 2916.7. The data thus correspond to a sample of about 2900 inclusive electron events, of which, according to the Monte-Carlo, about 330 contain $c \rightarrow e$ decays and 180 $b \rightarrow e$ decays. The errors of asymmetry measurements made using pure c and b prompt lepton event samples containing these numbers of events would be 0.05 and 0.07 for A_c and A_b respectively, assuming full acceptance. The discrepancy between these numbers and those obtained is due to the effects of fitting in the presence of a background and the limited acceptance of the JADE detector. This latter effect is particularly important here as the acceptance for inclusive electron events, with the constraint that the electron track must lie within $|\cos\theta| < 0.8$ decreases rapidly as the event axis approaches the beam pipe. The acceptance is thus poor in exactly the region in which asymmetries are most strongly manifest.

The Axial Coupling Constants of the c and b Quarks.

As presented in the second chapter, in the Standard Model the asymmetry A_f is given approximately by

$$A_f = k\frac{a_e a_f}{q_f}$$

k being a numerical factor dependent on the energy. The error introduced by the approximation is small compared to the measurement errors involved and so its use is justified. Including the corrections discussed in chapter two, which are

different for the different flavours, k takes the values 0.0851 and 0.0798 for c and b quarks respectively at a centre of mass energy of $35\,GeV$. The above asymmetry measurements thus correspond to

$$\frac{a_e a_c}{q_c} = -1.8 \pm 1.8 \pm 0.4$$

and

$$\frac{a_e a_b}{q_b} = -3.0 \pm 2.0 \pm 0.4\,.$$

Using the value of a_e measured in neutrino scattering experiments, given in chapter two, the ratios of the quark axial coupling constants to their charges are

$$\frac{a_c}{q_c} = 1.7 \pm 1.7 \pm 0.4$$

and

$$\frac{a_b}{q_b} = 3.0 \pm 2.0 \pm 0.4,$$

the error of the a_e measurement being insignificant compared to the errors arising from the asymmetry measurements. Assuming the electric charges of the quarks to be $2/3$ and $-1/3$ for c and b flavours respectively, the axial coupling constants are

$$a_c = 1.2 \pm 1.2 \pm 0.2$$

and

$$a_b = -0.98 \pm 0.67 \pm 0.17\,.$$

These results are in agreement with both the Standard Model expectations of $a_c = 1$ and $a_b = -1$ and previous measurements, the results of which are given in tables 8.1 for a_c, and 8.2 for a_b.

Alternatively, assuming the axial coupling constants take the expected values, the quark charges are measured to be

$$q_c = 0.58 \pm 0.58 \pm 0.13$$

and

$$q_b = -0.34 \pm 0.23 \pm 0.06\,.$$

Table 8.1, Measurements of A_c and a_c.

Group	$\sqrt{s}(GeV)$	A_c(measured)	A_c(group's expectations)	a_c	Method
MAC	29.0	-0.05 ± 0.11	-0.03	1.6 ± 3.6	$c \rightarrow \mu$
HRS	29.0	-0.25 ± 0.18	-0.09	2.6 ± 1.9	D^*
TPC	29.0	–	–	2.0 ± 1.0	$c \rightarrow e, \mu$
TPC	29.0	–	–	1.8 ± 1.8	D^*
MARK J	34.6	-0.17 ± 0.09	-0.14	1.2 ± 0.6	$c \rightarrow \mu$
JADE	34.4	-0.27 ± 0.14	-0.14	1.9 ± 1.0	D^*
TASSO	34.4	-0.13 ± 0.10	-0.14	0.9 ± 0.7	D^*

The weighted mean of these results is $a_c = 1.36 \pm 0.36$. The errors given are statistical only, these being larger than the systematic errors in all cases.

Table 8.2, Measurements of A_b and a_b.

Group	$\sqrt{s}(GeV)$	A_b(measured)	A_b(group's expectations)	a_b	Method
MAC	29.0	-0.07 ± 0.09	-0.12	-0.6 ± 0.7	$b \rightarrow \mu$
MARK II	29.0	–	–	$-2.6^{+0.7}_{-0.6}$	$b \rightarrow e, \mu$
TPC	29.0	–	–	-1.5 ± 1.4	$b \rightarrow e, \mu$
MARK J	34.6	-0.15 ± 0.22	-0.25	-0.6 ± 0.9	$b \rightarrow \mu$
TASSO	34.4	-0.38 ± 0.28	-0.27	-1.4 ± 1.0	$b \rightarrow \mu$
JADE	34.6	-0.228 ± 0.060	-0.252	-0.90 ± 0.24	$b \rightarrow \mu$

The weighted mean of these results is $a_b = -0.94 \pm 0.20$. The errors given are statistical only.

The figures in the above tables are taken from Naroska (1983) with the exception of the results from the TPC group, are from Aihara (1985).

Chapter 9

$B^0\overline{B^0}$ Mixing and the b Asymmetry

$B^0\overline{B^0}$ mixing is the phenomenon in which the transitions $B^0 \rightarrow \overline{B^0}$ and $\overline{B^0} \rightarrow B^0$ occur via, to lowest order, diagrams like those illustrated in figure 9.1. If this mixing occurs it implies that it is possible for events to occur in which the initial b and $\bar{b}$ pair decay as two b quarks or as two $\bar{b}$ antiquarks, the probability of this happening depending on the rate of the mixing transitions, the lifetime of the b quark and the frequency with which B^0 and $\overline{B^0}$ mesons are produced in the fragmentation process.

The traditional means of looking for $B^0\overline{B^0}$ mixing is to exploit the information as to the quark charges available when semi-leptonic decays occur. The relative number of b events in which two oppositely charged leptons are produced in opposite jets and in which two like charged leptons are produced in opposite jets being partially dependent on the amount of mixing that has occurred. Ignoring the problems of identifying the prompt leptons in question the main background arises from events in which the quark has decayed through the cascade $b \rightarrow c \rightarrow l$ or the antiquark through the charge conjugate decay chain. The result of this is that the charge of the lepton is opposite to that of its parent and some like sign opposite jet di-lepton events are expected even in the absence of $B^0\overline{B^0}$ mixing. Results are normally presented in terms of the ratio r of the number of B^0 mesons that decay in their original guise to those that decay as the conjugate partner, that is

$$r = \frac{N(B^0 \rightarrow \overline{B^0} \rightarrow l^+) + N(\overline{B^0} \rightarrow B^0 \rightarrow l^-)}{N(B^0 \rightarrow l^-) + N(\overline{B^0} \rightarrow l^+)}.$$

Rapid mixing, in which the transition rate is such that many mixing transitions occur before the B^0 mesons decay, that is the product of the B^0 lifetime and the mixing transition rate is much greater than one, gives rise to $r = 1$ while if no mixing occurs $r = 0$.

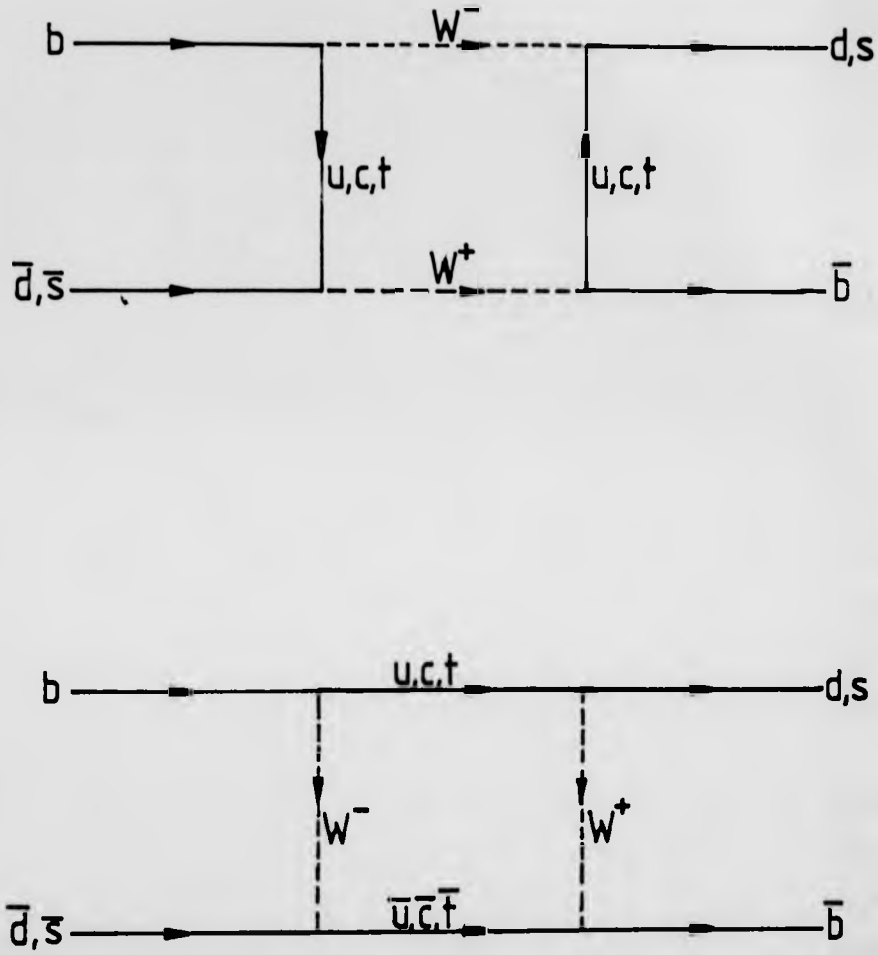

Figure 9.1. Feynman diagrams for $B^0\overline{B^0}$ mixing.

There are two types of B^0 meson, that formed from a b and an $\bar{s}$ and that formed from a b and a $\bar{d}$. The mixing rates for these two sorts of mesons, called B_s^0 and B_d^0 respectively, are not necessarily the same. Indeed the fact that $b \rightarrow c$ transitions are much favoured over $b \rightarrow u$ suggests that the rate of mixing is likely to be much larger for B_s^0 than for B_d^0 mesons. The ratios r for B_s^0 and B_d^0 mesons individually are labelled r_s and r_d respectively. The total mixing ratio is then

$$r = P_d r_d + P_s r_s$$

where P_r and P_s are the proportions of B_d^0 and B_s^0 mesons produced in the fragmentation.

From a study of like sign dilepton events the CLEO group concluded that at the 90% confidence level $r_d < 0.10$. They are unable to measure r_s as the energy of the electron-positron annihilations they study is below the threshold for the production of a $B_s^0\overline{B_s^0}$ pair. A similar study has been performed at PEP, where the higher energy enables production of both B_d^0 and B_s^0 mesons. This showed that r is less than about 0.2 (MARK II, 1985), again at the 90% confidence level.

The value of r may also be deduced from b asymmetry measurements in which the quark charge is tagged using a prompt lepton, provided it is assumed that the asymmetry with which the quarks were produced, A, is that given by the Standard Model. This is possible as the effect of incorrect tagging due to mixing is to reduce the measured asymmetry to A', in the same manner as described for 'wrong jet' electrons in the previous chapter.

The relationship between A, A' and r may be determined as follows. In order to make the analysis independent of the value of A and hence of energy it is performed in terms of

$$\Delta = \frac{A - A'}{A}.$$

The argument is given in terms of B^0 mesons, it applies also to $\overline{B^0}$ mesons when the charge conjugates of all the particles are taken.

Suppose that the number of B^0 mesons produced in the fragmentation is N_0. The number which, after undergoing mixing, decay to give positive leptons is

$$N^+ = \frac{r}{1+r} B_l^0 N_0$$

where B_l^0 is the branching ratio for the decay $B^0 \to l^-$. The number which decay to give negative leptons is

$$N^- = \frac{1}{1+r} B_l^0 N_0 .$$

If these N_0 neutral B mesons are a proportion R_0 of the N particles produced in a sample of b events which contain the initial b quarks, then in terms of N

$$N^+ = \frac{r R_0}{1+r} B_l^0 N$$

and

$$N^- = \left(\frac{R_0}{1+r} B_l^0 + (1 - R_0) B_l^- \right) N$$

where B_l^- is the branching ratio for the production of negative leptons from all particles, other than B^0 mesons, containing b quarks, in the proportions produced in the fragmentation process. Using the figures given in chapter two for the ratio of flavour production in the fragmentation process and for the ratio of baryon to meson production, R_0 is found to be 0.55. This value of R_0 will be assumed for the remainder of the discussion, it should be noted however that it has not been measured.

If N_F b quarks are produced in the forward direction and N_B in the backward, then the number tagged as being in the forward direction is the number of forward jets containing a negative lepton. That is

$$N_F' = \left(\frac{R_0}{1+r} B_l^0 + (1 - R_0) B_l^- \right) N_F + \frac{r R_0}{1+r} N_B .$$

The first term represents the number of forward jets arising from forward quarks, the former being smaller than the latter due to mixing, the second term is due to forward antiquarks in which mixing has produced what is tagged as a forward quark jet. Assuming that $B_l^0 = B_l^- = B_l$, in accordance with the spectator model, this becomes

$$N_F' = \frac{B_l}{1+r}\left[(1+r-rR_0)N_F + rR_0N_B\right].$$

Similarly

$$N_B' = \frac{B_l}{1+r}\left[(1+r-rR_0)N_B + rR_0N_F\right].$$

The measured asymmetry is then

$$\begin{aligned} A' &= \frac{N_F' - N_B'}{N_F' + N_B'} \\ &= \left(\frac{1+r-2rR_0}{1+r}\right)\frac{N_F - N_B}{N_F + N_B} \\ &= \frac{1+r-2rR_0}{1+r}A. \end{aligned}$$

Hence

$$\begin{aligned} \Delta &= \frac{A - A'}{A} \\ &= \frac{2rR_0}{1+r} \end{aligned}$$

for all energies. Thus

$$\begin{aligned} r &= \frac{\Delta}{2R_0 - \Delta} \\ &= \frac{A - A'}{A(2R_0 - 1) + A'} \end{aligned}$$

where the last result is obtained by substituting for Δ.

Alternatively the information concerning r available from b asymmetry measurements may be extracted from the values of the axial coupling constant of the b quark, a_b', obtained from those measurements. As

$$A = k\frac{a_e a_b}{q_b},$$

it is seen that

$$\Delta = \frac{a_b - a_b'}{a_b}.$$

Using $a_b = -1$ this becomes

$$\Delta = 1 + a_b'.$$

Thus

$$r = \frac{1 + a_b'}{2R_0 - 1 - a_b'}.$$

The measurement of the b asymmetry reported in this thesis is not precise enough to enable a limit to be placed on r. If it is combined with the result for the the b asymmetry previously obtained by the JADE group (Bartel, 1984a), the range of values which r may take can be somewhat restricted. The measurement, made using a sample of inclusive muon events, gave

$$A' = 0.228 \pm 0.060 \pm 0.025\,.$$

Combining this with the result obtained in this study, and adding the systematic and statistical errors in quadrature gives

$$A' = 0.230 \pm 0.060\,,$$

the result being dominated by the measurement made with the inclusive muon sample. This gives

$$r = -0.001^{+0.31}_{-0.19}$$

or, at the 90% confidence level,

$$r < 0.40$$

where it has been assumed that the expected Standard Model b asymmetry is exactly known.

Mixing in the $D^0\overline{D^0}$ system may, in principle, be investigated as above. There are however as yet no measurements of the c asymmetry of sufficient precision to enable limits to be set on this process.

SUMMARY

A brief description of aspects of the Standard Model was given, particularly those of relevance to the study of electron positron annihilations into quarks. The expected asymmetries of the production angle distribution of c and b quarks, with respect to the electron direction, including corrections due to the quark masses and QCD effects were found to be

$$A_c^{\mathrm{SM}} = -0.126 \pm 0.010$$

and

$$A_b^{\mathrm{SM}} = -0.230 \pm 0.020$$

where the errors arise as a result of the precision with which the parameters of the Standard Model are known.

A method of identifying electrons in multi-hadronic events recorded using the JADE detector was developed. The method gives, for a track entering the barrel part of the electromagnetic calorimeter, the probability that the track was that of an electron.

Techniques for the identification of the flavour of multi-hadronic events were investigated. It was found that, of the quantities studied, lepton momentum transverse to the event axis and the transverse mass of the event provide the clearest indication of an event's flavour. Furthermore, these two quantities are to a reasonable approximation independent. They may thus be used effectively in conjunction with one another.

The problems associated with the measurement of the asymmetry of the production angle of the quarks to the electron direction in electron positron annihilation were considered. The advantages of using a maximum likelihood fit to

the production angle distribution were demonstrated, these being the fullest use possible of the available information and the independence of the results obtained on detection inefficiencies symmetric in the quark production angle.

A measurement of the c and b quark asymmetries was made, the results of which were

$$A_c = -0.15 \pm 0.15 \pm 0.03$$

and

$$A_b = -0.24 \pm 0.16 \pm 0.03$$

respectively. From these results, assuming the charge of the c quark to be $2/3$, that of the b quark to be $-1/3$ and the axial coupling constant of the electron to the Z^0 to be -1.02 ± 0.12, as measured in neutrino scattering experiments, the axial coupling constants of the c and b quarks were calculated to be

$$a_c = 1.2 \pm 1.2 \pm 0.2$$

and

$$a_b = -0.98 \pm 0.67 \pm 0.17 .$$

These results are in agreement with the Standard Model expectations.

It was shown that the measurement of the quark asymmetries using lepton inclusive multi-hadronic events enables the study of mixing in the neutral meson systems, provided the Standard Model expectations for the asymmetries are accepted. An expression relating the decrease in measured asymmetry to the parameter r, conventionally used to describe mixing, was derived. A previous JADE measurement of the b asymmetry, made using an inclusive muon sample, combined with that above was used to determine the limit, at the 90% confidence level

$$r < 0.40$$

ACKNOWLEDGEMENTS

I should like to thank Professor Paul Murphy for the opportunity to study with the High Energy Physics group at Manchester University, and the Science and Engineering Research Council for ensuring that my overdraft is not as large as it might otherwise have been. My thanks to my supervisor, Dr. Ian Duerdoth, for his help and advice on all aspects of my study, and for proof-reading this thesis. I am grateful to Dr. Austin Ball for explaining the functioning of the JADE hardware to me and to Dr. Chris Bowdery for introducing me to the software and his efforts with the JADE standard analysis routines. My thanks also to all the members of the JADE group, in particular those at Manchester, for useful discussions concerning aspects of this thesis, to the directorate of the Deutsches Elektronen-Synchrotron for their hospitality, to the PETRA machine group and to the Computer Centre staff.

Writing this thesis would have been much more difficult without the support of Paul Hill and Jan Chrin, Susan Cartwright's expertise with the text processor and Christine who got me out of bed in the mornings, occasionally at unearthly hours. My thanks to all of them.

References

Abrams (1980) Phys. Rev. Lett. **44** 10.

Aihara (1985) "Heavy Quark Production in e^+e^- Annihilation at $29GeV$." Tokyo University.

Aitchison (1982) "An Informal Introduction to Gauge Field Theories." Cambridge University Press.

Aitchison and Hey (1982) "Gauge Theories in Particle Physics." Adam Hilger.

Allison et al. (1985a) Nucl. Inst. Meth. **A238** 220.

Allison et al. (1985b) Nucl. Inst. Meth. **A238** 230.

Allison and Cobb (1980) Ann. Rev. Nucl. Part. Sci. **30** 253.

Arnison et al. (1983a) Phys Lett. **122B** 103.

Arnison et al. (1983b) Phys Lett. **126B** 398.

Atarelli (1982) Nucl. Phys. **B208** 365.

Atwood (1983) SLAC-PUB-3266.

Bagnaia (1983) Phys Lett. **129B** 130.

Baines (1985) "Determination of the Lifetime and Semimuonic Branching Fraction of b Flavoured Hadrons Produced in e^+e^- Annihilation." Manchester University Ph.D. Thesis.

Banner et al. (1983) Phys Lett. **122B** 476.

Barlow (1985) JADE Note 124, to appear in the Journal of Computational Physics.

Bartel (1980) Zeit. für Phys. **C6** 295.

Bartel (1982) Phys. Lett. **108B** 140

Bartel (1983a) Phys. Lett. **108B** 140

Bartel (1983b) Phys. Lett. **129B** 145.

Abrams (1980)	Phys. Rev. Lett. **44** 10.
Aihara (1985)	"Heavy Quark Production in e^+e^- Annihilation at $29GeV$." Tokyo University.
Aitchison (1982)	"An Informal Introduction to Gauge Field Theories." Cambridge University Press.
Aitchison and Hey (1982)	"Gauge Theories in Particle Physics." Adam Hilger.
Allison et al. (1985a)	Nucl. Inst. Meth. **A238** 220.
Allison et al. (1985b)	Nucl. Inst. Meth. **A238** 230.
Allison and Cobb (1980)	Ann. Rev. Nucl. Part. Sci. **30** 253.
Arnison et al. (1983a)	Phys Lett. **122B** 103.
Arnison et al. (1983b)	Phys Lett. **126B** 398.
Atarelli (1982)	Nucl. Phys. **B208** 365.
Atwood (1983)	SLAC-PUB-3266.
Bagnaia (1983)	Phys Lett. **129B** 130.
Baines (1985)	"Determination of the Lifetime and Semimuonic Branching Fraction of b Flavoured Hadrons Produced in e^+e^- Annihilation." Manchester University Ph.D. Thesis.
Banner et al. (1983)	Phys Lett. **122B** 476.
Barlow (1985)	JADE Note 124, to appear in the Journal of Computational Physics.
Bartel (1980)	Zeit. für Phys. **C6** 295.
Bartel (1982)	Phys. Lett. **108B** 140
Bartel (1983a)	Phys. Lett. **108B** 140
Bartel (1983b)	Phys. Lett. **129B** 145.

Bartel (1983c)	Zeit. für Phys. **C20** 187.
Bartel (1983c)	Phys. Lett. **134B** 275.
Bartel (1983d)	Phys. Lett. **134B** 275.
Bartel (1984a)	Phys. Lett. **146B** 437.
Bartel (1984b)	Phys. Lett. **146B** 121.
Bartel (1985)	Zeit. für Phys. **C28** 343.
Bethke (1984)	JADE Note 111, unpublished.
Bjorken (1985)	Fermilab. Conf. 85/45.
Bjorken and Drell (1964)	"Relativistic Quantum Mechanics." M^{c}Graw-Hill Book Company.
Bjorken and Drell (1965)	"Relativistic Quantum Fields." M^{c}Graw-Hill Book Company.
Blewett (1977)	CERN 77-13.
Blobel (1977)	DESY F14/79-02.
Böhm and Hollik (1983)	DESY 83-118.
Brown et al. (1983)	CWRUTH-83-7.
Cartwright (1983)	"A Study of High Transverse Momentum Hadron Production in Two-Photon Interactions." Ph.D. Thesis, Glasgow University, DESY PLUTO internal report 84-01.
Cashmore et al. (1985)	Oxford preprint, 45/85.
CHARM (1985)	CERN-EP 85/113.
Chrin (1984)	"A Measurement of the Charge Asymmetry in $e^+e^- \rightarrow b\bar{b}$ and a Search for New Quarks at PETRA." Manchester University Ph.D. Thesis.
CLEO (1984)	CLNS-84/612.
Close (1979)	"An Introduction to Quarks and Partons." Academic Press.

Cords (1985)	DESY 85-074.
Edwards et al. (1982)	Phys. Rev. Lett. **49** 259.
Fairbank (1981)	Phys. Rev. Lett. **46** 967.
Fock (1927)	Phys. Rev. Lett. **46** 967.
Ford (1978)	SLAC report 210.
Fritzsch (1985)	MPI-PAE/PTh 42/85.
Gell-Mann and Levy (1960)	Nuovo Cimento **16** 705.
Gibson and Pollard (1976)	"Symmetry Principles in Elementary Particle Physics." Cambridge University Press.
Glashow (1961)	Nucl. Phys. **22** 579.
Goldstein (1951)	"Classical Mechanics." Addison-Wesley.
Guralnik et al. (1968)	"Advances in Particle Physics." Vol. 2, Interscience.
Heintze et al. (1982)	Nucl. Inst. Meth. **196** 293.
Hill (1985)	Manchester Univ. Ph.D. Thesis, in preparation.
t'Hooft (1971a)	Nucl. Phys. **B33** 173.
t'Hooft (1971b)	Nucl. Phys. **B35** 167.
JADE (1979)	JADE Note 44, unpublished.
JADE (1984a)	JADE Computer Note 71, unpublished.
JADE (1984b)	JADE Computer Note 79, unpublished.
JADE (1985a)	DESY 85-071.
JADE (1985b)	DESY 85-065.
Jersak et al. (1981)	Phys. Lett. **98B** 363.
Kim et al. (1981)	Rev. Mod. Phys. **53** 211.
Kobayashi and Maskawa (1973)	Prog. Theor. Phys. **49** 652.
Kogut (1983)	Rev. Mod. Phys. **55** 775.
Kreyszig (1962)	"Advanced Engineering Mathematics." Wiley.

Cords (1985)	DESY 85-074.
Edwards et al. (1982)	Phys. Rev. Lett. **49** 259.
Fairbank (1981)	Phys. Rev. Lett. **46** 967.
Fock (1927)	Phys. Rev. Lett. **46** 967.
Ford (1978)	SLAC report 210.
Fritzsch (1985)	MPI-PAE/PTh 42/85.
Gell-Mann and Levy (1960)	Nuovo Cimento **16** 705.
Gibson and Pollard (1976)	"Symmetry Principles in Elementary Particle Physics." Cambridge University Press.
Glashow (1961)	Nucl. Phys. **22** 579.
Goldstein (1951)	"Classical Mechanics." Addison-Wesley.
Guralnik et al. (1968)	"Advances in Particle Physics." Vol. 2, Interscience.
Heintze et al. (1982)	Nucl. Inst. Meth. **196** 293.
Hill (1985)	Manchester Univ. Ph.D. Thesis, in preparation.
t'Hooft (1971a)	Nucl. Phys. **B33** 173.
t'Hooft (1971b)	Nucl. Phys. **B35** 167.
JADE (1979)	JADE Note 44, unpublished.
JADE (1984a)	JADE Computer Note 71, unpublished.
JADE (1984b)	JADE Computer Note 79, unpublished.
JADE (1985a)	DESY 85-071.
JADE (1985b)	DESY 85-065.
Jersak et al. (1981)	Phys. Lett. **98B** 363.
Kim et al. (1981)	Rev. Mod. Phys. **53** 211.
Kobayashi and Maskawa (1973)	Prog. Theor. Phys. **49** 652.
Kogut (1983)	Rev. Mod. Phys. **55** 775.
Kreyszig (1962)	"Advanced Engineering Mathematics." Wiley.

Llewellyn-Smith (1974)	in "Phenomenology of Particles at High Energies." Scottish Universities Summer School, Academic Press.
Llewellyn-Smith (1982)	Phil. Trans. Roy. Soc. Lond. **304** 5.
Lüth (1979)	Proc. of Int. Symp. on Photon and Lepton Inter. at High Energy, Batavia Illinois.
MARK II (1985)	SLAC-PUB-3696.
Marshall (1984a)	RAL-84-002.
Marshall (1984b)	RAL-84-003.
Merzbacher (1961)	"Quantum Mechanics." Wiley.
Mills (1985)	To be published in Nucl. Inst. Meth.
Naroska (1983)	DESY 83-111.
Particle Data Group (1984)	Rev. Mod. Phys. **56** No. 2 Part II.
Pennington (1983)	Reports on Progress in Physics **46** 393.
Perkins (1982)	"Introduction to High Energy Physics." Addison-Wesley.
Peterson et al. (1983)	Phys. Rev. **D27** 105.
Salam (1968)	"Elementary Particle Theory." Almqvist, Forlag AB (Stockholm) p367.
Sauli (1977)	CERN 77-09.
Schubert (1984)	HEP-HD 84-09.
Schwinger (1958)	"Selected Papers on Quantum Electrodynamics." Dover Publications, New York.
Schwinger (1962)	Phys. Rev. **128** 2425.
UA1 (1985)	To appear in Proc. of the Bari Conf.
UA2 (1985)	To appear in Proc. of the Bari Conf.
Van Dyck et al. (1976)	Nature **262** 776.
Van Dyck et al. (1977)	Phys. Rev. Lett. **38** 310.
Weinberg (1967)	Phys. Rev. Lett. **19** 1264.

Weinberg (1972)	"Gravitation and Cosmology." Wiley, p41.
Weinberg (1980)	Rev. Mod. Phys. **52** 515.
Wetherill (1981)	"Intermediate Statistical Methods." Chapman and Hall.
Wetzel (1983)	University of Heidelberg preprint, May 1983.
Wick (1950)	Phys. Rev. **80** 268.
Wyatt (1983)	"A Study of the Production of b Quarks in e^+e^- Annihilation at High Energy." Oxford University Ph.D. Thesis.
Yang and Mills (1954)	Phys. Rev. **96** 191.
Ziman (1969)	"Elements of Advanced Quantum Theory." Wiley.